UNIVERSITY OF OKLAHOMA

GRADUATE COLLEGE

APPLICATIONS OF FLOQUET ANALYSIS TO MODERN PHASED ARRAY ANTENNAS

A DISSERTATION

SUBMITTED TO THE GRADUATE FACULTY

in partial fulfillment of the requirements for the

degree of

DOCTOR OF PHILOSOPHY

By

LAL MOHAN BHOWMIK
Norman, Oklahoma
2019

APPLICATIONS OF FLOQUET ANALYSIS TO MODERN PHASED ARRAY ANTENNAS

A DISSERTATION APPROVED FOR THE
SCHOOL OF ELECTRICAL AND COMPUTER ENGINEERING

By

Dr. Caleb J. Fulton, Chair

Dr. Christian Remling

Dr. Howard Bluestein

Dr. Nathan Goodman

Dr. Hjalti Sigmarsson

Dr. Jessica Ruyle

To my beloved parents **Prof. Nitai Charan Bhowmik** *and* **Chinu Rani Bhowmik**,

and to **Dr. Aruna Paul**– *my dear wife and friend,*

who stood by me all these years with unconditional love and support.

Acknowledgments

I would like to express sincere appreciation to my advisor, Professor Caleb Fulton. Without his dedicated supervision and sincere support, this research would not have been completed, and I would not have gained as much from my time at the University of Oklahoma, Norman, Oklahoma. He was the perfect role model for approaching research problems with his great vision and will always be an example. I am privileged to have experienced working in his group and learning from his insight and ability to stay future-oriented in a broad range of topics while keeping the depth of research and knowledge. I will always be candidly grateful for all his advice and support.

I would like to express appreciation for the work of my committee members, Professor Christian Remling, Professor Howard Bluestein, Professor Nathan Goodman, Professor Hjalti Sigmarsson, and Professor Jessica Ruyle, for taking the time to be part of my committee and for their valuable comments and suggestions.

I was fortunate to work in the Advanced Radar Research Center and with the fantastic people I got to meet during my doctoral journey. I am very thankful for all of the consultations and instructions, and also for the laughter and cheerful time we shared.

This dissertation would not exist without the support and love from my parents. My father, Professor Nitai Charan Bhowmik, and my mother, Chinu Rani Bhowmik, always motivated and encouraged me to study hard, even through the period of their difficult recovery from a serious road accident in 2007, and through multiple surgeries my father endured in 2017. My parents support for me never wavered even through a time of serious financial crisis. It has always been my goal to make them proud.

Finally, this thesis would not have been possible without the support and love from my wonderful wife, Dr. Aruna Paul. Ever since I met her, Aruna has brought me abundant happiness and love, and has illuminated my life even in desperate times. Pursuing a Ph.D involves taking a vow of hard work and agreeing to struggle for many lean years, but

Aruna was always there to encourage me. Her presence by my side gives me reason to live, to strive, and to succeed. Without her inspiration and motivation, I would never be where I am today. Aruna has been integral to the success of my quest. I credit my dear wife for my success, and thank her from the bottom of my heart for her sacrifice, love, and affection.

Contents

List Of Tables

List Of Figures

Abstract

Next generation radar technology is based on phased array technology and provides remarkable scanning flexibility and spatial search capability for the multifunction weather and air surveillance radar systems. The future weather radar is comprised of thousands of antenna elements and requires strict polarization purity, grating lobe free system, low sidelobe levels, suppressed surface waves, low cross-polarization, with beam shape requirements. To address these demands is a serious challenge. Over the past few decades, phased array radar technology has been a tremendous advancement in search for future radar technology. With the blessing of modern computational electromagnetic tools, the theory behind the electromagnetic and circuit-level behavior of large-scale phased array system opened the door to analyze the wide variety of multi-layered, complex system of large arrays. However, numerous challenges still remained unsolved for large scale development. One such challenge in integrating a large phased array is the threat of grating lobes that are introduced by unavoidable disturbances to the periodic structure at the seams between mechanical sub-array modules. In particular, gaps in the ground plane may interrupt the natural currents between elements, leading to radiation from periodic sources that are spaced at regular distances that are typically many wavelengths apart.

In order to quantify these grating lobe effects, an appropriate analysis framework and accurate model are of utmost importance. The model must capture all surface wave and mutual coupling between elements, and the analysis must have a clear formulation that allows for the calculation of worst-case grating lobe levels as well as differences in active reflection as a function of location within a sub-array. To accurately predict those effects, this dissertation work applied a modern method called Floquet framework, coupling with full wave solver to explore the grating lobe effects in infinite arrays of sub-arrays, with each physical sub-array potentially separated from the others by a gap or discontinuity in the ground plane. Calculations are then performed to extract active reflection coefficients and

grating lobe levels from the resulting Floquet mode scattering parameters. Additionally, this Floquet framework is expanded from broadside to any scan angles in space. In the mathematical framework, the surface equivalence theorem based on Huygens's equivalence principle is applied to authenticate its findings. From the simulation results, it is evident that the grating lobe amplitude level emerged to around 30 dB in the E-plane scan and E-plane grating lobes for a patch array. This is due to natural current disruption in between sub-arrays in the ground plane gap and it is very strong in the E-plane, leading to the potential for low-level grating lobe effects. The other planes and scan angles show less significant effects. It was found that the measurements qualitatively follow the simulated results. The Floquet-based method may therefore be used as a good approximation for a worst-case scenario where all gap-based perturbation effects are identical on each sub-array. This can be used for system-level planning to inform a mechanical solution to the electrical connection between sub-arrays.

Another fundamental and paramount challenge for phased array antenna is scan blindness. Scan range of the printed phased arrays is limited by the phenomenon known as scan blindness, which is induced by coherent coupling between the substrate waves/surface waves and the array's space harmonic fields. Near the scan blindness angle, a phased array system fails to function as a radiator or receiver because of strong excitation of substrate Transverse Electric (TE) and Transverse Magnetic (TM) waves and coupling of desired radiating energy to these unwanted substrate waves. Moreover, this dissertation work, with the aid of Floquet framework, accurately and more precisely captures the surface wave phenomena and its behavior using Electromagnetic Bandgap (EBG) structures to aim to reduce the surface wave excitation in an intelligent way. The reduction of surface waves can be beneficial in several ways to the next generation of digital phased arrays. First, the radiation efficiency will increase due to reduced surface wave excitation. Second, due to decreased surface waves the diffraction from the edges will also be decreased, leading

to decreased back radiation and interference with the main pattern in the forward region. Finally, reduction of surface wave excitation ultimately reduces coupling between adjacent antenna elements.

Furthermore, cylindrical radiating phased array radars have a unique challenge. Due to their conformal nature, they support cylindrical surface waves and cylindrical creeping waves. These modes have detrimental effects on the overall pattern quality and lead to "phase mode blindness" like as planar equivalent "scan blindness". This dissertation seeks to explain, address, and mitigate these surface and creeping wave effects and ultimately suppress "phase mode blindness" using cylindrical EBG structure.

1 Introduction

Phased array antennas are proliferating across a wide variety of applications. In modern days, they seem no longer to be an interest of just military (radar) applications, but are encountered in diverse civilian applications such as air traffic control and instrumental landing of airplanes, satellite communications, mobile communication base stations, radio astronomy, weather applications, medical applications (i.e., as microwave imaging to detect early breast cancer), and automotive applications (i.e., as automotive collisions avoidance radar or as adaptive cruise control technology). The beauty of phased array technology is its capability to perform accurate and rapid beam scanning within seconds, which allows a system to perform multiple tasks either enlaced in time or simultaneously. A phased array is a system of multiple antennas. By changing the phases of the antennas, the radiation pattern can be controlled in a particular direction and suppressed in undesired directions. Integration of electronics in the system increases the components and complexity and increases the frequency of operations for diverse applications. Today, very complex phased arrays can be manufactured over a wide range of frequencies and perform many functions. They can be electronically controlled which gives additional flexibility to perform all the tasks very accurately. The system can be programmed digitally to get more accurate and precise results very rapidly.

Despite their many potential capabilities, the high cost and complexity of phased arrays are the principal impediments to their deployment in various large scale applications. Therefore, it is paramount to understand their complexity, its limitations and capabilities, and also to explore the ways to make it cost effective. All of these pose significant challenges to understanding the basic electromagnetic and circuit level behavior of phased array systems. Even though some of the challenges are well-understood after years of research, there are still many fundamental challenges that need to be addressed. The purpose of this dissertation is to create a bridge to fill the gaps in understanding some of the problems at hand and propose ways to solve these problems.

1.1 Surface Waves

Surface waves are electromagnetic wave modes that bound to an interface between two materials and propagate along the surface. The materials could be any dissimilar materials, such as air, dielectric, metal, electromagnetic bandgap structures, or other kinds of materials. Surface waves can be of two types and are named transverse electric (TE) or transverse magnetic (TM) waves. In TE surface waves, the electric field is transverse to the direction of propagation and the magnetic field forms vertical loops out of the surface, while in TM surface waves, the magnetic fields are transverse to the direction of propagation and the electric field forms loops that extend vertically out of the surface. There are different ways these surface waves can be excited, such as with the antenna itself or other external radiation fields. As illustrated in Figure 1.1, a grounded dielectric slab, due to the presence of a dielectric substrate, always supports surface waves. The fields decay exponentially away from the boundary in both the positive and negative x and y directions. The rate of decay can vary and depends on the material's properties.

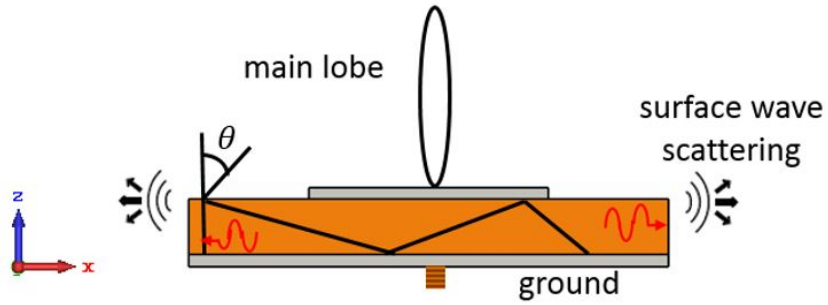

Figure 1.1: Propagation of surface waves modes on the grounded dielectric slab [1].

These surface wave excitations affect different microwave structures. For instance, they affect printed circuits, micro-strip lines, and antennas, and reduce the performance of the overall circuits. These surface waves can diffract at the finite-sized ground plane and lead to increased cross-polarization labels and ripples in the co-polarized radiation patterns. In the phased array, where multiple elements are required to build an array, these surface waves are strongly liable for strong mutual coupling. If the unit cell is larger than $0.5\lambda_0$, grating lobes and surface wave lobes can occur in the frequency band and scan volume of interest. As a result, scan blindness occurs at certain scan angles. Several procedures have been developed that mitigate this inherent problem. One of the methods to mitigate this issue is the use of high impedance surfaces. Using high impedance surfaces, one can alter the surface impedance and therefore the surface wave properties. High-impedance surfaces can be used to minimize the detrimental effects of the surface waves on antennas. By utilizing the textured metal surface, one can alter the scattering characteristics of the object. In this dissertation, high-impedance surfaces were used to control the surface wave propagation, and hence suppress scan blindness.

1.2 Ground Plane Gaps

Modern phased array and antenna applications require antennas to be mounted on the finite dielectric coated ground plane. Most of the analysis of the ground plane is based on the assumption that the ground plane is planar and infinite in extent. However, in practice all antennas are finite, so the ground plane is finite in nature. Typically, the electrical performance of the infinite ground plane antenna will be different from that of the finite ground plane. Therefore, the analysis must include the effects of the finite ground plane.

It is well established that a dielectric-coated ground plane supports a finite number of surface wave modes. In phased array, where multiple elements are necessary to build a radar, analysis is usually performed by unit cell analysis. While integrating these unit cells, they encounter gaps. These gaps perturb the natural current flow of the antenna elements. This smooth truncation of the dielectric-coated ground plane may alter the surface wave propagation and change the mutual coupling environment of each individual antenna element. Therefore, it is worthwhile to analyze a phased array that incorporates the ground plane gap effects, which will be analyzed in detail in Chapter. 3.

1.3 Dissertation Organization

This dissertation outlines details from multiple projects, with the common theme of application of Floquet analysis to modern phased array antennas.

Chapter 2 covers background information on the fundamentals of phased arrays and gap effects on phased arrays, particularly gaps in the ground plane of arrays of subarrays. Then a mathematical framework which accurately captures the mutual coupling and surface wave effects is suggested. This framework predicts and quantifies any worst case grating lobe effects for a large phased array system.

Chapter 3 presents the Floquet analysis overview and the standard mathematics behind it. This method can be coupled with the full wave solver.

Chapter 4 studies the gap effects on large phased arrays using the Floquet framework. In the past, the Floquet framework was coupled with the full wave solver to predict the performance of infinite arrays. However, this work is extended to analyze the infinite array with the finite sized sub-arrays, while capturing all mutual coupling and surface wave effects.

Chapter 5 investigates the benefits of EBG surface on modern phased arrays with the Floquet method for large phased array systems. Modern phased array antennas use $\lambda/2$ distance in between the array elements to avoid scan blindness. Over here the distance between the elements is more than $\lambda/2$ and the scan blindness is removed. However, using EBG structure the narrow bandwidth is found. Further research is necessary to investigate the bandwidth behavior of mushroom structures.

Chapter 6 explores the benefits of EBG surfaces on cylindrical geometries. Due to the conformal nature of the cylinder, cylindrical radar supports creeping waves. This chapter investigates how to suppress surface waves and creeping waves in the cylindrical geometry.

Chapter 7 summarizes and concludes the dissertation, and addresses directions for further research on Floquet modal framework. In addition, Electromagnetic bandgap material structure for modern phased array design is proposed.

2 Background on Phased Arrays

2.1 Introduction

In this chapter we will try to give an overview of electromagnetic behavior of phased array antennas starting from basic antenna fundamentals to antenna arrays and finally to phased array antennas. The basic fundamentals of the phased array antenna are also covered. These fundamentals are very essential in designing a successful phased array antenna system.

The phased array antenna is composed of groups of individual radiators and can be arranged in the space in various geometrical configurations to produce highly directive beams. These types of antenna arrangements are called arrays. In an array antenna, the antenna elements can be identical or different in size and shapes. The fields from each individual element constructively add to form a radiated beam of any desired shape in space and destructively add to cancel each other. The beam in the space is controlled by adjusting the phase and amplitude of the exciting signals at the individual elements. Therefore, without changing the position, beam scanning is possible electronically in the space. The overall performance of the phased array is affected by three principal parameters as given below:

1. The geometry of the array

2. The amplitude and phase excitation of each individual element

3. The radiation pattern of each individual element

No matter the purpose for which an antenna will be used, including in phased arrays, in cellular telecommunications, to broadcast, in medical applications, the performance of the radio frequency antenna is very crucial. Two major factors, the antenna resonance frequency, or center frequency, and the bandwidth, are very important design parameters in determining the performance of an antenna. The antenna needs to be well impedance-matched within its operating frequency.

2.1.1 Advantages of Phased Arrays

Using a phased array system, one can scan the complete hemispherical search in seconds accurately and rapidly, either interlaced in time or simultaneously. An electronically steered array radar is able to track a large number of targets and illuminate some of these targets with radio frequency (RF) energy. An electronically-controlled phased array gives more flexibility needed to perform all the various functions in a way best suited to the specific task at hand. The digital beam-steering technique even allows a faster and more accurate scan. Some of the unique capabilities of phased array antennas include:

1. Fast and accurate wide angle scanning without moving the antenna

2. Adaptive beam forming

3. Graceful degradation in performance over time

4. Distributed aperture

5. Multiple beams

6. Potential for low radar cross section

2.2 Grating Lobes

For a successful phased array design, it is necessary to understand the certain basic parameters of phased array antennas, for instance, the grating lobes, beam-width, instantaneous beam-width, etc. In phased arrays, there may be several pick intensities other than the desired beam. Those are called grating lobes. These are not the sidelobes. People usually confuse grating lobes with sidelobes. The grating lobe locations are a function of frequency and the element spacing. When the element spacing in the array is less than or equal to $\lambda_0/2$, there are no grating lobes, only main lobes exist. In general grating lobes appear when the array spacing is greater than $\lambda_0/2$. If the antenna elements spacing is greater than $\lambda_0/2$, the grating lobe appears even at broadside scanning.

In general, a linear array is comprised of identical elements positioned into a regular space in a regular geometrical configuration. Array factor for linear array for $N-$elements can be represented by

$$AF = \sum_{n=1}^{N} e^{j(n-1)(kd\cos\theta+\alpha)} \tag{2.1}$$

which can be written as

$$AF = \sum_{n=1}^{N} e^{j(n-1)\psi} \tag{2.2}$$

where

$$\psi = (kd\cos\theta + \alpha) \tag{2.3}$$

Therefore, array factor is a function of ψ is a Fourier series with a period of 2π.

$$AF(\psi + 2\pi) = \sum_{n=1}^{N} e^{j(n-1)(\psi+2\pi)} = \sum_{n=1}^{N} e^{j(n-1)\psi} e^{j(n-1)2\pi} = AF(\psi) \tag{2.4}$$

The array factor for a linear array is a function of θ. The complete structure can be determined from the values of θ as

$$0 < \theta < \pi \tag{2.5}$$

Usually this is refers to the visible region and map to $-1 < \cos\theta < 1$ or $-kd < kd\cos\theta < kd$, or

$$\alpha - kd < \psi < \alpha + kd \tag{2.6}$$

Actually equations 2.5 and 2.6 are functions of θ and ψ and determine the visible region. Let say we have exactly one period on the visible region and the period is 2π. Therefore, $2\pi = 2kd = 2(2\pi/\lambda)d$ or $d/\lambda = \frac{1}{2}$. Hence, when the element spacing is less than half wavelength, exactly one period of wavelength appears in the visible space. For more than one "half wavelength" spacing, there might be more major lobes appearing in the visible space. These additional lobes that have intensity equal to the main lobe are called grating lobes.

There are two grid structures of planar array. One is rectangular grid and the other one is triangular grid. Each has its own unique properties. For this study, we only considered the rectangular grid structure.

In most situations, it is undesirable to have grating lobes. As a result, most arrays are designed so the element spacings are less than one wavelength. The array grid of planar arrays controls the grating lobes. The scan performance of a rectangular-grid array behaves like the projected linear array in the scan plane.

2.2.1 Grating Lobes in Planar Array

In a linear array one can control the beam shape in only one plane, whereas when using a planar array one can control the beam pattern in both planes. In a planar array other

than principal planes one can use $sin\theta$ pattern space to see the periodicity of the grating lobes and to analyze the array in the 2-D plane. For a rectangular grid array, the grating lobe occurs when [3]

$$u_m = u_s + m\frac{\lambda}{a}, m = 0, \pm 1, \pm 2, ... \tag{2.7}$$

$$v_n = v_s + n\frac{\lambda}{b}, n = 0, \pm 1, \pm 2, ... \tag{2.8}$$

with the following relations :

$$\cos\theta_{n,m} = \sqrt{(1 - u_m^2 - v_n^2)} \tag{2.9}$$

where a and b are unit cell spacing and the a and b are the spacing between unit cell along $x-$ and $y-$ directions respectively. The first part of the right hand of the equations represents the locations of the main beam when antenna is scanned to θ_0. The second part represents the grating lobe locations. These are actually the periodic copies of the main beam.

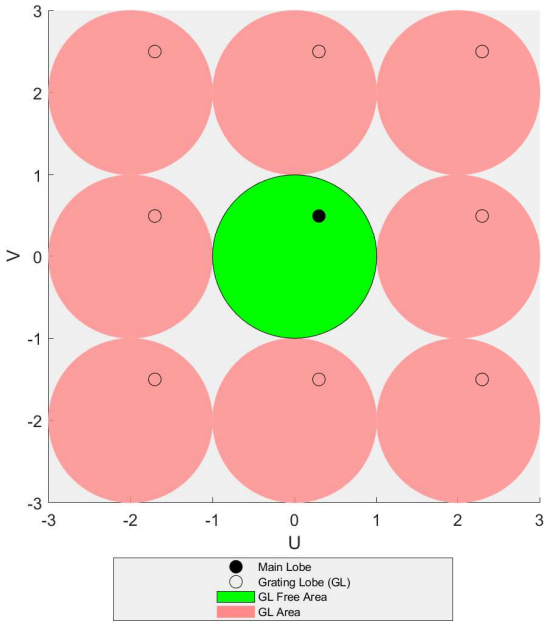

Figure 2.1: Grating lobe diagram in u-v space.

For planar rectangular grids, the grating lobe locations for half-wavelength spacing for both $x-$ and $y-$ directions have been depicted in Figure 2.1. The half wave-length spacing is chosen for the simplicity of the equations 2.7 and 2.8. As shown in Figure 2.1, the region inside the green circle is called the visible space. The black circle inside the green circle is the main beam for scanning angle $(\theta_s, \phi_s = 0°, 0°)$. The electronic scan beam can be scanned anywhere in the visible space without the presence of grating lobes.

2.3 Mutual Coupling

Mutual coupling is an important parameter in array theory. It can be defined as an electromagnetic interaction between the antenna elements in an antenna array. According to Stutzman and Thiele [4], mutual coupling has three components:

- Radiation coupling between two nearby antennas
- Interactions between an antenna and nearby objects, particularly conducting objects
- Coupling inside the feed network of an antenna array

Mutual coupling in real array alters the current magnitude (and thus impedance), and the phase distribution of each element from the free space values. Therefore, the total array pattern gets altered compared to no coupling case. It affects the antenna array primarily in following ways:

- Change the array radiation pattern
- Change the array manifold (the received element voltages)
- Change the matching characteristic of the antenna elements (change the element's input impedance)

Now, we will define the mutual coupling effects in terms of mutual impedance and scattering parameters and will only include the radiation coupling between the elements. Let us assume an arbitrary finite N element array. For the first element of an N element array, the way to relate terminal voltage and the element current is

$$V_1 = Z_{11}I_1 + Z_{12}I_2 + ... + Z_{1N}I_n \tag{2.10}$$

For N elements, it can be written as

$$\begin{aligned} V_1 = &\quad Z_{11}I_1 + \quad Z_{12}I_2 + \quad \ldots \quad + Z_{1n}I_n \\ V_2 = &\quad Z_{21}I_1 + \quad Z_{22}I_2 + \quad \ldots \quad + Z_{2n}I_n \\ &\ldots\ldots\ldots\ldots\ldots\ldots\ldots\ldots\ldots\ldots \\ &\ldots\ldots\ldots\ldots\ldots\ldots\ldots\ldots\ldots\ldots \\ V_n = &\quad Z_{1n}I_1 + \quad Z_{2n}I_2 + \quad \ldots \quad + Z_{nn}I_n \end{aligned} \tag{2.11}$$

where V_n= impressed voltage at the nth element, I_n = current flowing in the nth element, Z_{nn} = self-impedance of the nth element, Z_{mn}=Z_{nm} = mutual impedance between mth and nth elements. For nth terminal plane the total voltage and current is given by

$$V_n = V_n^+ + I_n^- \tag{2.12a}$$

$$V_n = V_n^+ - I_n^- \tag{2.12b}$$

where (V_n^+, I_n^+) and (V_n^-, I_n^-) are the incident and reflected waves at a specific point on the nth port. Equation 3.2 can be further simplified to

$$\begin{pmatrix} V_1 \\ V_2 \\ \vdots \\ V_n \end{pmatrix} = \begin{pmatrix} Z_{11} & Z_{12} & \ldots & Z_{1n} \\ Z_{21} & Z_{22} & \ldots & Z_{2n} \\ \vdots & \vdots & \ddots & \vdots \\ Z_{n1} & Z_{n2} & \ldots & Z_{nn} \end{pmatrix} \begin{pmatrix} I_1 \\ I_2 \\ \vdots \\ I_n \end{pmatrix} \tag{2.13}$$

or in matrix form as

$$[V] = [Z][I] \tag{2.14}$$

On the other hand, if V_n^+ is the amplitude of the voltage wave on port n, and V_n^- is the amplitude of the voltage wave reflected from port n, the $[S]$ matrix can be defined as

$$\begin{pmatrix} V_1^- \\ V_2^- \\ \vdots \\ V_n^- \end{pmatrix} = \begin{pmatrix} S_{11} & S_{12} & \dots & S_{1n} \\ S_{21} & S_{22} & \dots & S_{2n} \\ \vdots & \vdots & \ddots & \vdots \\ S_{n1} & S_{n2} & \dots & S_{nn} \end{pmatrix} \begin{pmatrix} V_1^+ \\ V_2^+ \\ \vdots \\ V_n^+ \end{pmatrix} \tag{2.15}$$

or

$$[V^-] = [S][V^+] \tag{2.16}$$

If we assume the characteristics impedance, Z_{0n}, of each port is identical, and set $Z_{0n} = 1$ from equation 3.3, the total voltage and currents at the nth port can be written as

$$V_n = V_n^+ + I_n^- \tag{2.17a}$$

$$V_n = V_n^+ - I_n^- = V_n^+ - I_n^- \tag{2.17b}$$

Using the definition of $[Z]$ from 3.3 and 3.8 we get

$$[Z][I] = [Z][V^+] - [Z][V^-] = [V] = [V^+] + [V^-] \tag{2.18}$$

which can be written as

$$([Z] + [U])[V^-] = ([Z] - [U])[V^+] \tag{2.19}$$

where $[U]$ is the identity matrix and can be defined as

$$[U] = \begin{pmatrix} 1 & 0 & \dots & 0 \\ 0 & 1 & \dots & 0 \\ \vdots & \vdots & \ddots & \vdots \\ 0 & 0 & \dots & 1 \end{pmatrix} \tag{2.20}$$

Comparing equations 3.10 and 3.6 we can say that

$$[S] = ([Z] + [U])^{-1}([Z] - [U]) \tag{2.21}$$

alternatively, we can find $[Z]$ matrix from $[S]$ matrix

$$[Z] = ([U] + [S])([U] - [S])^{-1} \tag{2.22}$$

In theory and practice, both can be used based on the requirements. In the finite sub-array we studied here, every individual antenna element within the sub-array will face a different mutual coupling environment. Hence, it is necessary to analyze the coupling behavior of each individual element. Using Floquet modal analysis we studied the coupling behavior of the antennas. The details of this Floquet modal framework is explained in Chapter. 3.

2.3.1 Eliminating Mutual Coupling

Mutual coupling is very important parameter in antenna arrays. If mutual coupling between the array elements can be known the array analysis can be performed rigorously in various aspects. According to Bhattacharyya [5], in general, the mutual coupling between the array elements can be quantified in terms of following measurable quantities:

- Mutual impedance

- Mutual admittance
- Scattering parameters

Mutual coupling alters the impedance and radiation characteristics of the elements. Unfortunately, it is very difficult to predict for a finite array. Mutual coupling usually tends to make the active element pattern more directive than the ideal element and, therefore, increase the scan roll-off of the array [6]. Hence, simply eliminating mutual coupling may deteriorate the active element pattern compared to what it should actually be.

2.3.2 Tightly Coupled Arrays

The traditional method of wide-band array design is to design an antenna element that has gain bandwidth $(10 : 1)$ or more. A recent innovation in wide-band phased arrays is the tightly coupled array. Tightly coupled arrays are of great interest due to their wide bandwidth, good scan performance, and low cross-polarization. The tight spacing of array elements in an array results in very high mutual coupling among the elements in the array. Over the years, researchers have found that tightly coupled elements were necessary to achieve wide bandwidth performance, while conventional array design seeks to reduce mutual coupling. The unexpected benefit is that the bandwidth of the embedded element pattern is larger than when isolated. The highly coupled array is a fundamentally different type of wide-band antenna where the mutual coupling among the array elements is utilized to shift down the center frequency and at the same time broaden the impedance bandwidth of the array [7]. Therefore, mutual coupling is very important to get the wide bandwidth.

2.4 Embedded Element Pattern

In order to understand the array behavior in phased array system, it is important to understand the radiated field intensity of an element in the far-field region. This parameter is often defined by element pattern. When this element pattern is a function of scan angle, it is called embedded element pattern. Embedded element pattern or scan element pattern (SEP), formally known as Active Element pattern, is gain per element versus scan angles. Scan element pattern, also a function of scan and frequency, tells the radar or communications systems designer how well the system works. Note that SEP is not an antenna "pattern;" it shows gain versus scan. The modifier "scan" implies a quantity that varies with scan angle. The scan element pattern will provide the phased array antenna gain at the position of the scanned beam as a function of scan angle.

2.4.1 Infinite Array Embedded Element Pattern

For a large phased array antenna, all scan element patterns will be nearly identical and the phased array antenna performance may be approximated by applying pattern multiplication. In this pattern multiplication, the common scan element pattern is multiplied with the array factor. Therefore, all coupling effects are accounted for then in the scan element pattern. The embedded element pattern can be defined as [5]

$$G_A(\theta, \phi) = G_e(\theta, \phi) \times AF(\theta, \phi) \tag{2.23}$$

where G_A represents the array gain pattern, G_e represents the active element gain pattern, and AF represents the normalized array factor with the sum of amplitude squares set of unity. The characterization of a large array antenna may be accomplished on the basis of the assumption that, in a large array, nearly all elements encounter a similar

array environment, and therefore also encounter identical mutual coupling effects from the surroundings.

2.4.2 Finite Sub-array Embedded Element Pattern

For an infinite array, active element pattern is the same for all elements. For a finite array, however, each element sees a different environment, so the active element pattern is different. To accurately and precisely calculate the active element pattern for a finite array, one must incorporate in the formulation all surface waves' and edge effects' contributions [8]. The equations should include all mutual coupling analysis between the antenna elements. Using Floquet modal analysis, the coupling coefficient is easily computed.

For an infinite array of a finite-sized sub array, edge effects do not contribute much to the overall array performance due to the fact that the center antenna element face equivalent to infinite array's center element environment. Hence, the active element pattern of infinite array of finite sized sub-array can be formulated as [9]

$$\vec{E}(\theta_{n,m}, \phi_{n,m}) = \hat{\theta}\left\{ jV_{n,m}^{TM}\sqrt{\frac{abZ_{n,m}^{TM}}{\lambda^2}} \right\} - \hat{\phi}\left\{ jV_{n,m}^{TE}\sqrt{\frac{abZ_{n,m}^{TE}}{\lambda^2}}\cos\theta_{n,m} \right\} \tag{2.24}$$

where

$$\cos\theta_{n,m} = \sqrt{1 - u_m^2 - v_n^2} \tag{2.25}$$

where a and b are the element spacings. $V_{n,m}^{TM}$ and $V_{n,m}^{TE}$ are the normalized modal voltages at the array aperture for the $TM_{n,m}$ and $TE_{n,m}$ Floquet modes, $Z_{n,m}^{TM}$ and $Z_{n,m}^{TE}$ represent the Floquet mode impedances relevant to $TM_{n,m}$ and $TE_{n,m}$ modes (e.g., 377 for a square lattice at broadside scan). It is worth mentioning that, the analysis utilized here under the assumption that array radiates in the infinite array environment when non-excited elements are match terminated. The details of this analysis are described in the Chapter. 3.

2.5 Scan Impedance

In a phased array, scanning by changing the feeding coefficients changes element input impedance, called the scan impedance. For an infinite array the formulation is very easy. However, the scan impedance, which is related to the scan reflection coefficient, is also defined by a radiating element as a function of scan angle, when all of the radiating elements are of the proper magnitude and phase. The scan impedance of a non-ideal radiating element is a function of the phase from across the array aperture. From the scan reflection coefficient, it can be immediately obtained through a well-known relationship as [10]

$$Z(\theta, \phi) = Z_0 \frac{1 + \Gamma(\theta, \phi)}{1 - \Gamma(\theta, \phi)} \tag{2.26}$$

where Z_0 is the port impedance and $\Gamma(\theta, \phi)$ is the scan reflection coefficient. A phased array consists of discrete radiators. The array is usually linear or planar, but can be cylindrical, spherical, or any conformal shape. Any array design must consider mutual coupling, scan blindness effects, grating lobes, polarization purity, bandwidth, etc. Impedance match is a function of scan due to mutual coupling.

2.5.1 Scan Blindness

In a phased array, when antenna elements are excited, substrate modes also get excited. These substrate waves change the mutual coupling of the array elements. When these substrate modes couple to the radiating mode at certain scan angles, the antenna does not radiate. Scan blindness is a specific phenomenon of a large phased array where some of antennas cease to radiate. Scan blindness is always undesirable. It happens when the propagation constant of a surface wave mode coincides with that of the Floquet mode, at

which point these two modes couple strongly, leading to a resonance and subsequent scan blindness.

If an infinite array structure is capable of supporting a guided wave, then under certain Floquet excitations, the guided mode may be strongly excited. Depending on the coupling mechanism between the radiating elements and the guided mode, the input voltage across each source element becomes either infinitely large, zero, or the voltage and the current are in phase quadrature. The above three voltage-current relations lead to infinite, zero, or reactive input impedance; hence the array ceases to radiate. This effect is known as scan blindness of the array.

Scan blindness becomes worse as the array size increases and is not a severe problem for small arrays. Complete scan blindness, occurring when 100% of the power is reflected from the elements, only occurs in infinite arrays.

Scanning to the blind angle means that k_z becomes imaginary while a surface wave mode propagates along the surface of the array. Blindness occurs when the imaginary part of the impedance becomes extremely large even when the real part may be nonzero. In order for blindness to occur, k must be zero, and the wave propagation constant must equal the surface wave propagation constant.

$$k_{sw} = \sqrt{k_{xs}^2 + k_{ys}^2} \tag{2.27}$$

Surface wave exist in a dielectric substrate of thickness h when for the TE mode

$$k_{zd} \cos k_{zd} h + j k_{z0} \sin k_{zd} h = 0 \tag{2.28}$$

and for the TM mode

$$\epsilon_r k_{zd} \cos k_{zd} h + j k_{z0} \sin k_{zd} h = 0 \tag{2.29}$$

where 0 in the subscript indicates free space and d indicates dielectric. For substrate with $h < \frac{\lambda_0/4}{\sqrt{\epsilon_r - 1}}$ only the lowest order TM surface wave modes exist.

According to Mailoux [11], array blindness results when the array geometry with short-circuited input ports would support a normal mode (lossless non-radiating propagation) along the structure at some given scan angle. With the array excited at all input ports, at the angle of array blindness, the input impedance at all ports are identically zero, with the structure supporting a non-radiating lossless mode. In finite array, the energy gets radiate in terms of grating lobes, in mechanical, or other thermal energies.

2.6 Gaps in the Ground Plane

To predict the performance of a large phased array antenna, precise and accurate modeling and validation of those modeling efforts are of utmost importance. A well-designed phased array should not have any grating lobes, as they can be avoided by proper choice of element lattice relative to the highest operating frequency and largest scan angle. However, one practical concern in integrating large phased array antennas is a low-level grating lobe effect that may appear because of interruption of the overall periodic structure due to the physical connection between mechanical sub-arrays of finite size. Recent advances in computational electromagnetics have enabled the analysis of larger and larger finite phased arrays, but simulations of arrays with thousands of elements are often problematic. This is especially the case if details like mechanical interconnections (and potential ground plane gaps) are also included.

To meet the demand for weather tracking and air surveillance, modern phased array design requires thousands of antenna elements. One practical way to arrange these antenna elements that are in the group of sub-arrays can be called line replaceable units (L-R-U). These LRUs can be assembled in a rectangular grid by putting each LRU along horizontal

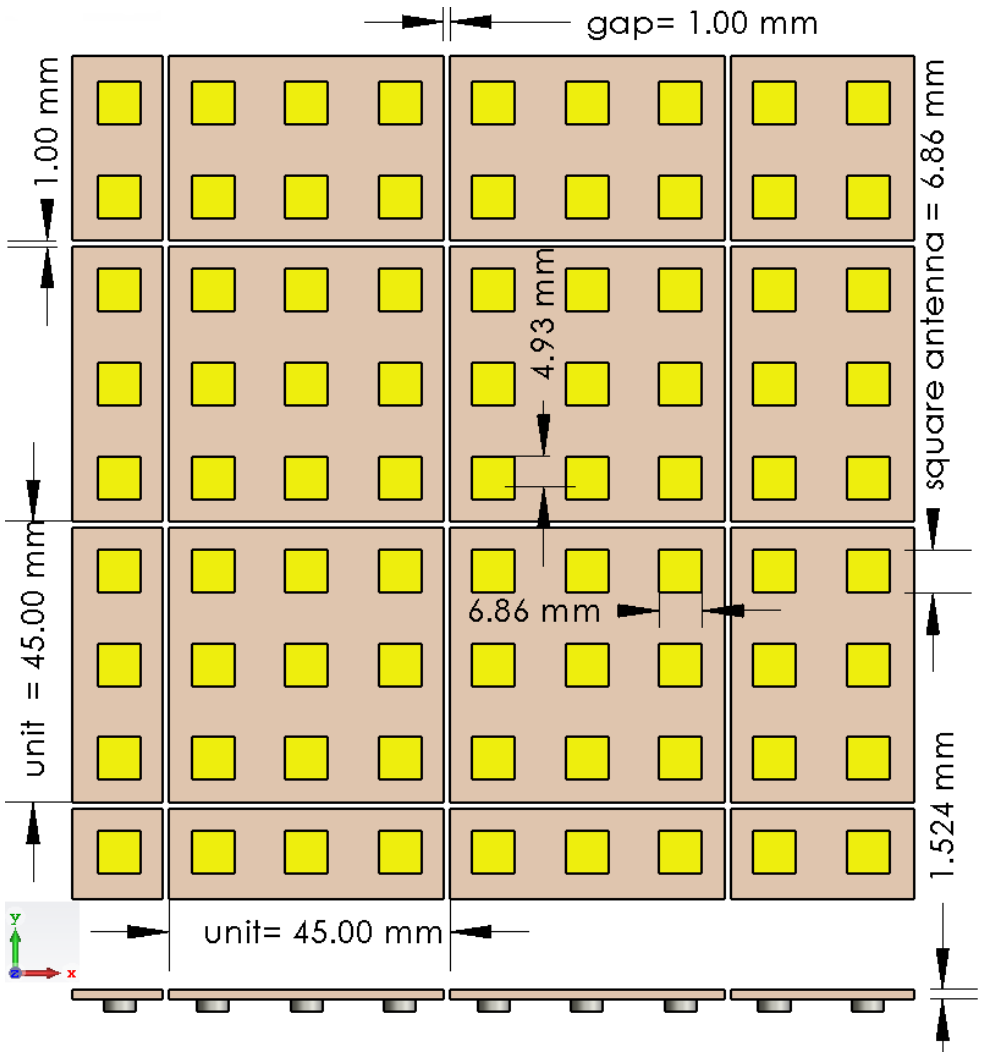

Figure 2.2: Ground plane gap model.

and vertical axes to form a planar configuration as shown in Figure 2.2. The main reason for such arrangements is probably the fact that service engineers can easily replace the LRU upon failure, which eventually helps to save service costs in the long run. An X-band 3×3 unit cell was designed. Each unit cell size is 45 mm $\times$ 45 mm. To mimic the practical situation of real phased array system a 1 mm gap is created in between each sub-array as can be seen in Figure 2.2. These gaps are the main culprits which impede the natural current flow between array elements. The simulation of such a large 8×8 and complicated

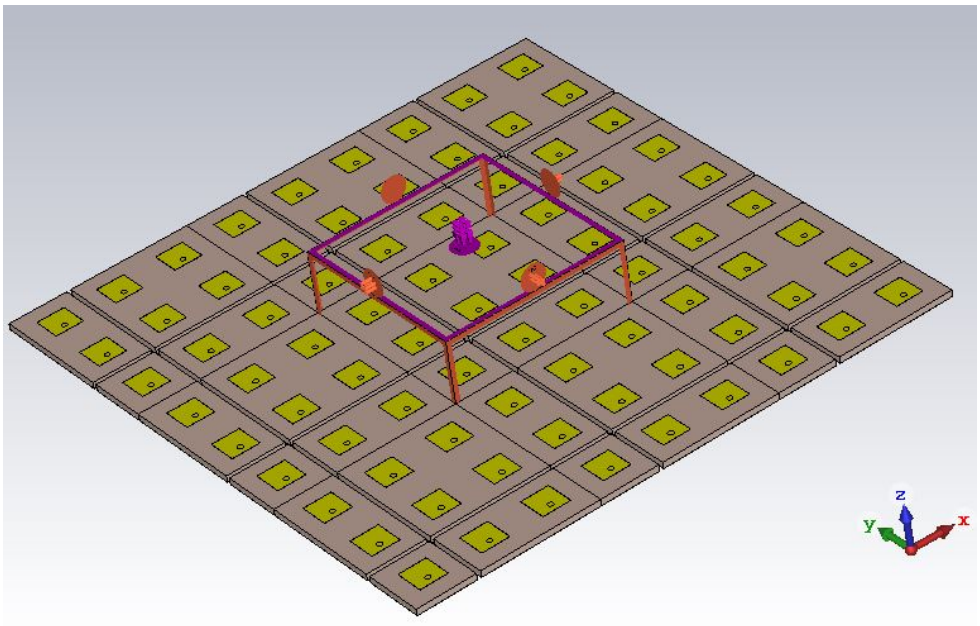

Figure 2.3: Unit cell set up for the gap model.

sub-array unit cell is difficult, but could predict serious grating lobe-related limitations long before building the eventual 10,000 element/face array.

However, if the overall array can still be reasonably treated as a periodic structure of finite sub-arrays that in turn forms a large phased array, then periodic boundary conditions, based on Floquet' s theorem, may be used on a single sub-array (one " unit cell " instead of the entire array geometry). An example of such unit cell set up is presented in Figure 2.3. This approach was explored through pure simulation in [9], where grating lobe limitations due to periodic ground plane gaps were estimated. The simulations must make use of many Floquet modes, owing to the larger (relative to a wavelength) unit cell size. This leads to both software (mode count) and memory/time limitations for larger sub-arrays. Analysis of more advanced antennas, with complex geometries, multi-layered structures, vias in electromagnetically sensitive locations, and 3-D structures will only exacerbate

these memory and time issues. Moreover, some systems like the future nationwide Multi-function Phased Array Radar (MPAR) program require very low peak sidelobe levels, as strict as -50 dB [12].

What is needed is an efficient and accurate method to analyze these effects validated through basic measurements. The next chapter will investigate such an analysis using Floquet modal framework.

3

Floquet Modal Analysis of Phased Array Antennas

The phased array antenna is becoming increasingly popular because of it provides the capability of command-able, agile, high gain beams which is very useful for radar, weather applications, airborne and space-borne applications. Phased array antenna system can be reconfigured electronically in a way that allows, for instance, beam scanning, multiple spot beams and shaped beams. Generally, the analysis of an array antenna involves a two-step process, such as characterizing an isolated element, and employing the element's characteristics to predict the performance of the full array. The underlying assumption in this approach is that the element characteristics remain invariant with respect to the array scan. Such an analysis works reasonably well if the coupling between the elements is negligibly small. For strongly coupled elements the analysis becomes inaccurate. This happens in the case of a wide-angle scan array, where the element spacing is kept small to avoid grating lobes. Therefore, to predict the performance of a wide angle scan array accurately, the analysis must include the mutual coupling effects.

For the array-pattern analysis, the well-known equation (i.e., array-pattern = array factor $\times$ isolated element pattern) does not explicitly include the mutual coupling effects. Inclusion of mutual coupling effects involves coupling analysis between the elements and subsequent manipulation of a coupling matrix. Alternatively, if one could determine the

element pattern in the array environment, then the above simple equation for array pattern becomes valid. Such an element pattern in the array environment is known as the active element pattern (AEP) or the embedded element pattern. The Floquet modal analysis yields the AEP, which implicitly includes the mutual coupling effects. In addition, the Floquet modal analysis yields the coupling coefficients between the elements in the "array environment". The conventional element-by-element approach ignores the effects of the neighboring elements when coupling between two elements in an array is considered. The effect of the neighboring elements on mutual coupling may be substantial for many situations.

To include the mutual coupling effect for broadside radiation, the concept of infinite array analysis of radiating sources was first introduced by Wheeler in 1948 [13]. A radiating element inside a waveguide was analyzed in a way that essentially emulates an infinite array of the elements from the image theory perspective. For analyzing a scanned beam array including mutual coupling effects, Stark employed the Fourier series expansion method [14]. He included the linear phase variation terms in the Fourier series, thus implicitly introducing "Floquet modal expansion". The radiation impedance, in the form of a doubly-infinite series, was deduced. Following Stark's formulation, Wheeler introduced a "pictorial presentation" of the impedance, which he called "grating-lobe series" method [15]. Farrell and Kuhn also employed the Floquet model to obtain the reflection coefficient and power pattern of an infinite array of rectangular waveguides [16]. A similar approach was used by other researchers to study surface wave resonance effects in dielectric loaded waveguide arrays [17].

In this chapter, we present a Floquet modal analysis of an infinite array with a finite sub-array. The finite sub-array analysis includes three major steps. In the first step, an infinite array with uniform excitation is analyzed using Floquet modal expansion. Under such excitation, the active reflection and transmission coefficients of an element are

determined. In the second step, the driving point reflection coefficients of a fully excited finite array are obtained using the scattering matrix formulation. It is shown that the elements of the scattering matrix (i.e., the coupling coefficients) can be determined from the active reflection coefficients of an element in an infinite array. In the third step, the vector AEP is obtained. Hence, the radiation pattern of a finite array with an arbitrary excitation can be computed. In our study we specifically focused on grating lobe effects on phased array antennas. Grating lobe amplitude increases due to disruption of the ground plane. The explanation of such a behavior is explained.

3.1 Overview of Floquet Modal Analysis

The field excited by a periodic phased array can be decomposed into an infinite number of modes, which are referred to as Floquet modes. Depending on the frequency, some modes propagate and some modes decay along the z-direction. The former are usually referred to as propagating waves, and the latter are often called evanescent waves. Both modes are indexed by m and n, along the two respective dimensions, according to the framework shown in Figure 3.1. In this framework, "UC" represents a periodic unit cell boundary condition that enforces the two-dimensional periodicity along these dimensions. There are also open boundaries, parallel to the unit cell lattice, above and below it, which are realized in finite element solvers with Floquet ports that are similar to waveguide ports. The Floquet modal development naturally employs an S-matrix formulation for all of the modes, and all of the developments in this paper will utilize this convenient formulation.

The number of propagating modes depends on the frequency, scan angle, and unit cell size, but for a given array there ideally exists only one propagating mode pair (TE and TM) corresponding to $m = n = 0$. This so-called "fundamental" mode represents a plane wave propagating in the scan direction (θ_s, ϕ_s) when the array is transmitting.

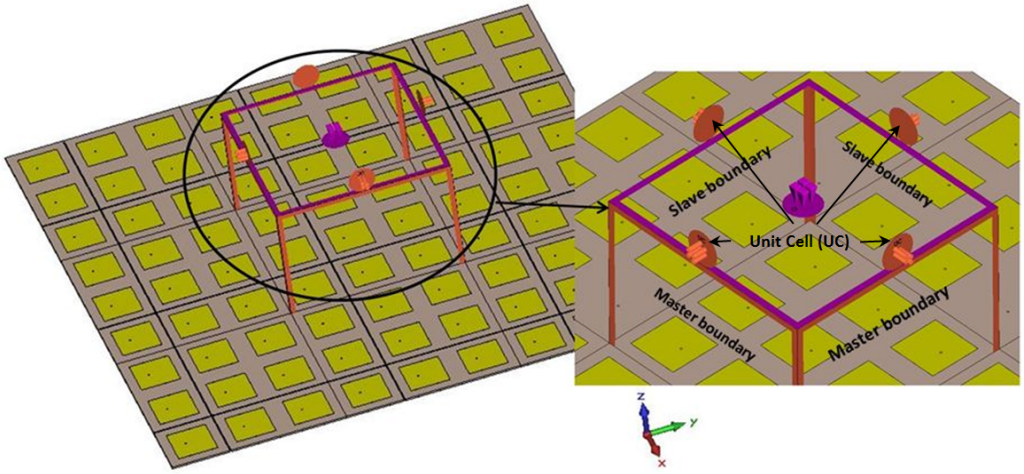

Figure 3.1: Typical Fouquet modal unit cell boundary condition.

Fortunately, numerical experiments have shown for single-element lattices that only the propagating Floquet modes and a few evanescent Floquet modes are needed to yield very accurate solutions [18].

When scanning to an angle (θ_s, ϕ_s), the phase difference between adjacent sub-arrays situated along the x and y directions are $\psi_x = k_0 a \sin\theta_s \cos\phi_s$ and $\psi_y = k_0 b \sin\theta_s \sin\phi_s$, respectively, where k_0 is the wave number in free space. The normalized modal electric field vectors (transverse components and variation only), corresponding to the resulting Floquet modes, are given by [18]

$$\bar{e}^{TE}_{n,m}(x, y, \psi_x, \psi_y) = \frac{\hat{x}k_{yn} - \hat{y}k_{xm}}{\sqrt{ab(k_{xm}^2 + k_{yn}^2)}} \exp(-jk_{xm} - jk_{yn}) \tag{3.1}$$

$$\bar{e}^{TM}_{n,m}(x, y, \psi_x, \psi_y) = \frac{\hat{x}k_{yn} + \hat{y}k_{xm}}{\sqrt{ab(k_{xm}^2 + k_{yn}^2)}} \exp(-jk_{xm} - jk_{yn}) \tag{3.2}$$

where $a \times b$, is the unit cell size, hats symbolize unit vectors and k_{xm} and k_{yn} are the Floquet wave numbers along x and y directions, respectively for the ith Floquet mode. For a rectangular grid, the wave numbers are given by:

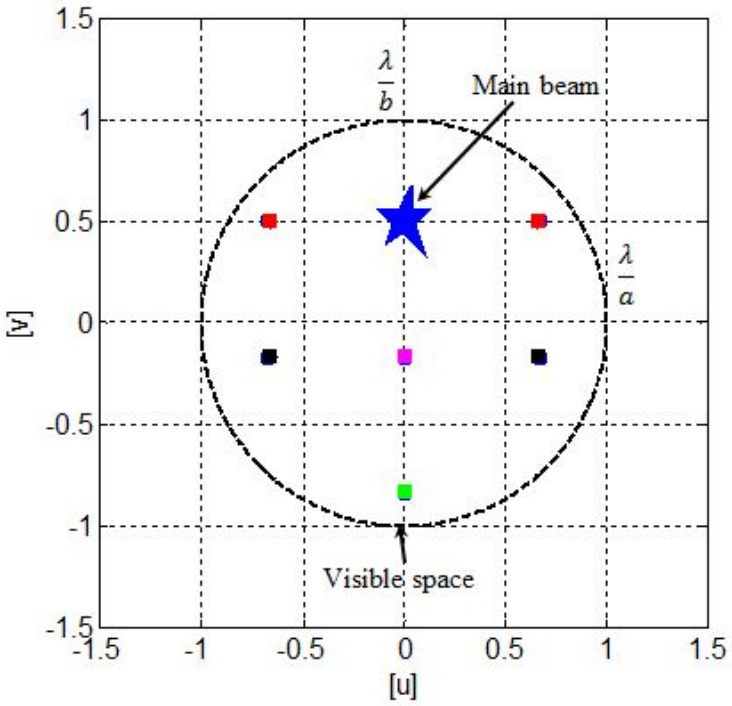

Figure 3.2: Grating lobe diagram for $1.5\lambda \times 1.5\lambda$ array with scanning angle ($\theta_s = 30°, \phi_s = 90°$).

$$k_{xm} = \frac{\psi_x + 2m\pi}{a} \tag{3.3}$$

$$k_{yn} = \frac{\psi_y + 2n\pi}{b} \tag{3.4}$$

where integers m and n, as well as whether a specific mode is TE or TM, depend on the Floquet mode index i. For the purposes of this research work, define the Floquet indices $i_{n,m}^{TE}$ and $i_{n,m}^{TM}$ to be those corresponding to the TE and TM mode, respectively, for a given n and m. Normalization of equations 3.3 and 3.4 by k_0 produces the following coordinates [19];

$$u_m = u_s + m\frac{\lambda}{a}, m = 0, \pm 1, \pm 2, ... \tag{3.5}$$

$$v_n = v_s + n\frac{\lambda}{b}, n = 0, \pm 1, \pm 2, ... \tag{3.6}$$

The coordinates generate the locations of all grating lobes on the (u, v) or direction cosine plane, which is traditionally used to visualize the migration of grating lobes under scanning [20]. All real angles, representing visible space, are inside on the unit circle in this plane. Angles outside the unit circle are "imaginary" or invisible space. When the main beam is scanned, the origin of the (u, v) plot moves to the new value and all grating lobes moves correspondingly. However, the unit circle remains fixed. Any coordinate (u, v) falling within the unit circle other than the fundamental beam $m = n = 0$ represents a grating lobe location, shown in Figure 3.2. Since the sub-array lattice constants a and b are typically multiple wavelengths, several such grating lobes may exist, spaced by λ/a and λ/b in the u and v directions, respectively.

The scattering matrix that relates antenna terminal and Floquet modes is given by [5]

$$\left[V^-\right] = \left[S\right]\left[V^+\right] \tag{3.7}$$

where $\left[V^-\right]$ is the normalized incident voltage vector and $\left[V^-\right]$ is the normalized reflected voltage vector at the input port and $\left[S\right]$ is the scattering matrix of order $(N_s + N_f) \times (N_s + N_f)$, where N_s is the number of elements per sub-array and N_f is the number of Floquet modes being considered. This matrix can be decomposed into four sub-matrices as:

$$\left[\ S\right] = \left[\begin{array}{c:c} S^a & S^r \\ \hdashline S^r & S^F \end{array}\right] \tag{3.8}$$

where S^a, S^r, and S^F represents scattering parameters for ports, radiation and Floquet, respectively.

3.1.1 Radiation Patterns and Grating Lobe Calculations

A *single-element*, single-polarization "sub-array " unit cell will produce an electromagnetic field that can be represented in terms of Floquet modal fields as [18]

$$\vec{E}(x,y) = \sum_{i=1}^{\infty} S_{i1}^{r}(\psi_x,\psi_y)\vec{e_i}(x,y,\psi_x,\psi_y) \tag{3.9}$$

In the above equation, S_{i1}^{r} is the transmission coefficient from the antenna port (port 1) to the ith Floquet mode and $\vec{e_i}$ is the normalized modal electric vector for the ith Floquet mode, corresponding to a particular n, m, and TE or TM mode from equations 3.3 and 3.4. These transmission coefficients are directly computed from a unit cell analysis with periodic boundary conditions.

For the arrays in question here, those built on two-dimensional rectangular sub-arrays with elements indexed by j within a sub-array, the fields are given by

$$\vec{E}(x,y) = \sum_{i=-\infty}^{\infty}\sum_{j=1}^{N} S_{i,j}^{r}(\psi_x,\psi_y)\vec{e_{i,j}}(x,y,\psi_x,\psi_y)e^{-jk_0(u_s x_j + v_s y_j)} \tag{3.10}$$

Here, the element locations are (x_j, y_j) and $S_{i,j}^{r}$ is as defined above. The modal voltages associated with the $i_{n,m}^{TE}$ and $i_{n,m}^{TM}$ modes are

$$V_{n,m}^{TE} = \sum_{j=1}^{N} S_{i_{n,m}^{TE},J}^{r}(\psi_x,\psi_y)e^{-jk_0(u_s x_j + v_s y_j)} \tag{3.11}$$

$$V_{n,m}^{TM} = \sum_{j=1}^{N} S_{i_{n,m}^{TM},J}^{r}(\psi_x,\psi_y)e^{-jk_0(u_s x_j + v_s y_j)} \tag{3.12}$$

The vector form of the resulting radiated fields at the scan angle (θ_s, ϕ_s) becomes [5]

$$\vec{E}(\theta_s,\phi_s) = \hat{\theta}\left\{jV_{0,0}^{TM}\sqrt{\frac{abZ_{0,0}^{TM}}{\lambda^2}}\right\} - \hat{\phi}\left\{jV_{00}^{TE}\sqrt{\frac{abZ_{0,0}^{TE}}{\lambda^2}}\cos\theta_s\right\} \tag{3.13}$$

where $V_{0,0}^{TM}$ and $V_{0,0}^{TE}$ are the normalized modal voltages at the array aperture for the $TM_{0,0}$ and $TE_{0,0}$ Floquet mode, $Z_{0,0}^{TM}$ and $Z_{0,0}^{TE}$ represent the fundamental mode TE and

TM Floquet mode impedances (e.g., 377 for a square lattice at broadside scan). The gain can be determined by appropriately normalizing these fields. Similarly, under the assumptions herein, reciprocity dictates that the overall transmit and receive patterns are identical.

The radiated fields may be modified for any scan angles and for any Floquet scan impedances with the following relations

$$\vec{E}(\theta_{n,m},\phi_{n,m}) = \hat{\theta}\left\{jV_{n,m}^{TM}\sqrt{\frac{abZ_{n,m}^{TM}}{\lambda^2}}\right\} - \hat{\phi}\left\{jV_{n,m}^{TE}\sqrt{\frac{abZ_{n,m}^{TE}}{\lambda^2}}\cos\theta_{n,m}\right\} \tag{3.14}$$

where

$$\cos\theta_{n,m} = \sqrt{1-u_m^2-v_n^2} \tag{3.15}$$

The Ludwig-2 AZ/EL definition of polarization is used here because it is the most relevant for the polarimetric weather radar application from which this work draws its accuracy-driven inspiration. According to this definition [21]

$$E_A(A,E) = \frac{\cos\phi_s}{\cos E}E_{\theta_s}(\theta_s,\phi_s) - \frac{\cos\theta_s\sin\phi_s}{cosE}E_{\theta_s}(\theta_s,\phi_s) \tag{3.16}$$

$$E_E(A,E) = \frac{\cos\theta_s\sin\phi_s}{\cos E}E_{\theta_s}(\theta_s,\phi_s) + \frac{\cos\phi_s}{cosE}E_{\theta_s}(\theta_s,\phi_s) \tag{3.17}$$

where

$$\cos E = \sqrt{1-(\sin\theta_s\sin\phi_s)^2} \tag{3.18}$$

The results below reflect this definition of polarization, where elevation (E) maps to co-pol and azimuth (A) maps to cross-pol for the arrays investigated.

It is worth mentioning that, the grating lobe locations and radiated fields for grating lobe $\vec{E}(\theta_{n,m},\phi_{n,m})$ for a given scan direction can be computed from Floquet wave numbers. The grating lobe directions $(\theta_{n,m},\phi_{n,m})$ with the Floquet wave numbers are given by [5]

$$\sin\theta_{n,m}\cos\phi_{n,m} = \frac{m\lambda_0}{a} + \sin\theta_s\cos\phi_s \tag{3.19}$$

$$\sin\theta_{n,m}\sin\phi_{n,m} = \frac{n\lambda_0}{a} + \sin\theta_s\sin\phi_s \tag{3.20}$$

The solution of equations 3.19 and 3.20 give a finite set of real solutions of $(\theta_{n,m}, \phi_{n,m})$ and these represent corresponding grating lobe locations. The grating lobe direction for a finite number of elements excitation in the sub-array, creates $(N_s + N_f) \times (N_s + N_f)$ eigenvectors. Each eigenvector comprises a set of grating lobes [5]. Therefore, intensities of the grating lobes such as the amplitude and phase of the grating lobes are related to the eigenvectors.

3.1.2 Mutual Coupling and Active Impedance

The mutual coupling information between the elements is important in determining the active impedance of an element with respect to given amplitude and phase distributions [5]. For a given excitation of a finite array with a port scattering matrix S^b, the active reflection coefficient of the ith element is given by

$$\Gamma_i = \sum_{j=1}^{N} S^b_{i,j}\frac{V_j^+}{V_i^+} \tag{3.21}$$

For infinite arrays where matched loads are assumed on all elements, the excitation is uniform and the active impedance is only a function of scan angle. However, for arrays of sub-arrays, the active impedance will additionally depend on where a given element is positioned within a sub-array, and this can be calculated as

$$\Gamma_i = \sum_{j=1}^{N} S^a_{i,j} e^{-jK_0(u_s)|x_j - x_i| + v_s|y_j - y_i|} \tag{3.22}$$

3.2 Simple Example Simulations

Antenna arrays can be based on a variety of designs, (e.g., dipole, log-periodic dipole, microstrip, etc.) each having their own modeling technique and performance characteristics [22]. For the illustrative purposes of this dissertation, square microstrip patch antennas, shown in Figure 3.3, are adopted due to the relative simplicity of the design, and the fact that they represent a common phased array element.

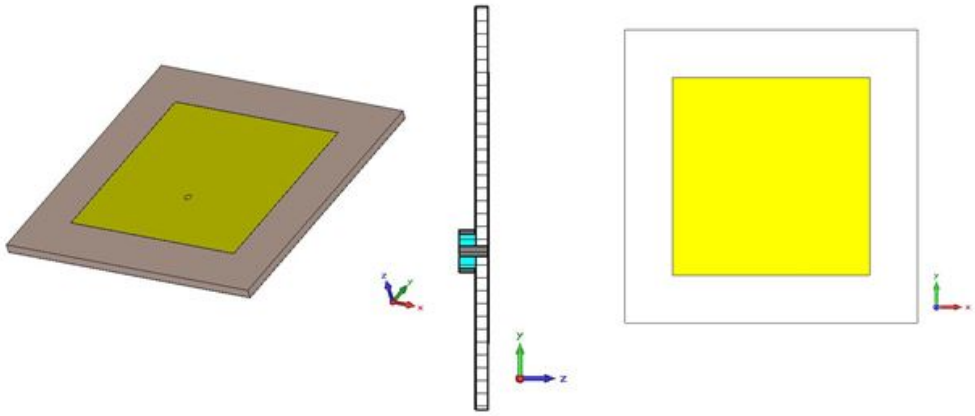

Figure 3.3: Cross-sectional view of a single microstrip patch antenna.

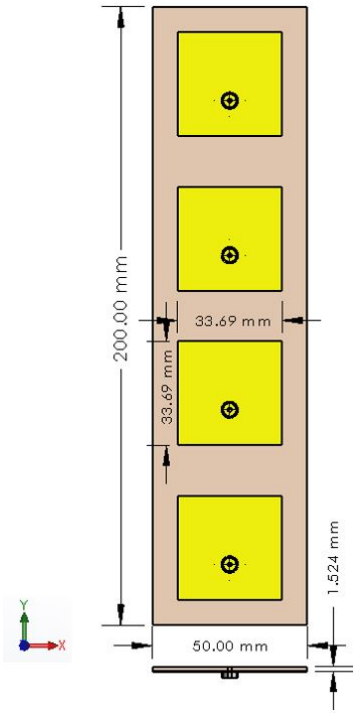

(a) 1×4 antenna array without gap

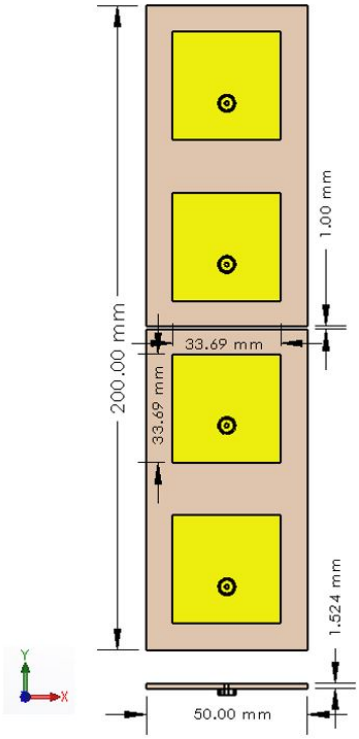

(b) 1 × 4 antenna array with a 1 mm gap

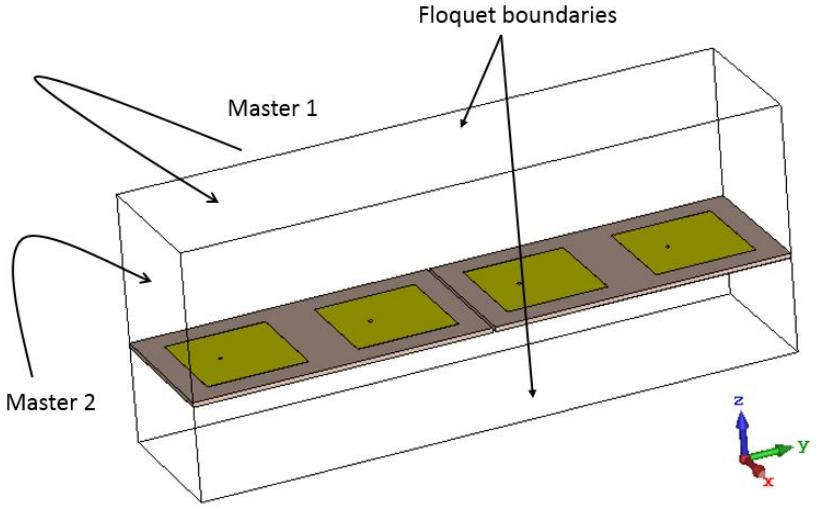

(c) Unit cell set up for 1 × 4 antenna array with a 1 mm gap

Figure 3.4: 1 × 4 array geometry.

The frequency range is chosen to be near the 2.6 GHz to 3 GHz band with a center frequency 2.85 GHz, to match the weather radar application. The substrate used in this model is the RT/Duroid 5880 (tm) with a dielectric constant of 2.2, a loss tangent of 0.0009, and a thickness of 1.524 mm. The size of the square patch antenna is set to be 33.69 mm $\times$ 33.69 mm in order to reasonably match the antenna at broadside at the center frequency. The feeding position is shifted from origin by 5.36 mm and fed by a 50-Ω coaxial cable through a probe feed. The copper thickness is chosen as 35 μm.

3.2.1 1×4 Antenna Sub-array Design

The square patch antenna was aligned and replicated along its E-plane as shown in Figure 3.4 to form a 1×4 array. Figure 3.4a shows the 1×4 array without a ground plane gap. In a separate simulation, a 1 mm gap, shown in Figure 3.4b, was added in between the patches to intentionally create a discontinuity of the currents in the ground plane and to represent a moderately-sized gap that may appear in a large phased array. The unit cell set for 1×4 are is depicted in Figure 3.4c. The simulations were run in a full wave solver by employing periodic boundary conditions mapped to specific scan angles. Each individual antenna element is excited by a TEM wave port. A total of 38 Floquet modes were used in this particular simulation. In general, the choice of these modes is based on the frequency, scanning angle, and sub-array unit cell size to ensure that all higher-order modes have enough attenuation to the Floquet ports ($>$ 40 dB) to ensure convergence of the solution. Here, the distance to the upper boundary is chosen to be 50 mm. Higher-order modes are ignored in order to ensure simulation efficiency and to ease the interpretation of results. The full S-parameters were generated for a θ_s angle of 30° for the three principle planes (E-plane, H-plane, and D-plane). Based on these S-parameters, the embedded element pattern, grating lobes, and active reflection coefficients are computed using the equations of the previous section in MATLAB.

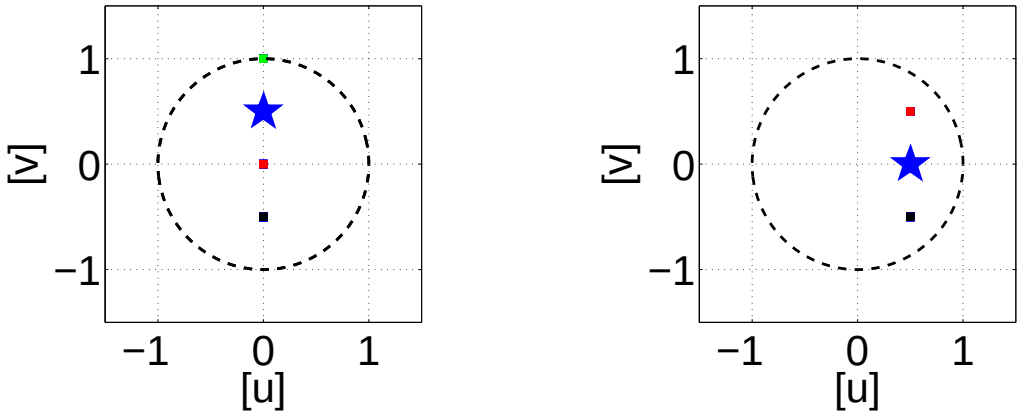

(a) E-plane

(b) H-plane

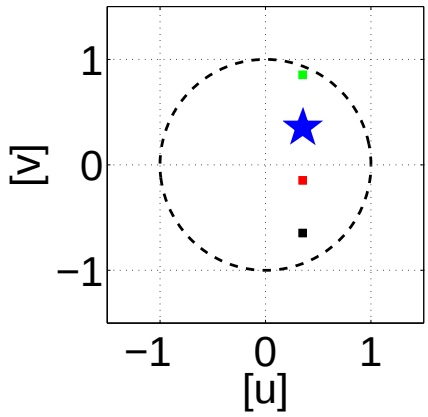

(c) D-plane

Figure 3.5: 1×4 array grating lobe locations (blue star indicates main beam location).

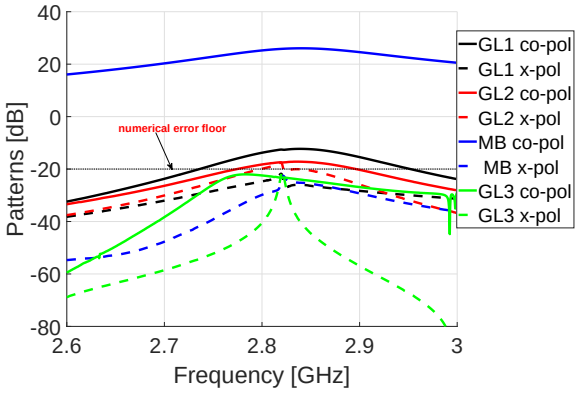

(a) E-plane without gap

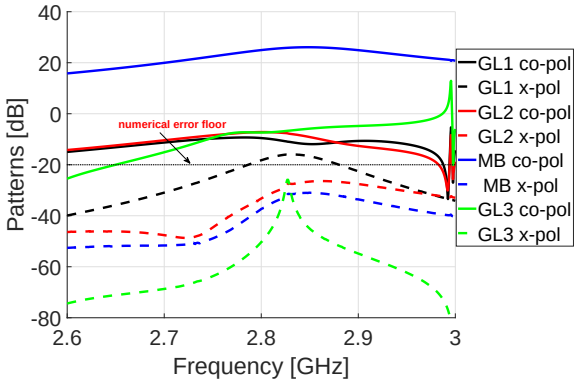

(b) E-plane with gap

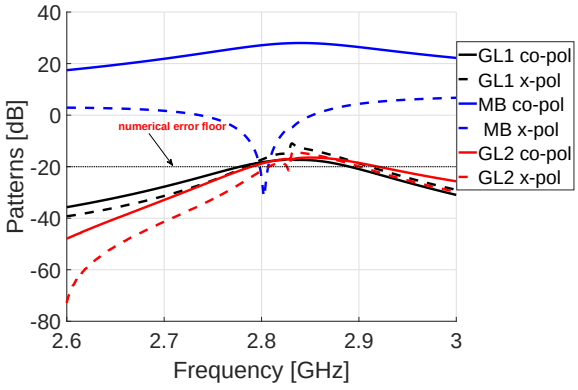

(c) H-plane without gap

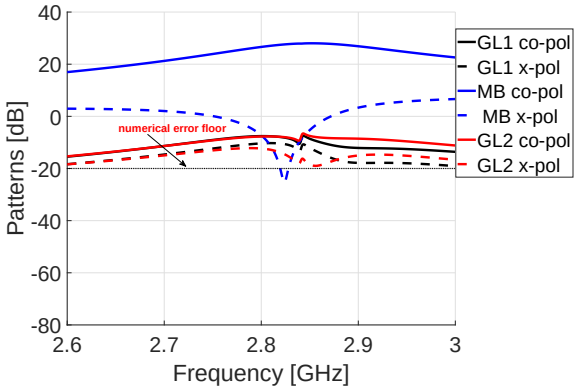

(d) H-plane with gap

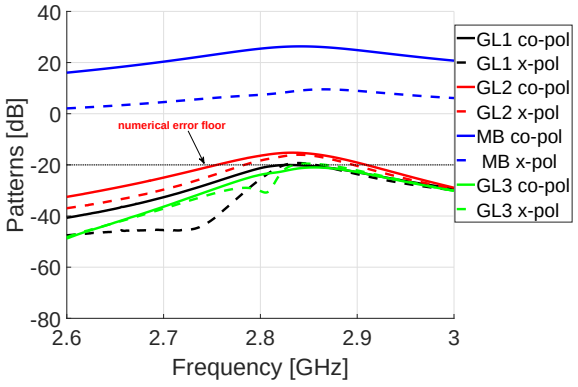

(e) D-plane without gap

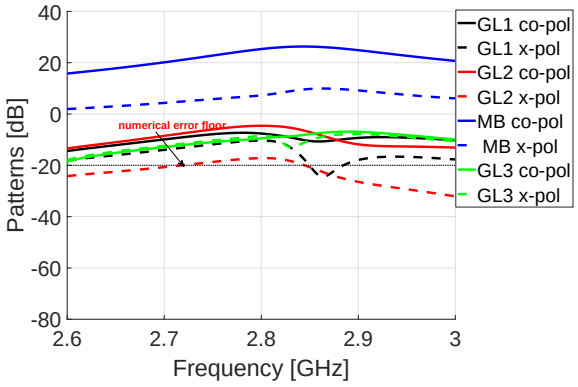

(f) D-plane with gap

Figure 3.6: 1×4 array radiated field patterns vs. frequency.

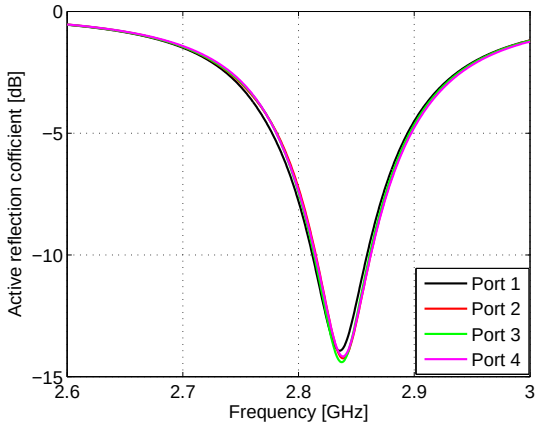

(a) E-plane without gap

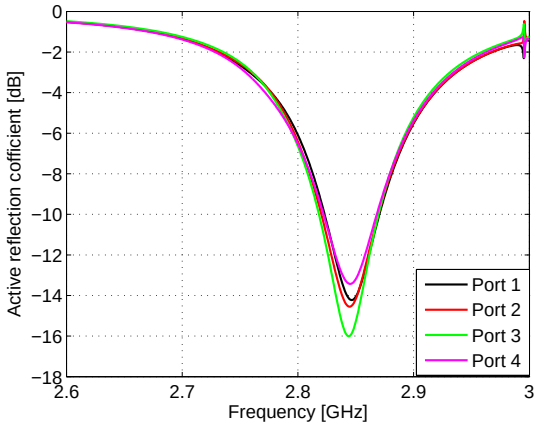

(b) E-plane with gap

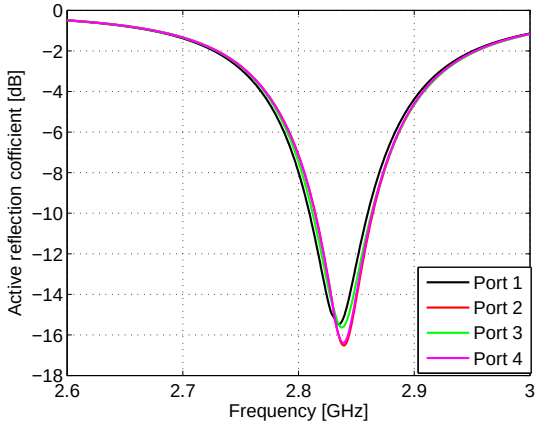

(c) H-plane without gap

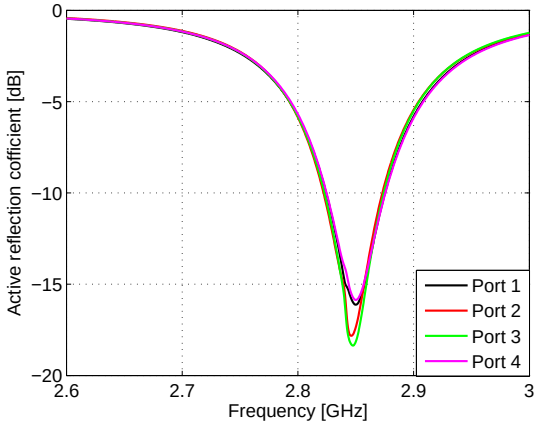

(d) H-plane with gap

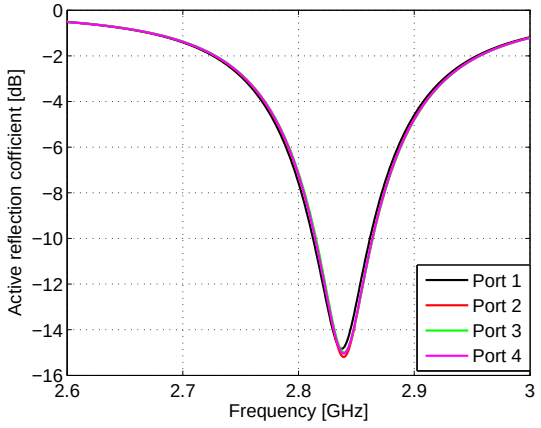

(e) D-plane without gap

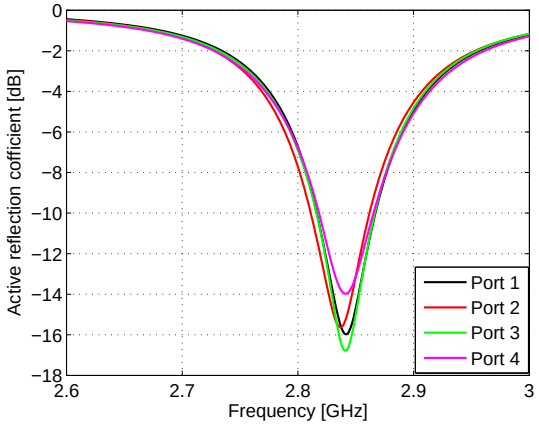

(f) D-plane with gap

Figure 3.7: 1×4 array active reflection coefficient.

3.2.2 Results

The grating lobe locations of these scan angles ($\phi_s = 90°, 0°, 45°$ for $\theta_s = 30°$) are plotted in Figure 3.5. There are four, three, and four grating lobes for the E-plane, H-plane, and D-plane scans, respectively. The radiated field patterns (normalized E-field) for all polarizations and grating lobes are shown in Figure 3.6. Due to the disruption of the ground plane, the grating lobe amplitudes emerged at least 5-dB in the E-and H-planes, with one of the E-plane grating lobes increasing to a significant level (30 dB). This is because the currents are strongest along this direction. Hence, a disruption there is most significant. For systems requiring very low sidelobes, this is clearly an issue. In the H-plane there is an obvious null in the cross-pol of the main beam. This is related to the way that mutual coupling effects manifest themselves along a direction where symmetry is violated by the non-differential probe feeding, whereas symmetry is largely maintained in the E-plane. Figure 3.7 shows the active reflection coefficients of every individual port. As expected, gaps created by the interruption of natural currents in the ground plane lead to different mutual couplings with respect to relative antenna positions. Therefore, the discrepancies are observed.

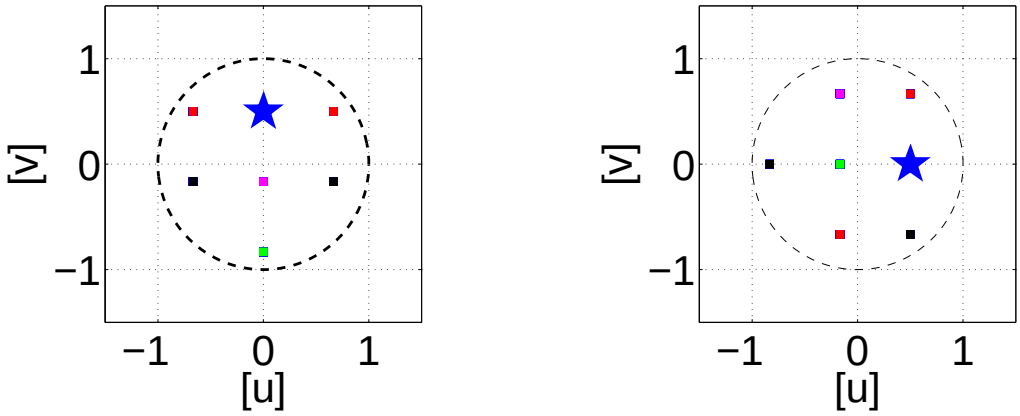

(a) E-plane

(b) H-plane

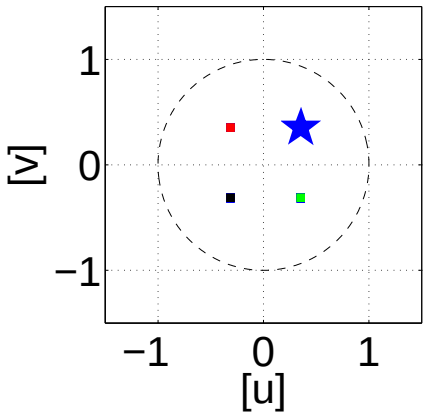

(c) D-plane

Figure 3.8: 3×3 array grating lobe locations (blue star indicates main beam location).

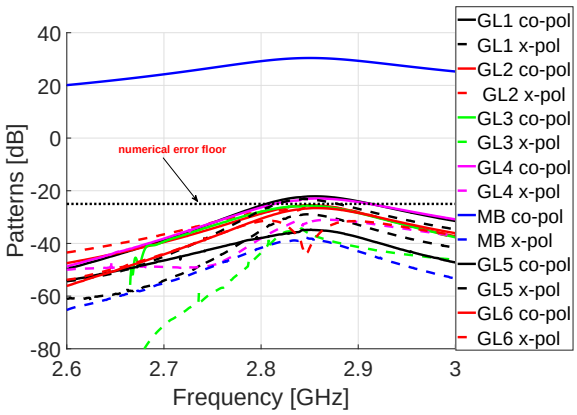

(a) E-plane without gap

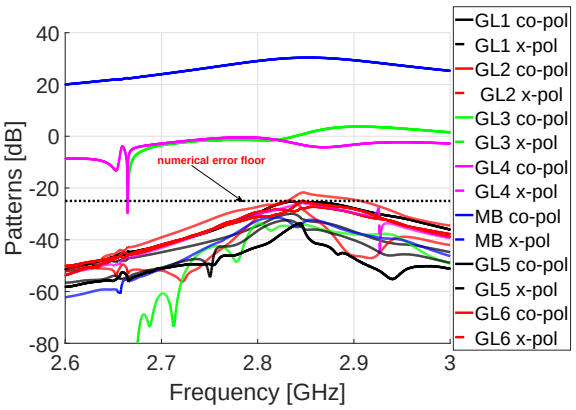

(b) E-plane with gap

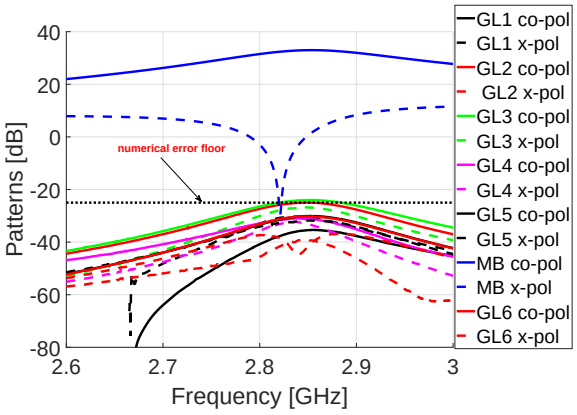

(c) H-plane without gap

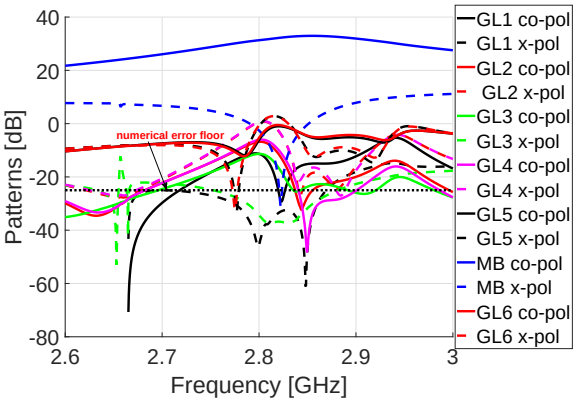

(d) H-plane with gap

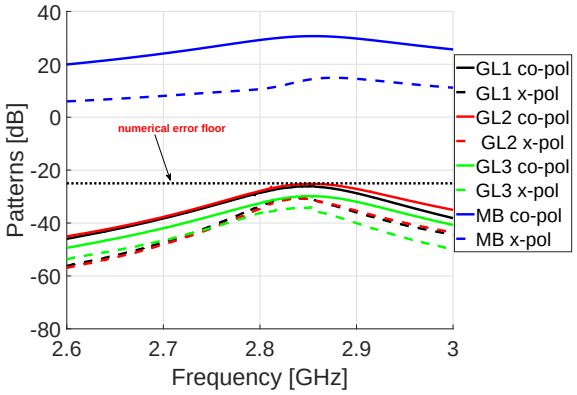

(e) D-plane without gap

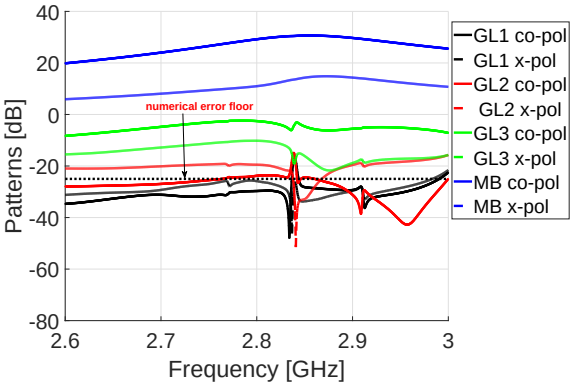

(f) D-plane with gap

Figure 3.9: 3×3 array radiated field patterns vs. frequency.

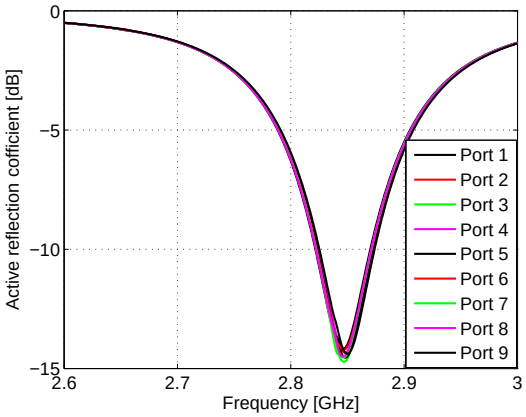

(a) E-plane without gap

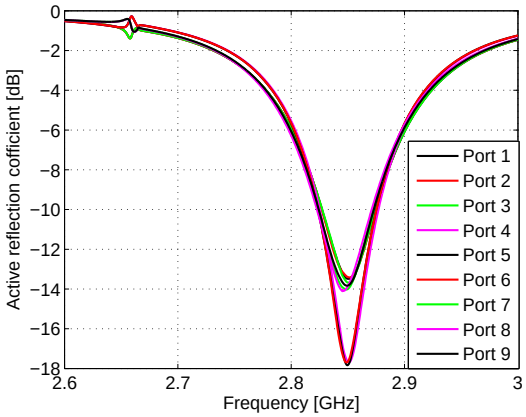

(b) E-plane with gap

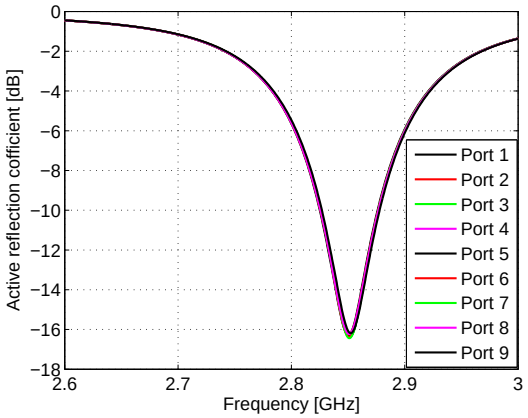

(c) H-plane without gap

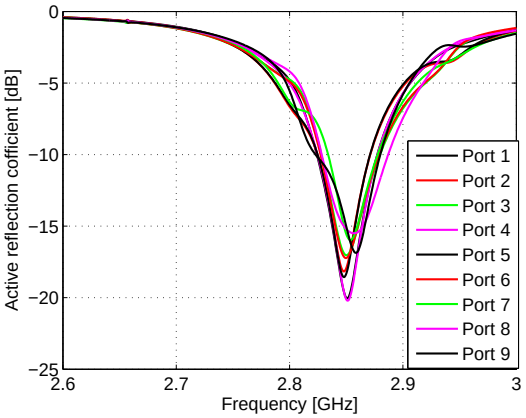

(d) H-plane with gap

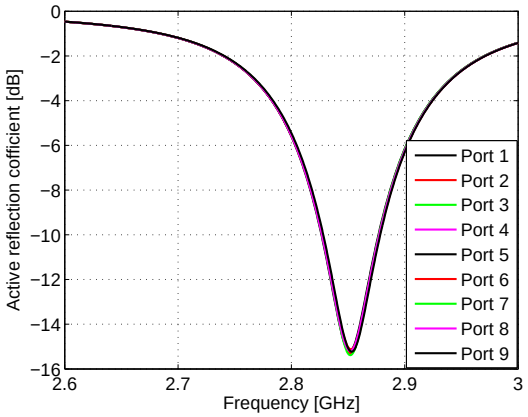

(e) D-plane without gap

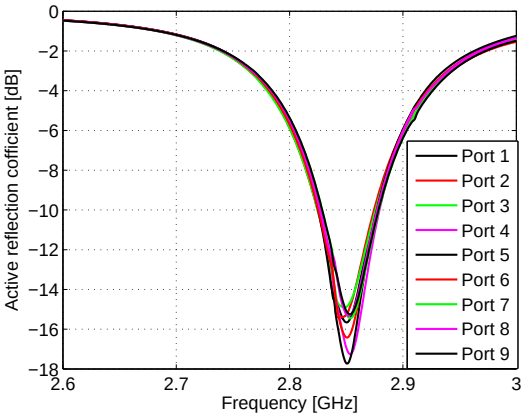

(f) D-plane with gap

Figure 3.10: 3×3 array active reflection coefficients.

3.3 3×3 Antenna Sub-array Design

To investigate a more general case where sub-arrays are arranged in a 2D lattice, a 3×3 array was also simulated. Figure 3.1 shows the geometry of a 3×3 array with and without disruption of the ground plane. The ground plane is again separated with a 1 mm gap, but this time along a square lattice, as shown in Figure 3.1. The analysis are performed with exactly the same approach as described for the 1×4 array. The upper z distance to the Floquet port is increased to 100 mm to further attenuate higher-order modes, allowing for a reduction to 32 Floquet modes with field convergence.

3.3.1 Results

The variation of the active element pattern is again studied for the 3×3 sub-array case. The effects of gaps in the ground plane and subsequent variations in mutual coupling are more apparent in the 3×3 array. In Figure 3.8, the relevant grating lobe locations are plotted. For E-plane and H-plane scanning there are six grating lobes, and in the D-plane there are only four grating lobes. Like the 1×4 array, the rise of grating lobe amplitudes is even more evident in the 3×3 case, as shown in Figure 3.9. Figure 3.10 shows the active reflection coefficients in each case for each antenna within the sub-array.

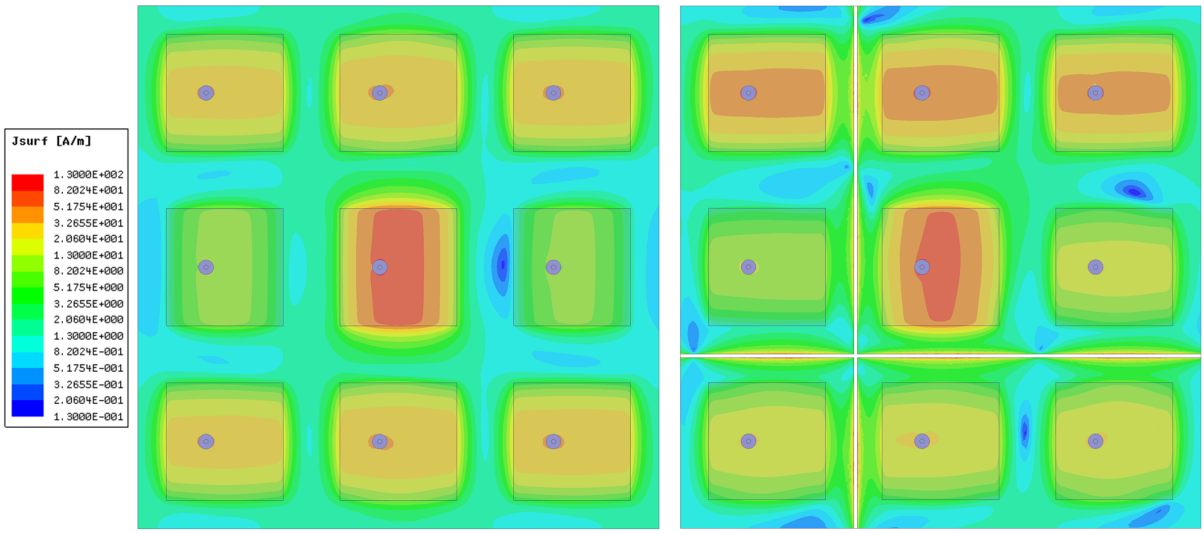

Figure 3.11: Current density of 3×3 array, (left) without a ground plane gap and (right) with a 1 mm gap.

Interruption of current propagation due to the gap is shown in Figure 3.11, where the absolute value of the complex surface current is plotted on a logarithmic scale covering 60 dB. It is obvious from the graph that the flow of current gets disrupted at the gaps, and that interruption is the principal contributor to the grating lobes. It can also be seen that the current distribution under the non-driven patches is also changed as a result of the perturbed mutual coupling. This also perturbs the resulting Floquet mode parameters and, therefore, the resulting grating lobes.

4

Practical Demonstration Verification and Impact on Future Weather Radar

The standard Floquet modal analysis of infinite arrays of finite sized sub-arrays has been studied through a rigorous mathematical framework and presented in the previous chapter. This Floquet framework, however, has not been validated through measurements. To corroborate the overall theory, this chapter presents measurements of an array of $1.5\lambda \times 1.5\lambda$ sub-arrays of simple patch antennas, quantifying the grating lobe and the grating lobe effects. The measurements are accomplished carefully in a planar near-field anechoic chamber. These efforts will eventually be helpful to predict the performance of next generation digital phased array radars, which requires much more complex geometries without building the array first.

In the previous chapter the antenna was designed and studied for $S-$band. In order to verify the theoretical findings, we need a reasonably moderate sized antenna array. Within the fabrication facilities of Advanced Radar Research Center at University of Oklahoma, we can fabricate the reasonably moderate sized antenna array, if we switch to a higher frequency band. Therefore, the frequency band is switched from S-band to X-band with a center frequency near 10 GHz, in order to operate at a frequency where the array could be large enough to capture large-array effects with readily-available coaxial connectors, while being small enough to prototype and measure. The substrate was Rogers R04350B,

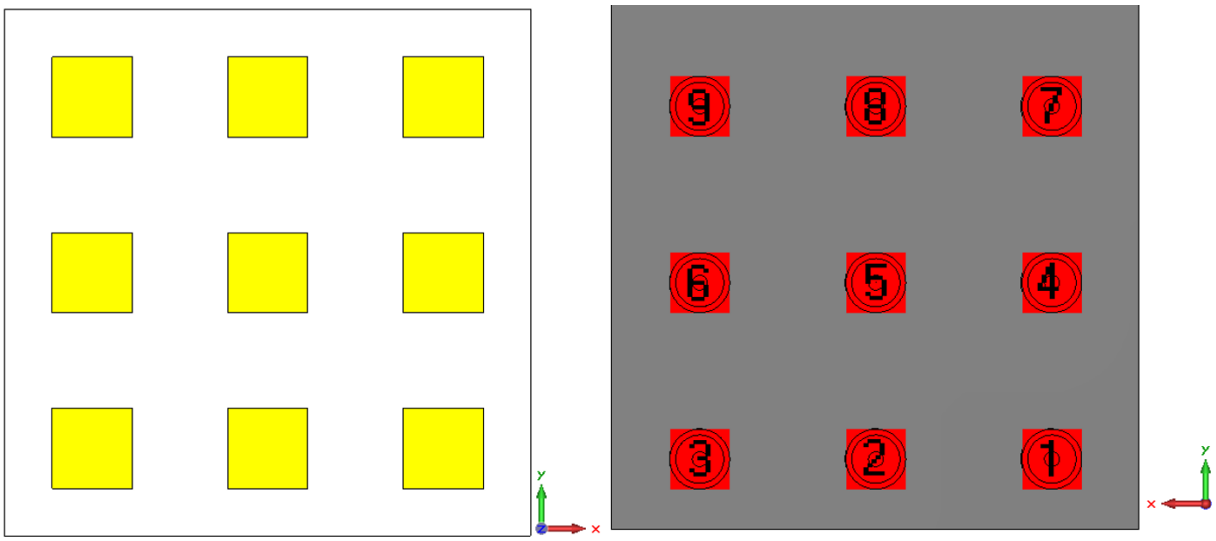

Figure 4.1: Top and bottom view of 3×3 sub-array with port numbers.

with a dielectric constant of 3.66, a loss tangent of 0.004, and a thickness of 1.524 mm. The size of each patch is set to be 6.86 $\times$ 6.86 mm in order to reasonably match the array at broadside at the center frequency with a feeding position of 1.5 mm from the patch center. Each element is fed by a 50 Ω SMA connector through a probe feed. The copper thickness is chosen to be 35 μm. The elements are spaced on a 15 mm grid with 15 elements along the H-plane and 27 elements along the E-plane. In one simulation and board, the ground plane is continuous, and in a separate simulation, a 1 mm gap is added in the ground plane between each 3 $\times$ 3 sub-array to intentionally create a discontinuity. This truncation is representative of a significant gap that may appear during integration of many sub-arrays in a large phased array system. Figure 4.1 shows the top and bottom view of the 3 $\times$ 3 sub-array and the port numbers for each element according to their relative space. The array is assumed herein to be on the x-z plane.

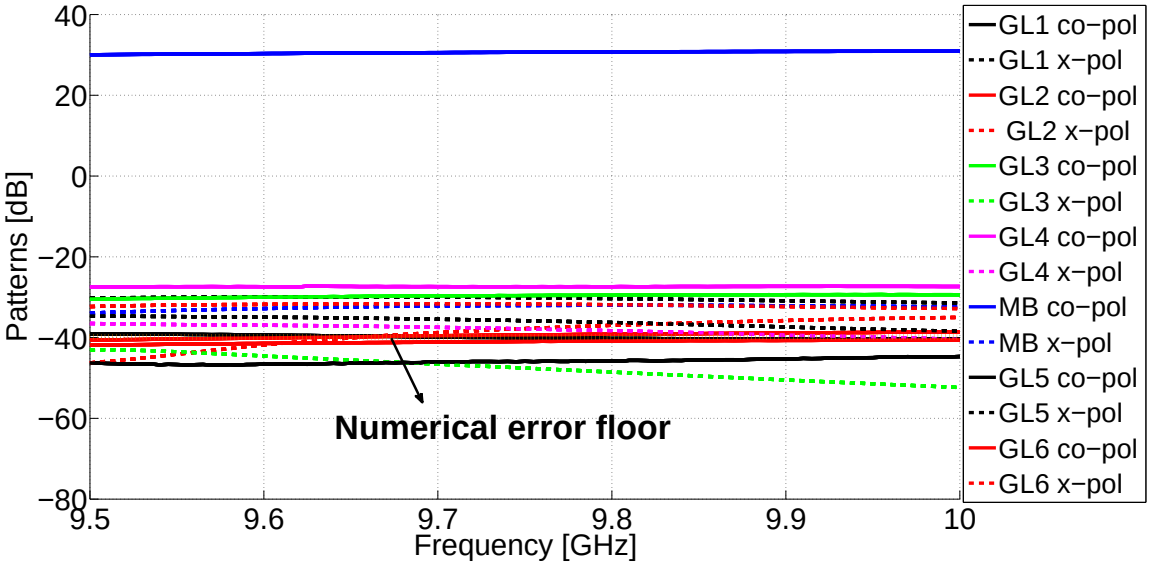

(a) E-plane without gap

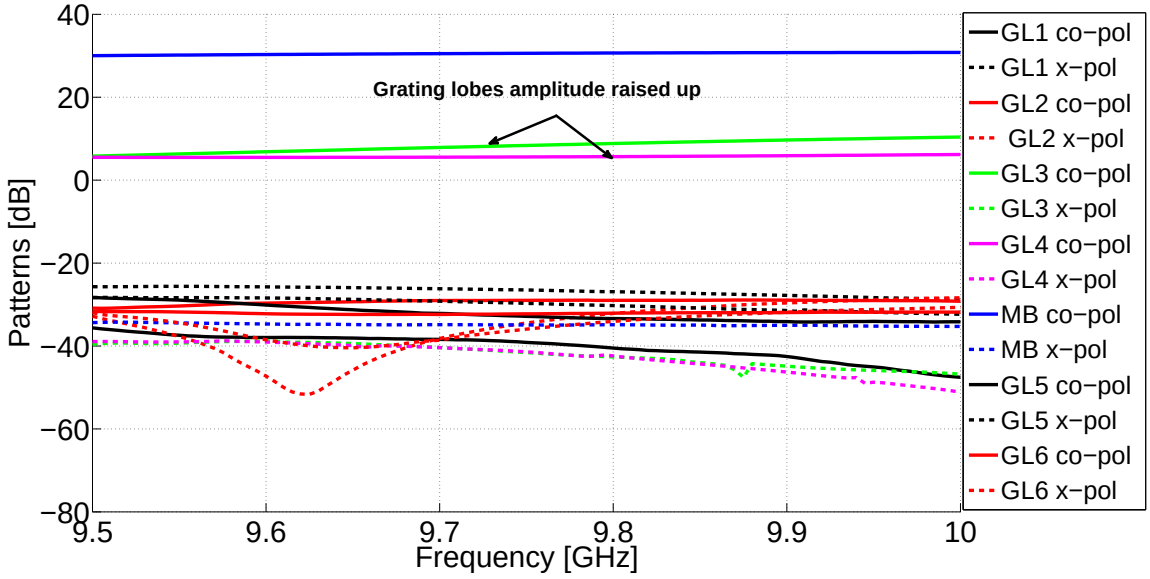

(b) E-plane with a 1 mm gap in ground plane

Figure 4.2: $1.5\lambda \times 1.5\lambda$ array radiated field vs. frequency at 30° scan for E-plane.

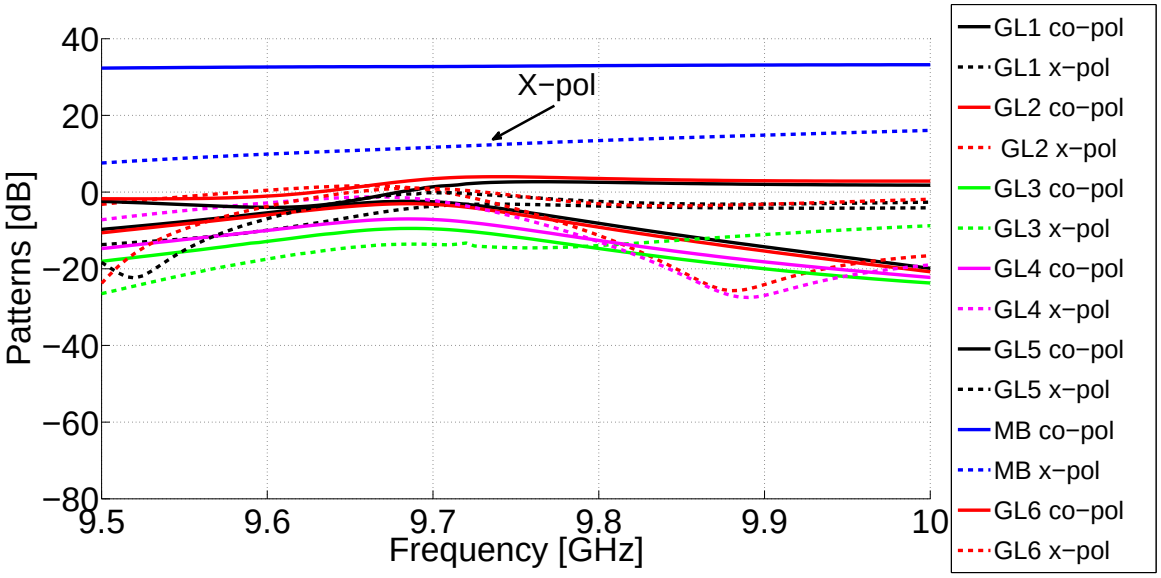

(a) H-plane with a 1 mm gap in ground plane

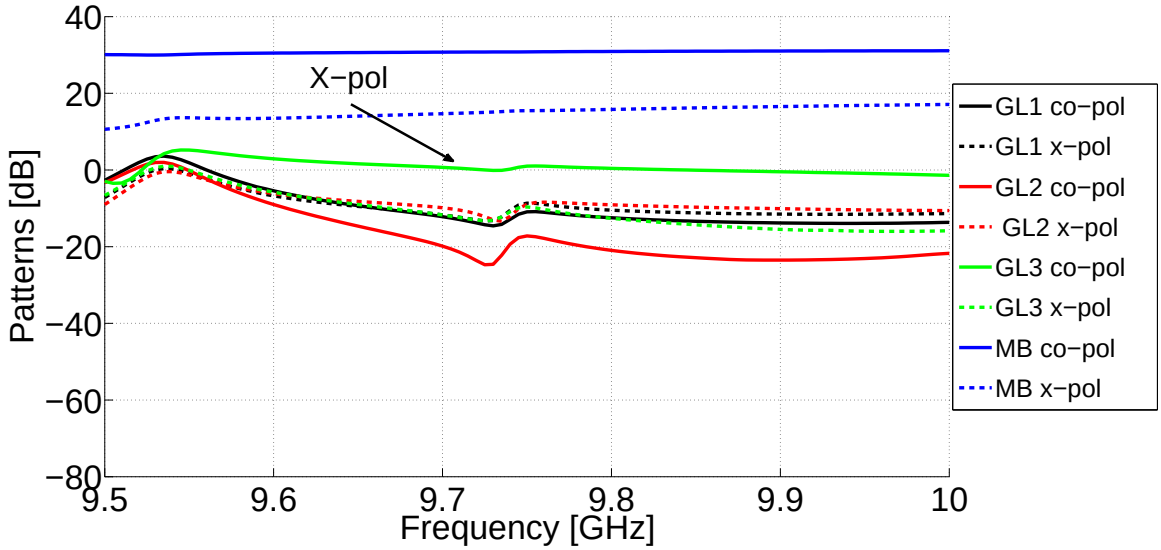

(b) D-plane with a 1 mm gap in ground plane

Figure 4.3: $1.5\lambda \times 1.5\lambda$ array radiated field vs. frequency at 30° scan.

Figure 4.2 compares the radiated field pattern (normalized E-field) for all polarization and grating lobes for two different cases (without a 1 mm gap in the ground plane and with a 1 mm gap in between the sub-arrays). The grating lobe levels calculated here are representative of residual numerical errors in HFSS, and their levels are shown in Figure 4.2. There are a total of six grating lobes, and, due to disruption of the current in the ground plane, some of the grating lobes emerged at more than -30 dBc, as shown in Figure 4.2b. Such a grating lobe would be significant in a system requiring low sidelobe levels.

The normalized H-plane and D-plane field patterns for all polarizations and grating lobes are showed in Figure 4.3. As shown in Figure 4.3, some of the grating lobes' amplitude also raised up for both planes. This is the similar behavior we have observed for E-plane scan.

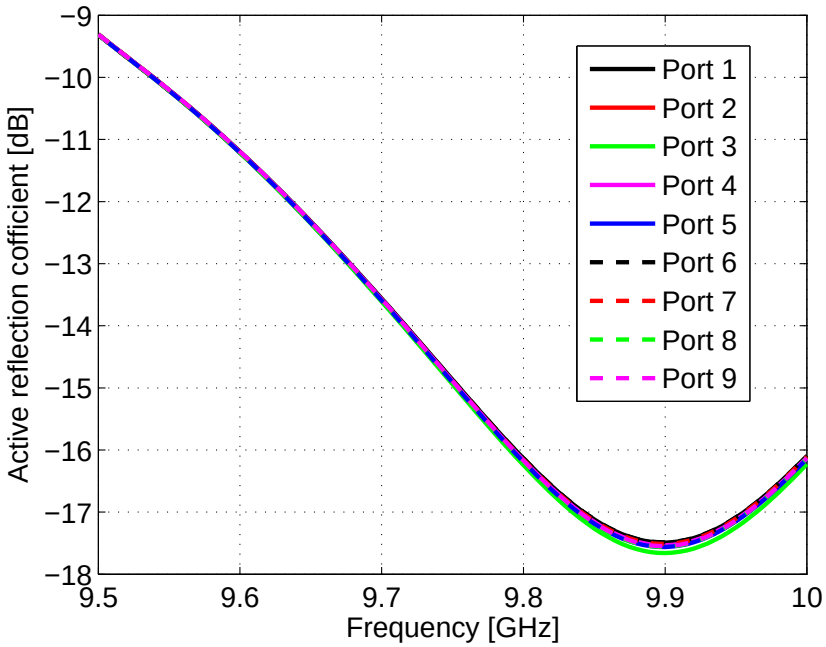

(a) E-plane without gap

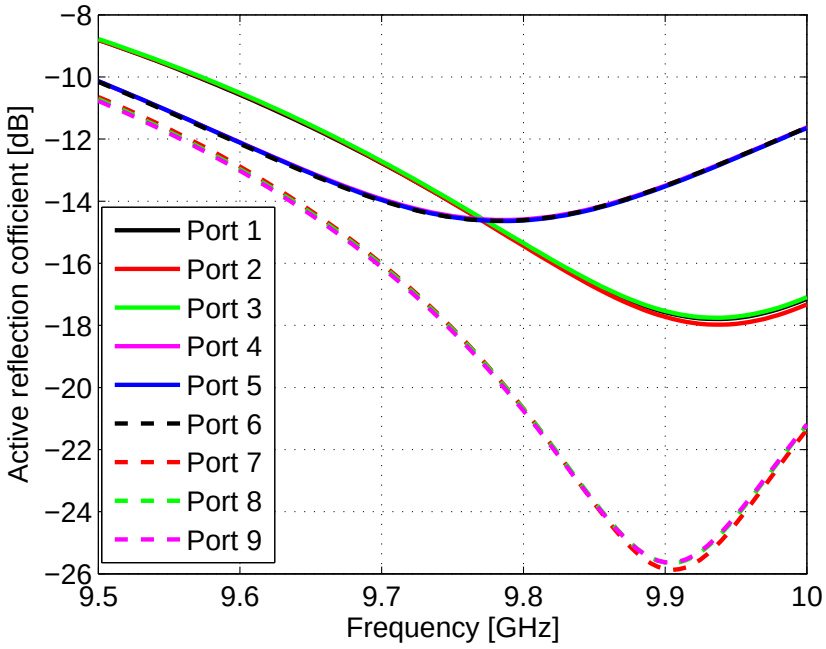

(b) E-plane with 1 mm gap in ground plane

Figure 4.4: Active reflection coefficient of 3 × 3 array.

The variation of the active reflection coefficient for each element in a 3×3 sub-array is shown in Figure 4.4. The effect of gaps in the ground plane and subsequent variations in mutual coupling are apparent in the 3×3 array. The active reflection coefficient varies from element to element due to the 1 mm gap in the ground plane, as shown in Figure 4.4b. When there is no gap, as depicted in Figure 4.4a, all the elements in the array will see similar mutual coupling environments, so the active reflection coefficients for all ports would be same. Where there is a gap, as explained earlier, this is not the case instead, all ports will see different mutual coupling environment so the active reflection coefficients will also be different.

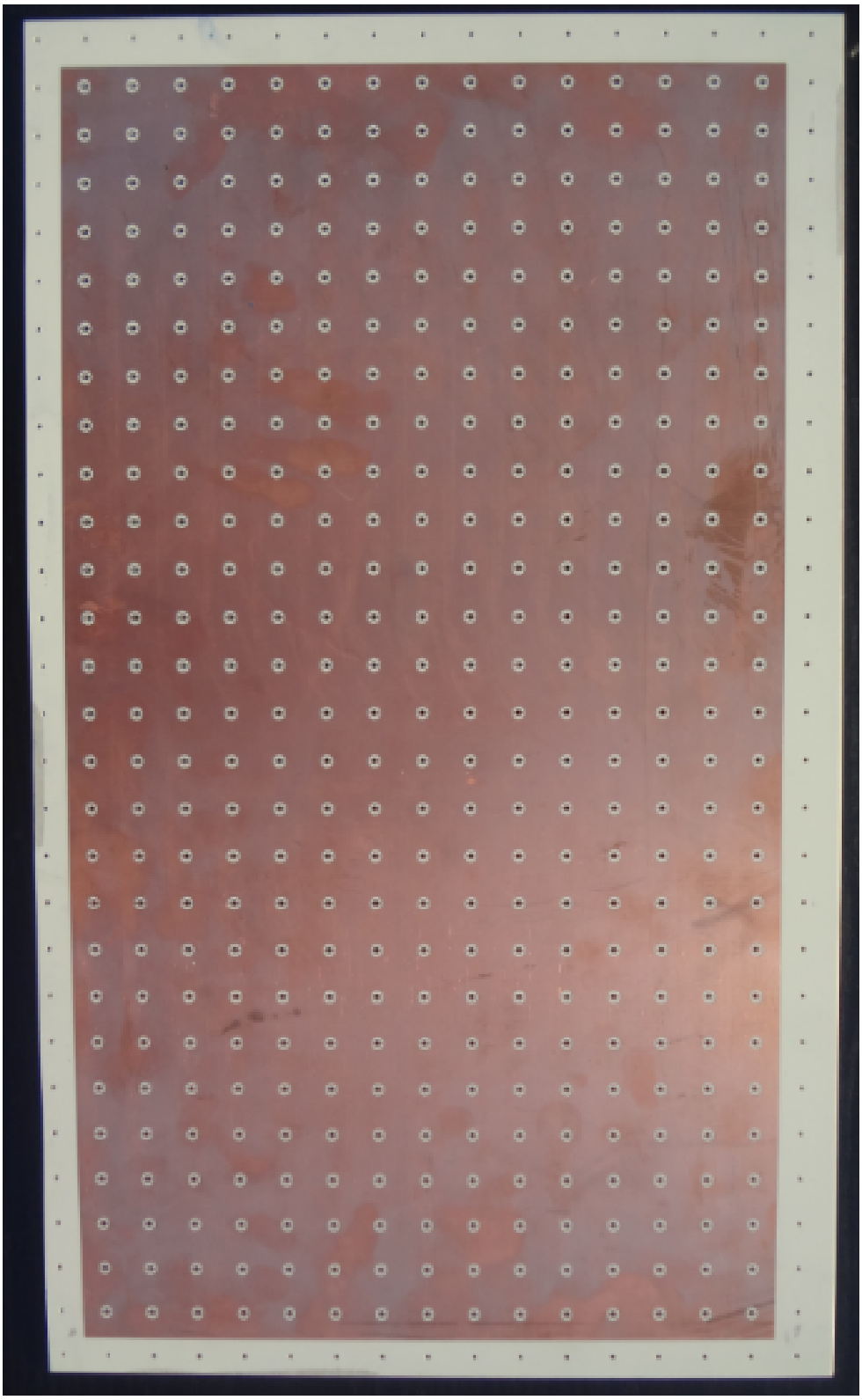

Figure 4.5: Bottom view of the antenna array without gap.

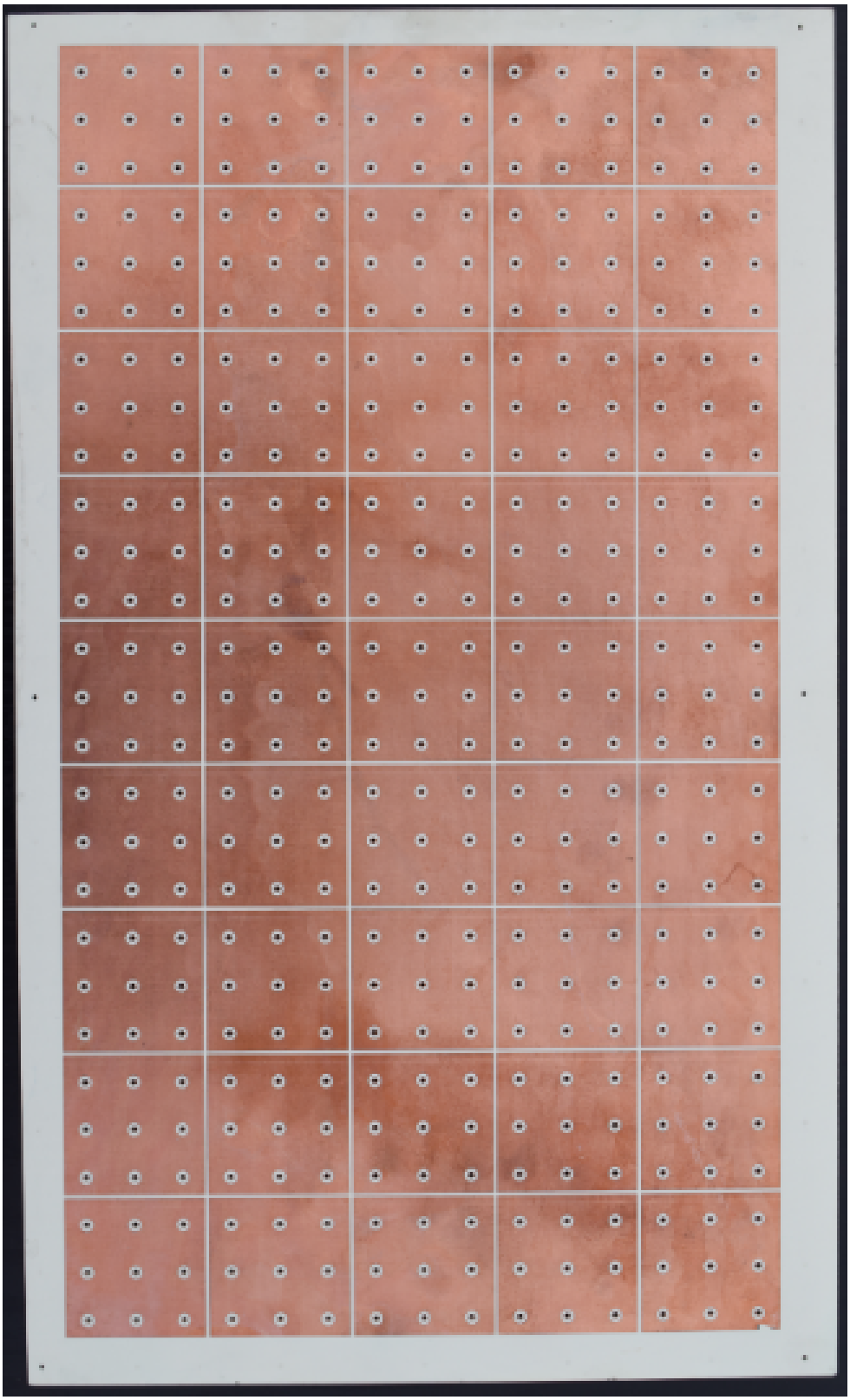

Figure 4.6: Bottom view of the antenna array with a 1 mm gap between sub-arrays.

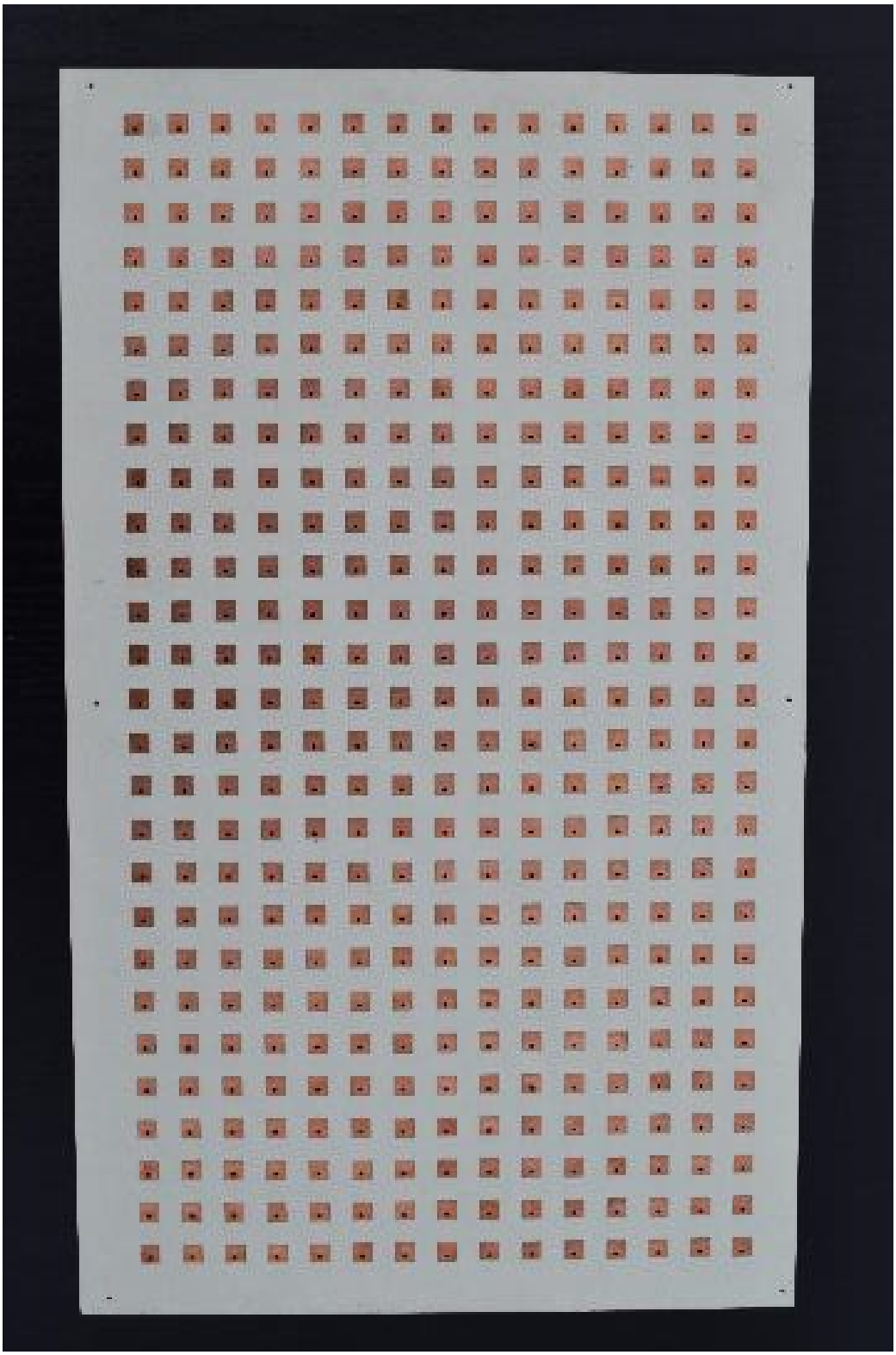

Figure 4.7: Front view of the antenna array.

4.1 Fabrication Efforts

Figure 4.5, Figure 4.6 and Figure 4.7 show bottom and front views of the fabricated 9 $\times$ 5 antenna array. Each sub-array contains 3 $\times$ 3 elements. There are in total 405 elements of square patch antennas. This represents the largest array that could be fabricated in-house, and this size is thus as close a representation to an infinite array as possible. A wet etching method and photo lithography were used to fabricate the antenna array. Ideally, all elements are identical, and the mutual coupling is periodic between the sub-arrays; however, finite "array of sub-array" effects and fabrication errors will inevitably provide a practical measurement limit.

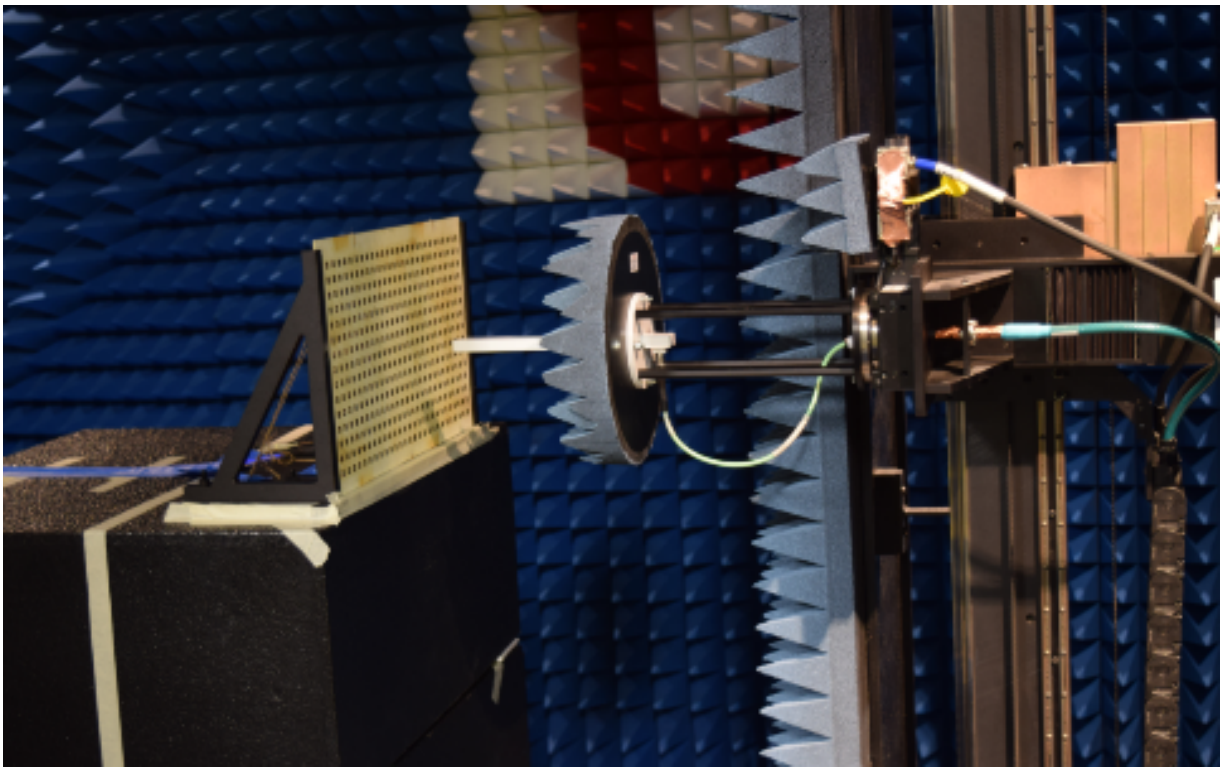

Figure 4.8: Test fixture of the measurement set up.

The individual feed points of the antenna are terminated with 50 Ω coaxial feed, and 50 Ω matched loads were attached to provide a proper coupling environment. The central

three sub-arrays were measured in the near field chamber of the Advanced Radar Research Center at University of Oklahoma.

The test fixture of the array measurements is depicted in Figure 4.8. An OEWG X-band probe was used as a source antenna (transmitter). The probe and array were separated by approximately 2λ (2.402 inches) to get the proper near field data. The central 3×9 elements (1×3 sub-arrays of 3×3 elements) were measured in order to validate the overall theory based on individual and average behavior of these sub-arrays.

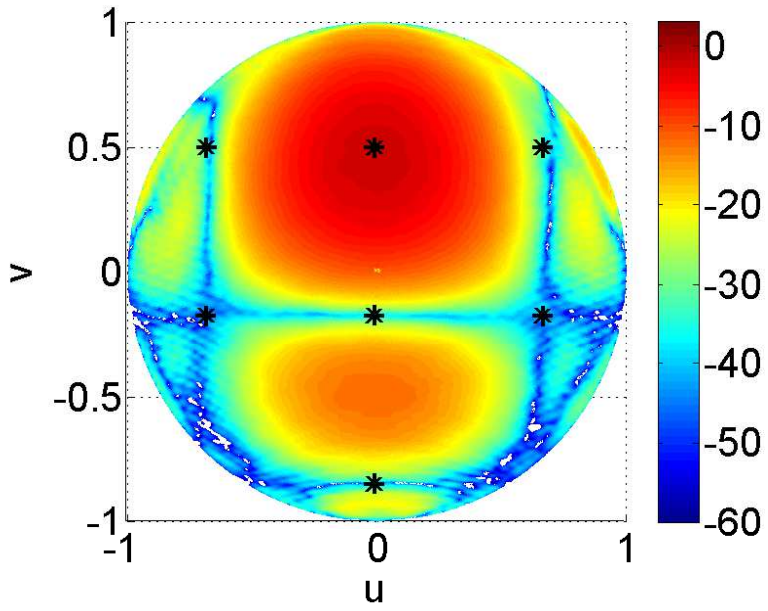

(a) Center sub-array without gap

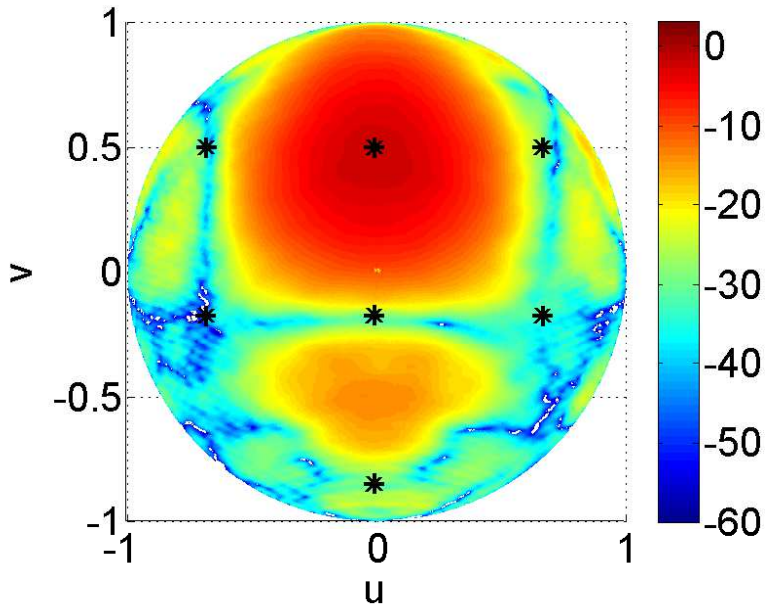

(b) Center sub-array with gap

Figure 4.9: E-plane scanning sub-array element pattern [dB] (the black asterisks ($*$) indicate grating lobe locations).

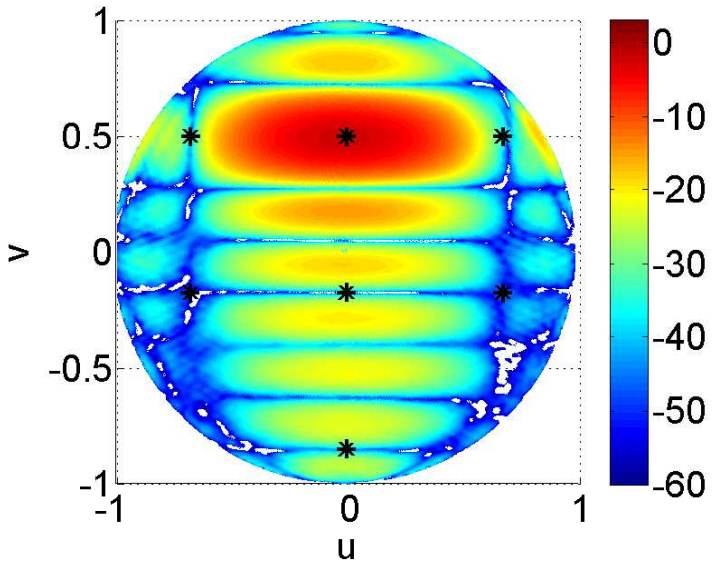

(a) Combined sub-arrays without gap

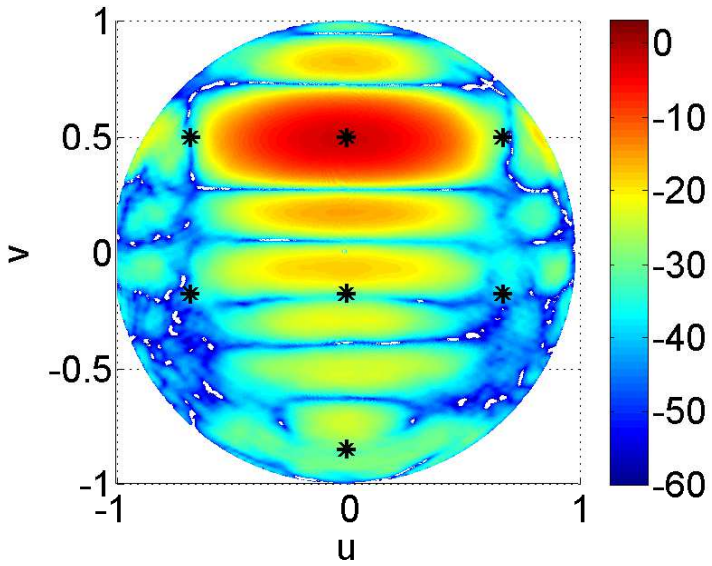

(b) Combined sub-arrays with gap

Figure 4.10: E-plane scanning sub-array element pattern [dB] (the black asterisks ($*$) indicate grating lobe locations).

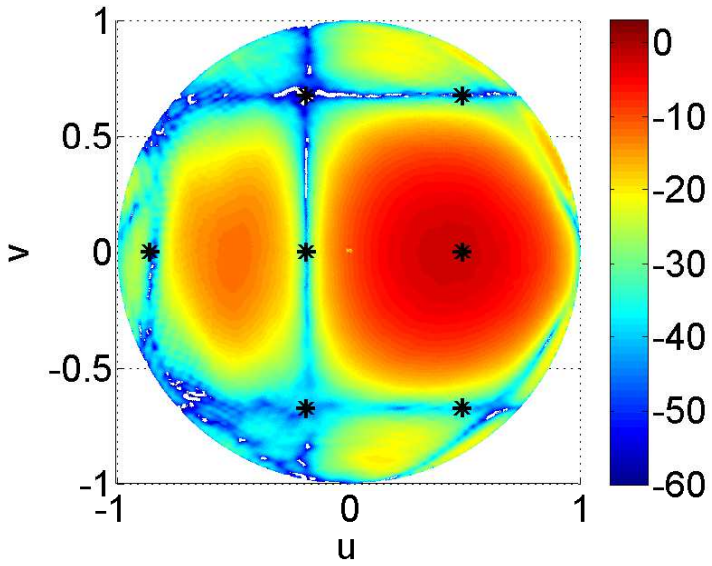

(a) Center sub-array without gap

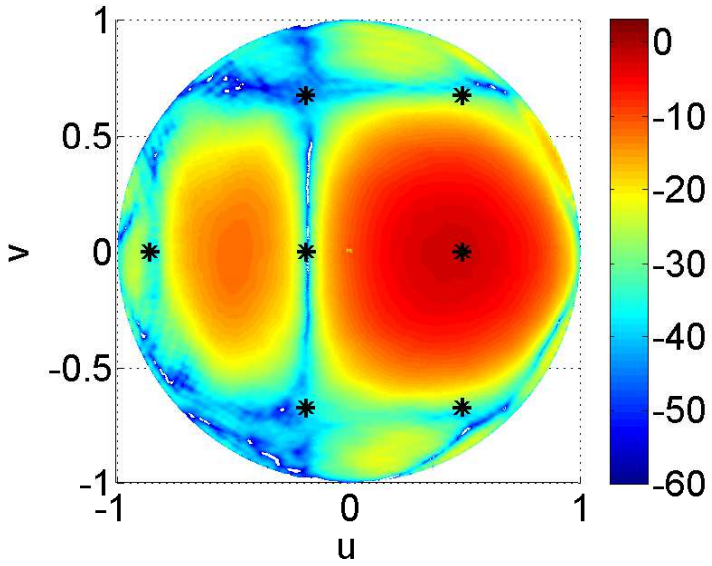

(b) Center sub-array with gap

Figure 4.11: H-plane scanning sub-array element pattern [dB] (the black asterisks ($*$) indicate grating lobe locations).

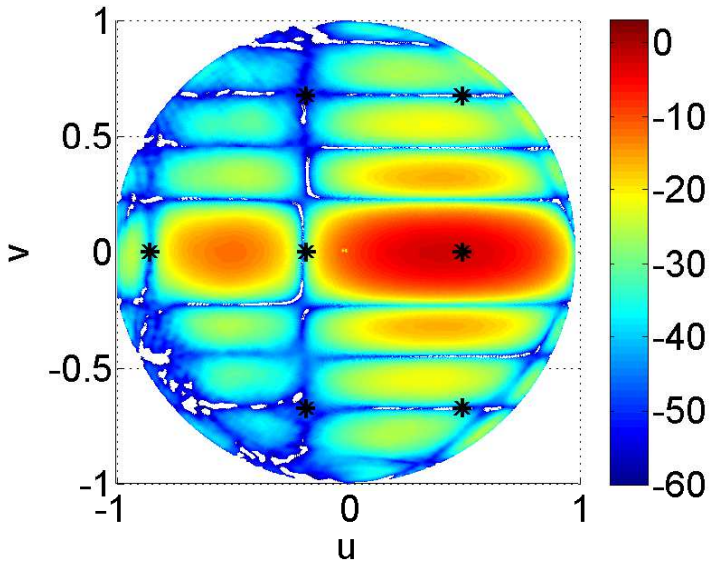

(a) Combined sub-arrays without gap

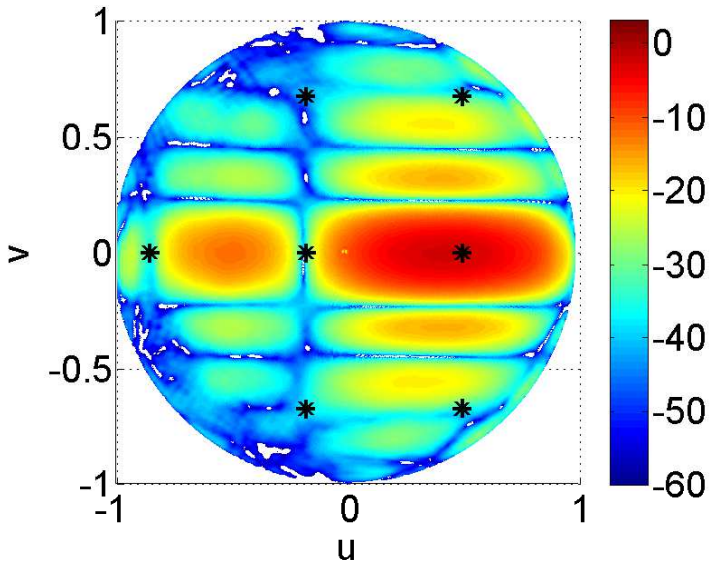

(b) Combined sub-arrays with gap

Figure 4.12: H-plane scanning sub-array element pattern [dB] (the black asterisks ($*$) indicate grating lobe locations).

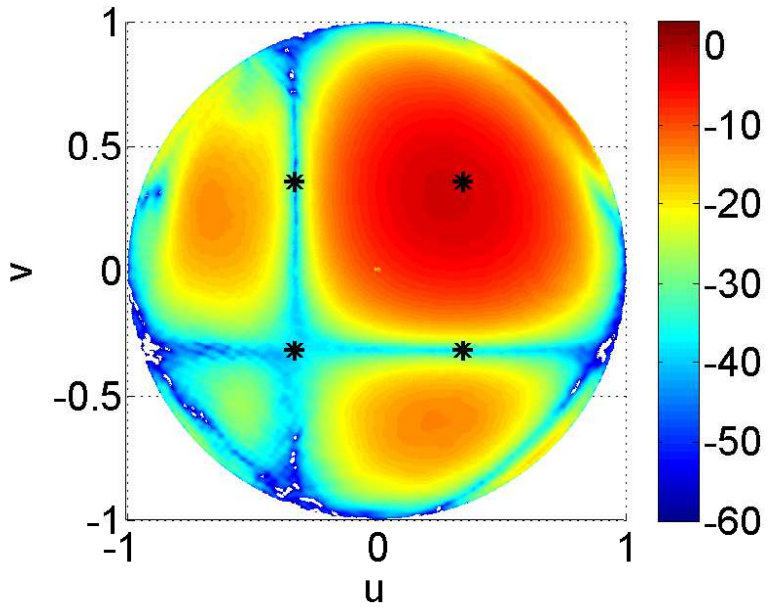

(a) Center sub-array without gap

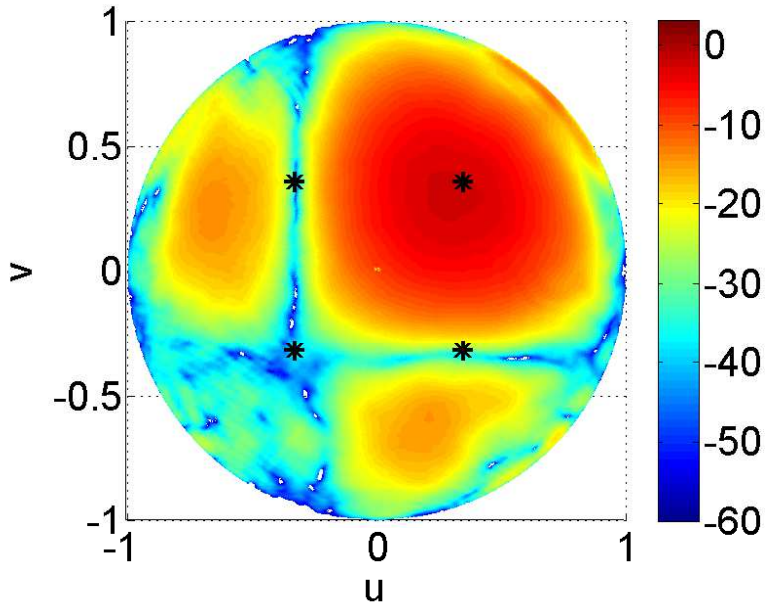

(b) Center sub-array with gap

Figure 4.13: D-plane scanning sub-array element pattern [dB] (the black asterisks ($*$) indicate grating lobe locations).

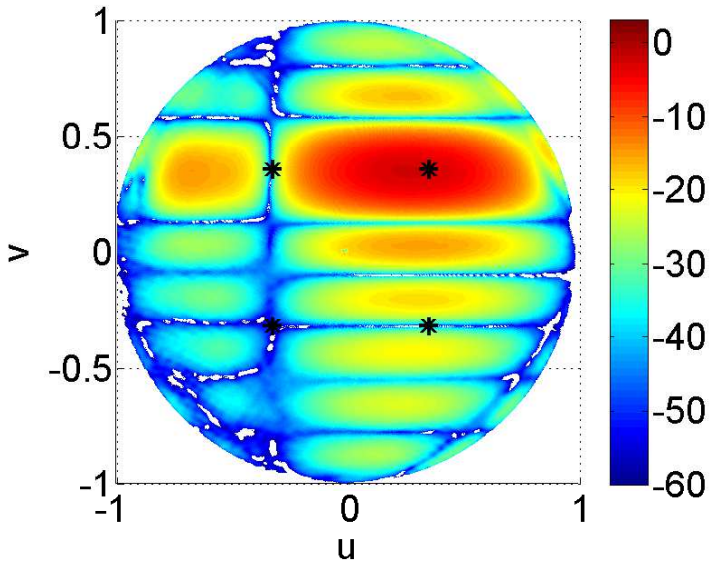

(a) Combined sub-arrays without gap

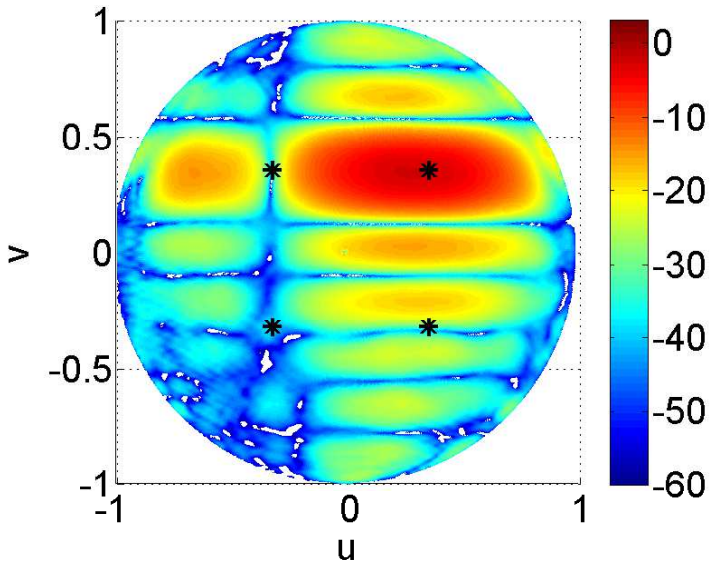

(b) Combined sub-arrays with gap

Figure 4.14: D-plane scanning sub-array element pattern [dB] (the black asterisks ($*$) indicate grating lobe locations).

4.2 Measurements

The measurement results of the embedded sub-array patterns of E-plane scanning for center and combined sub-arrays at 30° are shown in Figure 4.9 and Figure 4.10. These types of plots are a hemispherical projection of three-dimensional space on a two-dimensional surface. The black stars in the plots are the calculated grating lobe locations. It is clearly visible that the grating lobe was raised up due to the gap in the ground plane. It is more visible when all the elements are combined. Figure 4.11 and Figure 4.12 exemplify the embedded element sub-array patterns of H-plane scanning for center and combined sub-array, respectively. A similar trend is observed in the H-plane as well. The D-plane embedded sub-array patterns comparison, shown in Figure 4.13 and Figure 4.14, does not exhibit grating lobes that are as significant as in the E-plane. Certainly, the grating lobes level increased for all cases.

Table 4.1: SUMMARY AND COMPARISON OF SIMULATED AND MEASUREMENT RESULTS

			Dominant grating lobe level		
			E-plane [dB] (u,v)	H-plane [dB] (u,v)	D-plane [dB] (u,v)
Simulated	Unit Cell	Without gap	60.26 (0,-0.85) 58.17 (0,-0.18)	64.58 (-0.85,0)	61.68 (-0.32,0.35)
		With gap	21.375 (0,-0.85) 24.95 (0,-0.18)	30.89 (-0.85,0)	31.12 (-0.32,0.35)
Measured	Left subarray	Without gap	29.34 (0,-0.85) 34.70 (0,-0.18)	29.41 (-0.85,0)	33.54 (-0.32,0.35)
		With gap	24.86 (0, -0.85) 30.17 (0,-0.18)	31.25 (-0.85,0)	29.03 (-0.32,0.35)
	Center subarray	Without gap	38.12 (0,-0.85) 34.92 (0,-0.18)	47.62 (-0.85,0)	34.07 (-0.32,0.35)
		With gap	27.94 (0,-0.85) 27.69 (0,-0.18)	38.96 (-0.85,0)	26.14 (-0.32,0.35)
	Right subarray	Without gap	36.61 (0, -0.85) 33.76 (0,-0.18)	29.51 (-0.85,0)	31.11 (-0.32,0.35)
		With gap	28.88 (0,-0.85) 28.40 (0, -0.18)	26.20 (-0.85,0)	26.29 (-0.32,0.35)
	Combined subarrays	Without gap	38.28 (0,-0.85) 48.26 (0, -0.18)	39.47 (-0.85,0)	50.34 (-0.32,0.35)
		With gap	27.69 (0,-0.85) 28.97 (0, -0.18)	33.06 (-0.85,0)	27.95 (-0.32,0.35)

4.3 Comparison between Simulation and Measurement Results

The comparison between simulation and measured results between different sub-arrays have been summarized in Table. 4.1. From the simulation results it is evident that the grating lobe amplitude level emerged to around 25 dB in the E-plane scan and E-plane grating lobes. This is due to current disruption in the ground plane gap and it is very strong in the E-plane. The other scan angles and planes show a less significant effect.

The measured results also show similar characteristics, but in the case of the E-plane the measurements do not show as drastic of a rise in grating lobes in the worst case. It

is speculated that the variability in the (hand-) manufacturing of each connector, load, and solder connection prohibits a purely constructive addition of these more dominant grating lobe effects. Further testing of other non-central sub-arrays are underway to better understand these limitations. It is evident from the combined sub-array results that the increases in radiation due to the gaps are not only visible at the precise grating lobe locations but all along the corresponding ridges in (u, v)-space as well. Phase stability between measurements was a concern at first, but it was found that the phase did not vary in repeated measurements more than a few degrees (which maps to an error floor of around -50 dBc in these measurements for a single sub-array). However, because small alignment errors will drastically impact the measured level of smaller grating lobe effects, careful post-processing and measurement re-alignment will be investigated to explore the limitations due to this non-ideality as well.

4.4 Further Analysis

Using Floquet modal analysis, we were able to extract the grating lobes radiation pattern for the finite sized sub-arrays. We found that due to the gap some of the grating lobes amplitude raised up. Since the gap is the only source for the disruption of natural currents, the issue is how we can represent the grating lobes in terms of gap currents for each grating lobe location for particular scan angles. To answer this question, we need to formulate the gap current as a slot magnetic current. Since this type of antenna is aperture antenna, we used aperture analysis techniques to analyze the antennas.

Aperture antennas can be analyzed either in spatial domain or in spectral domain. In spatial domain the analysis is very complex. However, spectral domain it can be simplified. To analyze it in the spectral domain we have two choices as noted in equations 4.1.

$$\underline{A} = \underline{\hat{z}} A_z(x,y,z) \qquad \nabla^2 A_z + k_0^2 A_z = 0 \tag{4.1a}$$

$$\underline{F} = \underline{\hat{z}} F_z(x,y,z) \qquad \nabla^2 A_z + k_0^2 F_z = 0 \tag{4.1b}$$

Induce the Fourier transform

$$\tilde{A}_z(k_x,k_y,Z) = \int_{-\infty}^{+\infty}\int_{-\infty}^{+\infty} A_z(x,y,Z) e^{-j(k_x x + k_y y)} dxdy \tag{4.2}$$

$$A_z(x,y,Z) = \frac{1}{(2\pi)^2}\int_{-\infty}^{+\infty}\int_{-\infty}^{+\infty} \tilde{A}_z(k_x,k_y,Z) e^{-j(k_x x + k_y y)} dk_x dk_y y \tag{4.3}$$

$$\nabla^2 A_z + k^2 A_z = \frac{1}{(2\pi)^2}\int_{-\infty}^{+\infty}\int_{-\infty}^{+\infty} (-k_x^2 - k_y^2 + \frac{\partial}{\partial z^2} + k^2)\tilde{A}_z(k_x,k_y,Z) e^{-j(k_x x + k_y y)} dk_x dk_y = 0 \tag{4.4}$$

Hence

$$\frac{\partial^2 \tilde{A}_z}{\partial z^2} + (k_x,k_y,Z) e^{-j(k_x x + k_y y)} dk_x dk_y = 0 \tag{4.5}$$

If we define

$$k_z \equiv \sqrt{(k_0^2 - k_x^2 - k_y^2)} \tag{4.6}$$

Correct choice would be

$$k_z = \begin{cases} \sqrt{k_0^2 - k_x^2 - k_y^2}, & k_x^2 + k_y^2 < k_0^2 \\ -j\sqrt{k_0^2 - k_x^2 - k_y^2}, & k_x^2 + k_y^2 < k_0^2 \end{cases} \tag{4.7}$$

Then we have

$$\frac{\partial^2 \tilde{A}_z}{\partial z^2} = k_z^2 \tilde{A}_z = 0 \tag{4.8}$$

Solution,

$$\tilde{A}_z(k_x, k_y, z) = \tilde{A}_z(k_x, k_y, 0)e^{-jk_z z} \tag{4.9}$$

Similarly,

$$\tilde{F}_z(k_x, k_y, z) = \tilde{F}_z(k_x, k_y, 0)e^{-jk_z z} \tag{4.10}$$

Hence,

$$A_z(x, y, z) = \frac{1}{(2\pi)^2} \int_{-\infty}^{+\infty} \int_{-\infty}^{+\infty} \tilde{A}_z(x, y, 0)e^{-j(k_x x + k_y y + k_z z)} dk_x dk_y \tag{4.11}$$

$$F_z(x, y, z) = \frac{1}{(2\pi)^2} \int_{-\infty}^{+\infty} \int_{-\infty}^{+\infty} \tilde{F}_z(x, y, 0)e^{-j(k_x x + k_y y + k_z z)} dk_x dk_y \tag{4.12}$$

This a representation of the potential as spectrum of plane waves. For an aperture in x-y plane, the far-fields can be represented as

$$E_\theta = \frac{jke^{-jkr}}{4\pi r}[f_x \cos\phi + f_y \sin\phi + \eta \cos\theta(-g_x \sin\phi + g_y \cos\phi)] \tag{4.13a}$$

$$E_\phi = \frac{jke^{-jkr}}{4\pi r}[(f_x \sin\phi - f_y \cos\phi)\cos\theta + \eta \cos\theta(-g_x \sin\phi + g_y \cos\phi)] \tag{4.13b}$$

where η is the impedance in free space and f and g have been expanded in terms of their x and y components.

4.5 Huygens Sources

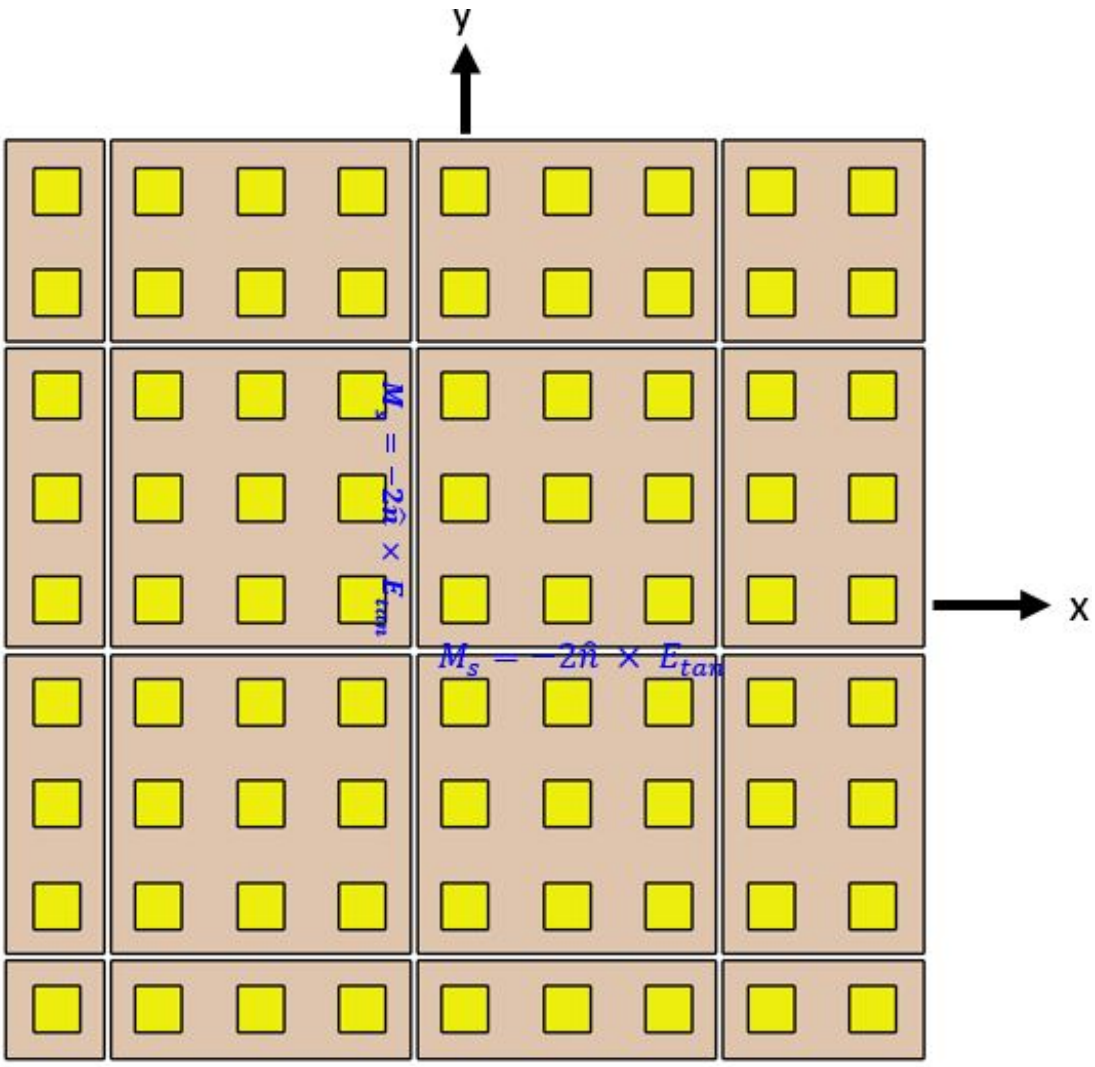

Figure 4.15: Equivalent gap current model on ground plane.

It is very important to understand that antenna radiate from currents. For the problem described here in Figure 4.15, we need to first calculate the current in the gap. Using the computational electromagnetic methods, one can calculate currents on a boundary surface by using the equivalence theorem with the incident fields, and calculate the far-field radiation pattern from these boundary currents. In general, we assume a current

distribution on the antenna or, equivalently, a distribution of fields on an aperture. The fields on the aperture can be reduced to a current distribution. We need to calculate the magnetic current distribution in this gap model depicted in Figure 4.15. Magnetic current are fictitious, but they enable the radiation problem to be solved. This kind of problem stated in Figure 4.15 can be solved by simply analyzing the aperture in periodic environment.

We replace the incident fields in the aperture with a combination of equivalent electric and magnetic currents. We calculate radiation as a superposition of each source by using the vector potentials. Oftentimes, we assume that the incident field is a propagating free-space wave whose electric and magnetic fields are proportional to one another. This gives us the Huygens source approximation and allows the use of integrals over the electric field in the aperture. Each point in the aperture is considered to be a source of radiation.

The Huygens source approximation is based on the assumption that the magnetic and electric fields are related in a plane wave in the aperture as [23]

$$\eta g_y = f_x \qquad and \qquad -\eta g_x = f_y \tag{4.14a}$$

$$\eta H_y = E_x \qquad and \qquad -\eta H_x = E_y \tag{4.14b}$$

with this approximation the far field becomes

$$E_\theta = \frac{jke^{-jkr}}{4\pi r}(1+\cos\theta)(f_x\cos\phi + f_y\sin\phi) \tag{4.15a}$$

$$E_\phi = \frac{jke^{-jkr}}{4\pi r}(1+\cos\theta)(f_x\sin\phi - f_y\cos\phi) \tag{4.15b}$$

The two-dimensional vector Fourier transform $\boldsymbol{f} = (f_x, f_y)$ of the aperture electric field in the x-y plane determines the far-field components. We derive the radiated components

by projecting (vector scalar product) this field onto the vectors $\frac{\hat{\theta}}{cos\theta}$ and $\hat{\phi}$. The transformed $\boldsymbol{f}$ expands the field in k-space. This normalizes the pattern and removes the direct dependence on the aperture length.

We separate out all but $\boldsymbol{f}$ when we consider aperture distributions. We drop the terms for the radiation from a point source and the pattern of a Huygens point source and limit our discussions to Huygens sources and far fields. General aperture fields require equation 4.13, and for any region other than the far-field, additional phase terms are needed in the transforms.

4.6 Further Simulation Results

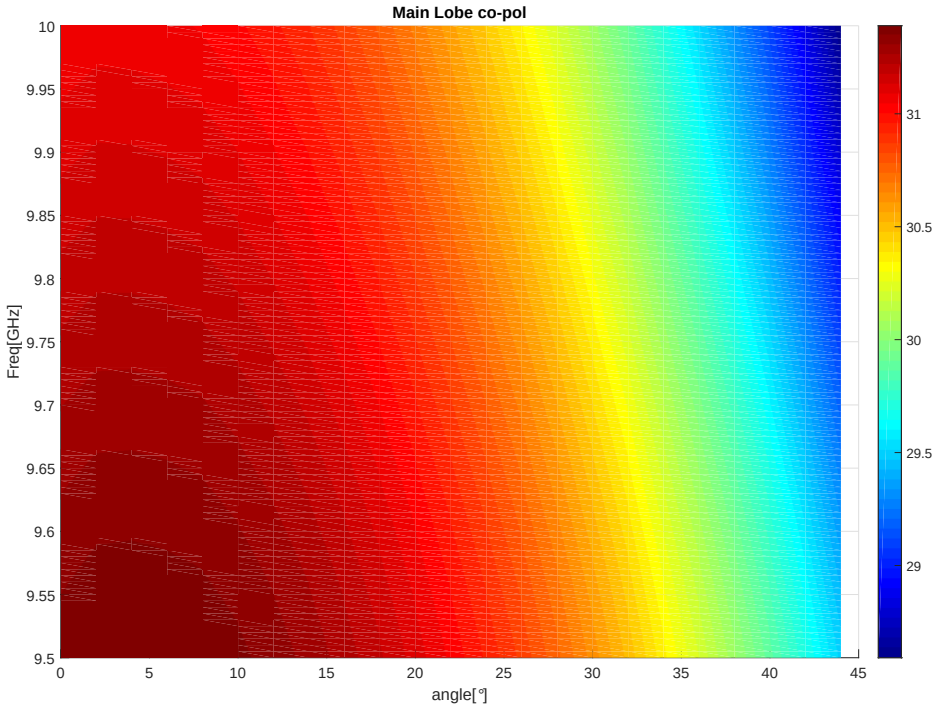

Figure 4.16: Without gap main lobe co-pol.

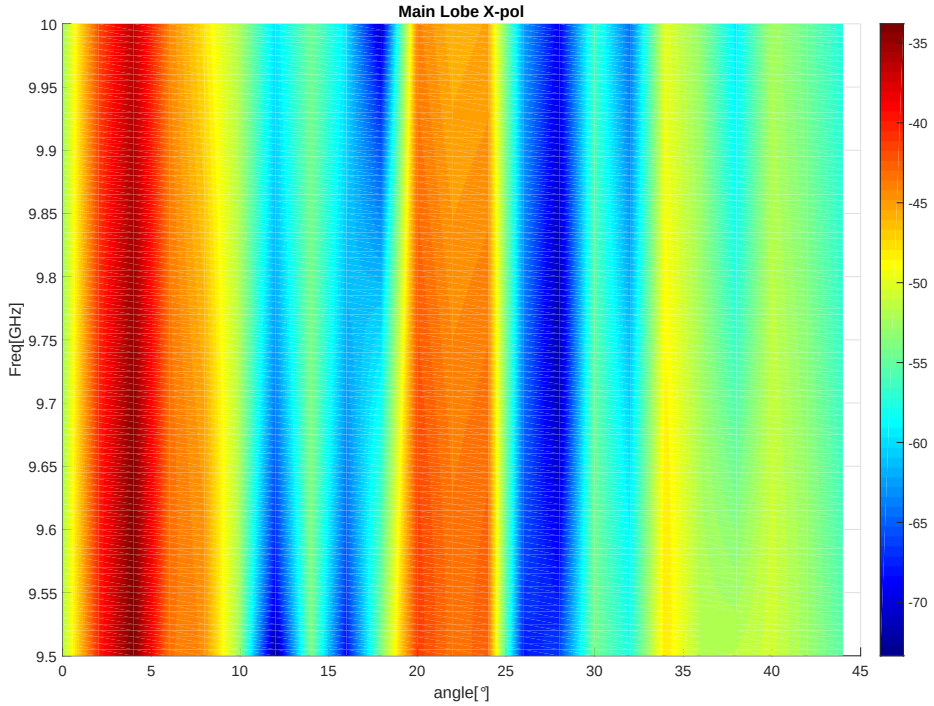

Figure 4.17: Without gap main lobe cross-pol.

The goal of this section is to accurately capture and analyze the grating lobes effects including mutual and surface wave effects for any given scan angles of planar phased arrays with rectangular lattice structures. To perform this investigation, we expanded our study from 0° scanning angle to 44° with 2° angular resolution. We studied for both cases, without gap and with a 1 mm gap. The co-pol and cross-pol of main beam for without gap case are plotted in Figure 4.16 and Figure 4.17. Figure 4.18 and Figure 4.19 depicted the co-pol and cross-pol of main beam for the 1 mm gap case. As expected, the patterns distorted for the 1 mm gap case at a scan angle near 20° and the amplitude of the cross-pol increased. This cross-pol rise is happened may be the gap current radiation.

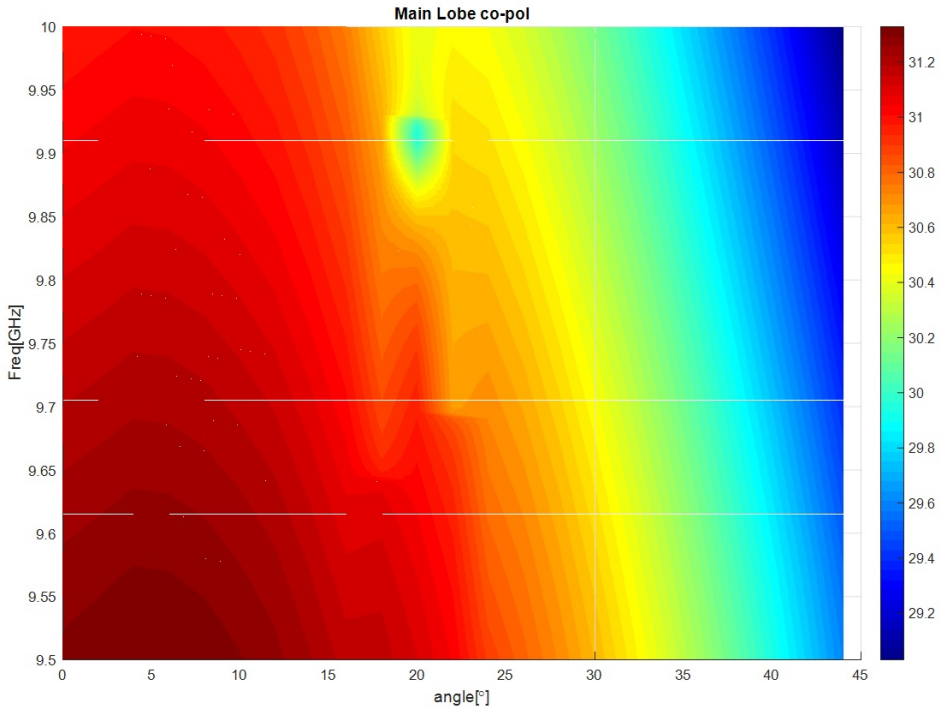

Figure 4.18: With a 1 mm gap main lobe co-pol.

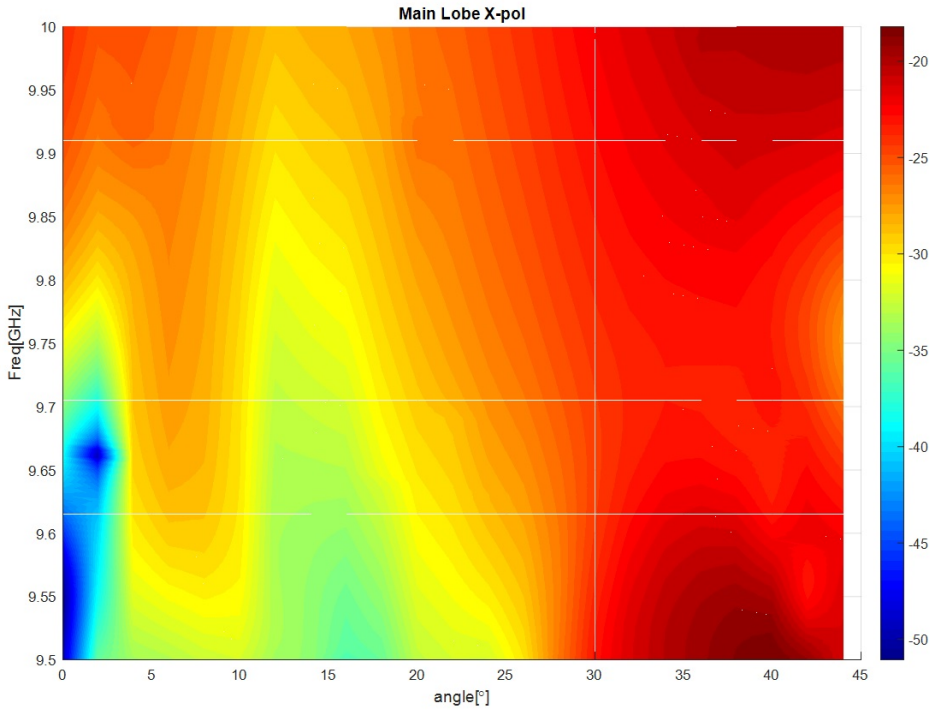

Figure 4.19: With a 1 mm gap main lobe cross-pol.

4.7 Gap Current Radiation

To investigate more, the present section focuses on how gap current can be captured due to gaps in the sub-arrays, how this gap current radiates and affects the grating lobes, sidelobes, cross-polarization levels, and the radiation patterns is discussed in order to acquire fundamental knowledge and undertake theoretical/mechanical treatments to the array level to predict the overall array performance. These studies were performed with the combination of Floquet modal unit cell analysis results and exporting these results into a MATLAB program, where spectral domain analysis technique, discussed in earlier sections, was used. The unit cell discussed herein, as shown in Figure 4.1, has a total of nine wave ports and a 1 mm gap in-between the array. After a successful full-wave Floquet modal simulation in the HFSS, the surface currents and near-field data are exported with a constant resolution in a uniform grid. Initially, the center element of the array is excited, and results are exported under master/slave conditions. Antennas in the array are arranged along $\phi = 90°$, making it as an E-plane. The results shown here are only for the scan angle $(\phi_s, \theta_s) = (90°, 30°)$. The gap currents are depicted in Figure 4.20.

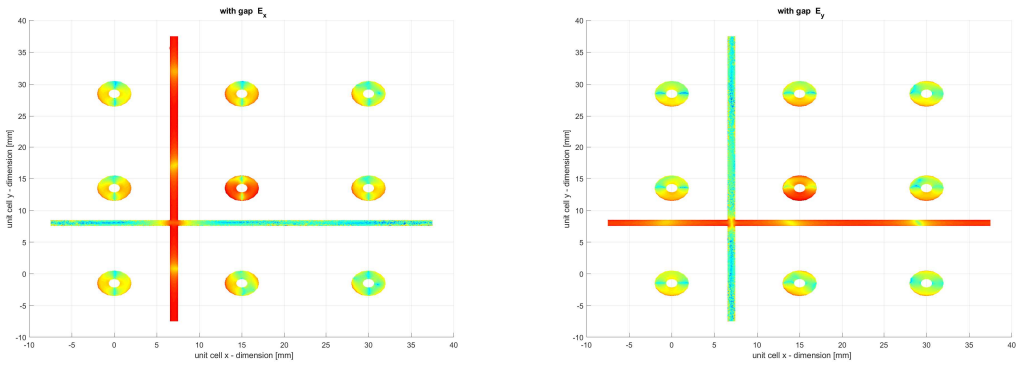

(a) E_x field [with gap]

(b) E_y field [with gap]

Figure 4.20: Electric fields in the ground plane while exciting center element [E-plane].

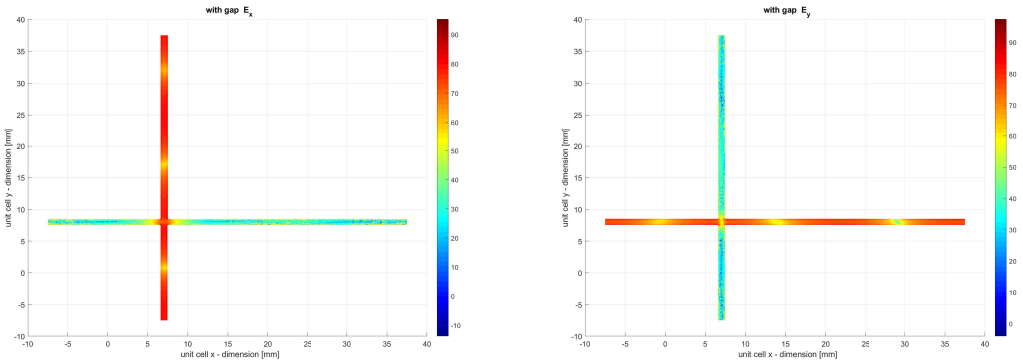

(a) E_x field [with gap] (b) E_y field [with gap]

Figure 4.21: Gap currents only [E-plane].

The near-field data for gap along x- and y-directions is visible in the graphs due to excitation of the center element of the array. The fields for the ports are also apparent in the graphs. It is evident that by eliminating the ports' near-field current contribution, one can easily get the gaps' current only as illustrated in Figure 4.21. This graph is showing only the gaps' contribution.

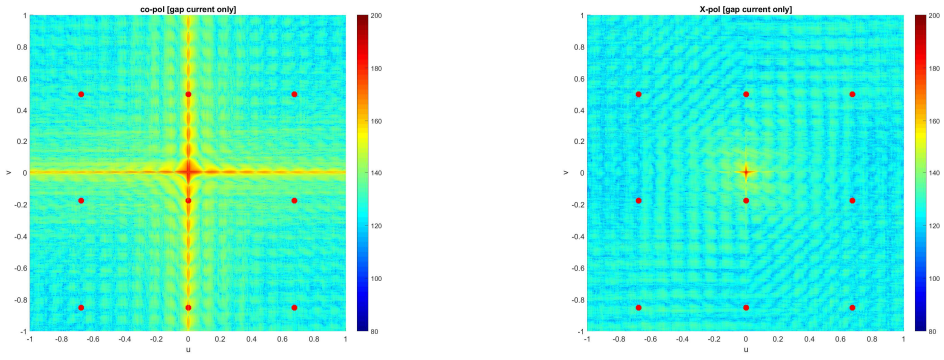

(a) Co-pol [with gap] (b) Cross-pol [with gap]

Figure 4.22: Radiated electric fields due to gap currents only [E-plane].

If we consider this gap current as an infinitely long magnetic current source, using spectral domain method and invoking Huygen's equivalent principal, the radiated fields for the gap itself can be calculated. The radiated fields solely for the gap current radiation are plotted in Figure 4.22. By employing standard mathematical formulation, the radiated fields are converted to Ludwig-II, and depicted in Figure 4.23. The radiation patterns due to gap current are even worse when converted to Ludwig-II. The red dots on the graphs are representing the grating lobe locations.

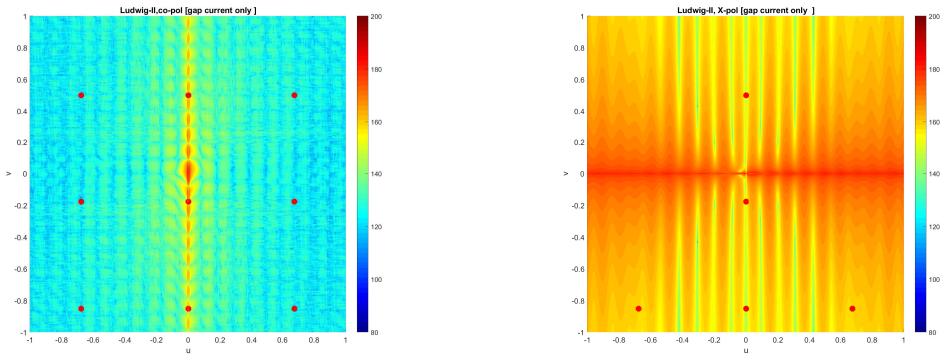

(a) Co-pol [with gap]

(b) Cross-pol [with gap]

Figure 4.23: Radiated electric fields due to gap currents in Ludwig-II [E-plane].

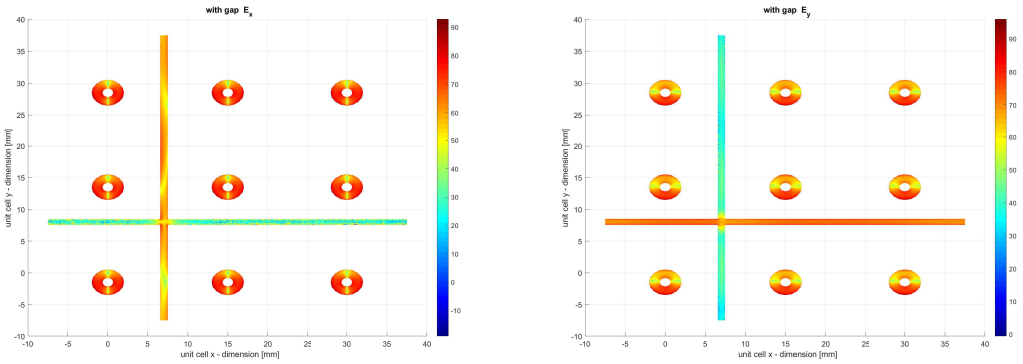

(a) E_x field [with gap] (b) E_y field [with gap]

Figure 4.24: Electric fields in the ground plane while exciting all elements [E-plane].

In the previous configuration, only the center element of the array was excited. Now, all nine elements are excited and all nine elements contribution to the gap and resulting radiating patterns are studied. The scan angle for this study is chosen to be $(\phi_s, \theta_s) = (90°, 30°)$. Similar approaches are applied to perform this study as well. The contribution from all nine elements are presented in Figure 4.24. As is observed, the ports' near-field data is visible in the graphs.

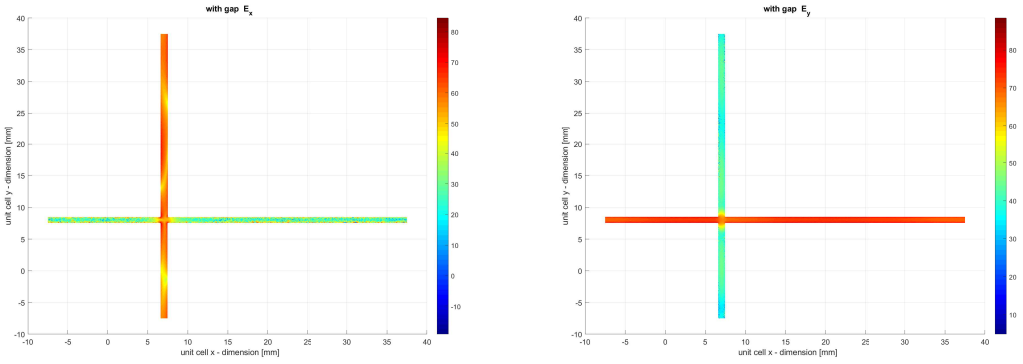

(a) E_x field [with gap] (b) E_y field [with gap]

Figure 4.25: Gap currents only while exciting all elements [E-plane].

The concentration of this study is solely based on the gaps' contribution. Therefore, the ports' data are eliminated and resulting gaps' fields are plotted in Figure 4.25. As can be seen in the graphs, there is only gap fields are available.

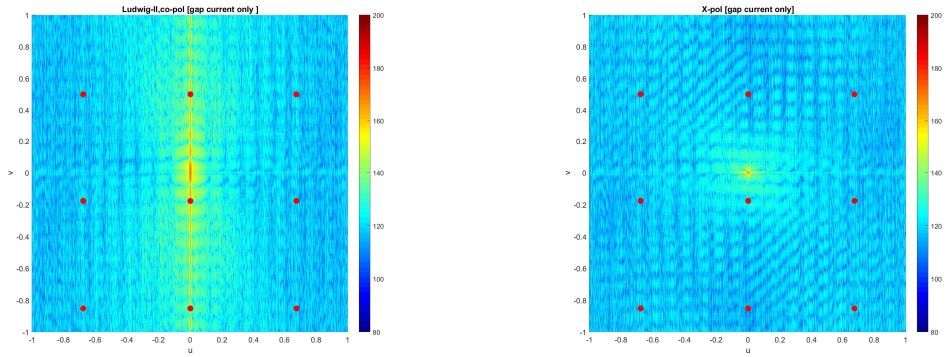

(a) Co-pol [with gap] (b) Cross-pol [with gap]

Figure 4.26: Radiated electric fields while exciting all elements and due to gap currents only [E-plane].

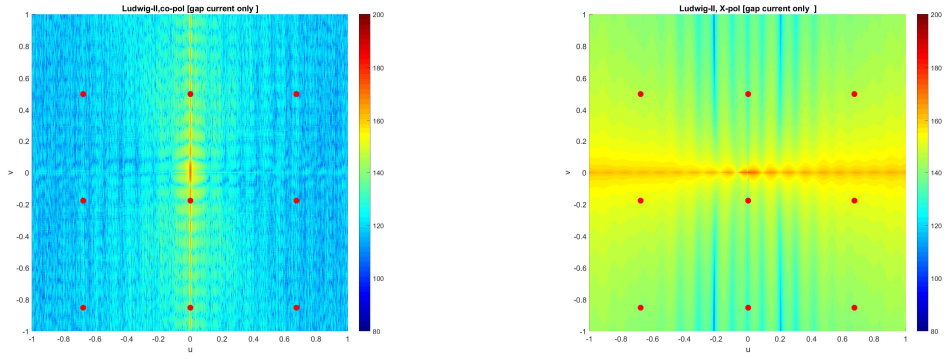

(a) Co-pol [with gap] (b) Cross-pol [with gap]

Figure 4.27: Radiated electric fields while exciting all elements and due to gap currents in Ludwig-II [E-plane].

The radiated far-fields due to the gap current are illustrated in Figure 4.26. The radiated fields are converted to Ludwig-II. Figure 4.27 shows the radiated fields for Ludwig-II.

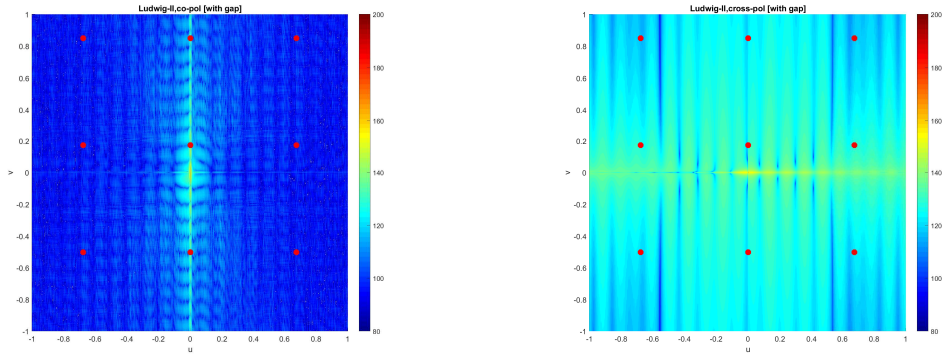

(a) Co-pol $(\phi_s, \theta_s) = (90°, 10°)$. (b) Cross-pol $(\phi_s, \theta_s) = (90°, 10°)$.

Figure 4.28: Radiated electric fields due to gap currents in Ludwig-II [E-plane].

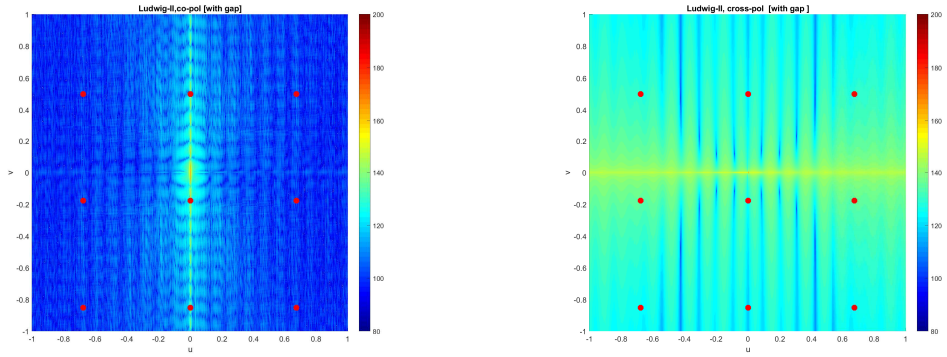

(a) Co-pol $[(\phi_s, \theta_s) = (90°, 30°)]$. (b) Cross-pol$[(\phi_s, \theta_s) = (90°, 30°)]$.

Figure 4.29: Radiated electric fields due to gap currents in Ludwig-II [E-plane].

After exciting all nine elements in the array and their contribution to the gap currents are added together, the results are averaged to get the final radiated fields. The radiated fields for scan angle $(\phi_s, \theta_s) = (90°, 10°)$ after converting to Ludwig-II are shown in

Figure 4.28. Similarly, for scan angle $(\phi_s, \theta_s) = (90°, 30°)$, the contribution of radiated fields in Ludwig-II is illustrated in Figure 4.29. The study is performed for various scan angles and different settings for port excitation, for instance, exciting the center element only and/or all nine elements. From all the graphs shown above, it is evident that, even for a 1 mm gap truncation in the sub-array, the gap current radiates and it contributes to the both co-pol and cross-pol patterns. There is no gap exist under the assumption of infinitely long ground plane and thereby no gap current contribution to the radiation patterns. Finally, it can be concluded truncation of gap in the ground plane or perturbation of currents due to gaps affects the cross-pol, which may lead to cross-pol rise in the patterns.

4.8 Conclusions

A large phased array that requires thousands of elements is typically built by adjoining several sub-arrays next to each other. Mechanical gaps (or other perturbations) are therefore likely at the sub-array seams. These gaps disrupt the natural current flow in between sub-arrays, leading to the potential for low-level grating lobe effects. This study has attempted to simulate and measure these effects carefully in a near-field chamber using a reasonably large array with an X-band, with relatively large (1 mm) gaps between sub-arrays of 3×3 elements. It was found that the measurements qualitatively follow the simulated results in most cases, but that mechanical (and thus electrical) variability in the fabrication of this particular array may have limited the overall accuracy of the measurements. Nevertheless, the measurements show that with suitable disruption to the natural current flow (particularly along the E-plane for these microstrip patch antennas), one does observe measurable increases in grating lobes, even based on measurement of a

subset of the sub-arrays. The Floquet-based method may therefore be used as a good approximation for a worst-case scenario where all gap-based perturbation effects are identical on each sub-array.

Effects of ground plane/dielectric truncation is obvious. When the dielectric coated ground plane is of infinite extent, all the antenna elements see the same mutual coupling environment. When the ground plane has a sharp discontinuity like the case of the finite sub-array analyzed here, the surface waves will be diffracted. If one can consider this truncation in the unit cell analysis as infinitely long magnetic current source, the effects of truncation on the radiation patterns, grating lobes, and cross-pol levels can be analyzed accurately by incorporating all mutual coupling and surface wave effects using the mathematical framework described above for any given scan angles. A full wave analysis of the problem using the spectral domain approach is also presented to verify the validity of the Floquet framework invoked for this analysis. Theoretical and experimental investigations on any scan angles were also conducted. Both mathematical frameworks reveal that the truncation in the ground plane even as small as 1 mm alters the grating and cross-pol levels significantly. This rigorous effort can be used for system-level planning to inform a mechanical solution to the electrical connection between sub-array for any future phased array radar applications.

5

Floquet Analysis of Planar EBG structure for Surface Wave Suppression

In the electromagnetic environment, the inherent behavior in the interface of two different materials always generates surface waves. This also includes, for instance, interface between free space and the dielectric material. These surface waves propagate along the interface and decay slowly or attenuate with the distance from the interface. During these path propagations the surface waves get incident to one interface and reflected back to the other interface, and when they reach to the edges they get diffracted and radiate readily into surrounding space as leaky waves. These undesirable features are depicted in Figure 5.1. These waves are incident on the ground plane, for instance, at an elevation angle θ, get reflected from there, and meet the dielectric-air interface, which also reflects them. Following this waggling path, they finally reach the boundaries of the substrate where they are reflected back and diffracted by the edges of the substrate [1].

These surface waves can be classified into two categories: transverse electric (TE) or transverse magnetic (TM) surface waves. They are the TE and TM modes of the substrates. These modes are characterized as the wave attenuating in the transverse direction (normal to the antenna plane).

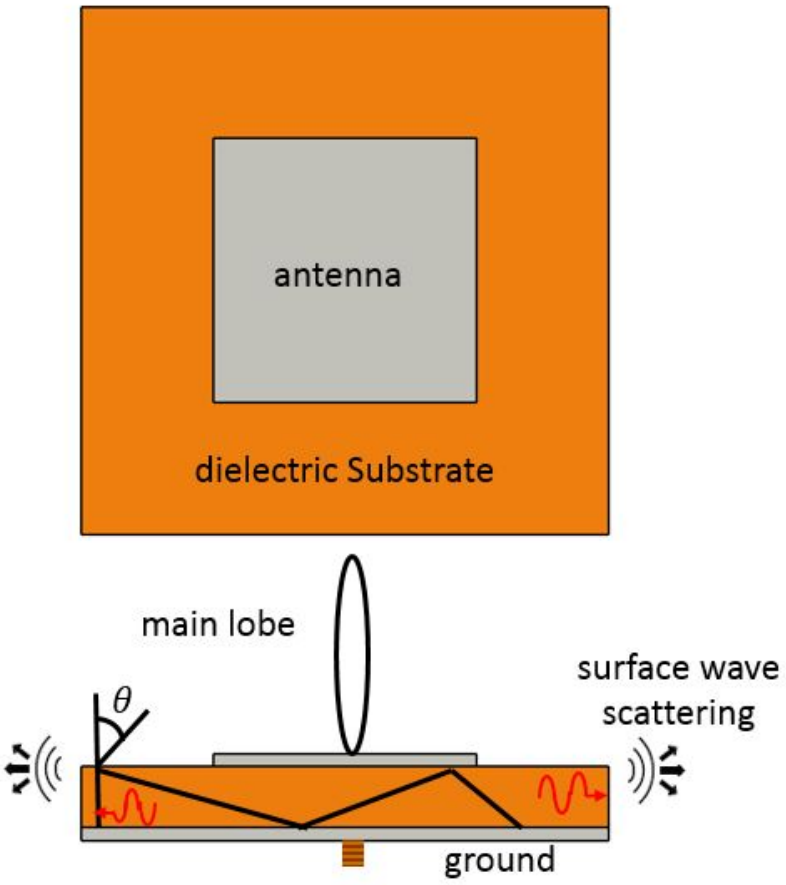

Figure 5.1: Propagation of surface waves in the substrate [1].

Surface wave propagation is a very serious problem in the phased array community. Surface wave radiation increases cross-polarization levels, limits beam scanning capabilities and creates scan blindness, reduces antenna efficiency and gain, and increases end-fire radiation. Therefore, it is very important to explore these surface waves and their characteristics and propose a way to suppress these surface waves. Electromagnetic bandgap (EBG) structures offer unique solution, for they effectively suppress surface waves for a variety of frequencies and a wide range of applications [24]. EBGs usually consist of metallic patches of different shapes located at the surface of grounded dielectric slab and each element is connected to the ground plane through vias. The metallic patches could be

Figure 5.2: Lumped LC model for EBG analysis [2].

different shapes like a square, hexagon, or other shapes. In general, the height of the substrate is less than a tenth of a wavelength $h < \lambda/10$ [25]. According to [25], the vias plays a very important role in suppressing the surface waves. Numerous studies have been carried out over the years to suppress the surface waves using vias. The main idea, in short, is that using a high impedance surface, the antenna is placed very near to the ground plane and electromagnetic bandgap behavior suppresses propagation of surface waves, which reduces radiation from the edges and thereby maintains a very directive beam [2, 24, 25].

Even though various methods have been implemented to analyze the EBG structures, the simplest method is the lumped element model. Other techniques are: (a). periodic transmission line method and (b). full wave numerical methods. Figure 5.2 represents the equivalent lumped element model of the EBG structure and that describes EBG as an LC resonant circuit [26]. The resonance frequency is given by the following equation

$$\omega_0 = 1/\sqrt{LC} \tag{5.1}$$

It is evident from the equation that, if we increase the capacitance, resonance frequency can be reduced. To the author's knowledge, no publications to date have analyzed the fundamental limits of these high impedance surfaces or provided clear guidelines to design these high impedance surfaces including multilayer circuits. Analysis of multilayer structure and vias is also rare. Some others suggest that TM wave suppression is relatively easy

compared to the TE waves [27]. Hence, it is very important to analyze EBG geometry for multilayer structures for phased array applications and suppress the surface waves.

5.1 Benefits of Reducing Surface Wave Suppression

Reducing surface wave excitation from printed planar antennas can be beneficial for various reasons. First, the radiation efficiency will increase due to reduced surface waves excitation. Second, due to decreased surface waves, the diffraction from the edges will also decreased, leading to decreased back radiation and interference with the main pattern in the forward region. Also, reduced surface wave excitation usually results in reduced coupling between adjacent antenna elements [28].

EBG substrates consist periodic structures and have forbidden frequency bands, within which no surface waves can propagate. Care must be taken, however, to also ensure that leaky waves are not supported by the periodic substrate, which can also result in undesirable effects [29]. Antennas based on reduced surface waves can also eliminate the surface waves [28].

The wire medium supports three different families of plane wave solutions: transverse electromagnetic (TEM) modes, transverse magnetic (TM) modes, and transverse electric (TE) modes. The dispersion characteristics of these modes are [30]

$$\beta_h = \pm k_z \quad (TEMmode) \tag{5.2a}$$

$$\beta_h^2 = k^2 \quad (TEmode) \tag{5.2b}$$

$$\beta_h^2 = \beta_p^2 + k^2 \quad (TMmode) \tag{5.2c}$$

The mushroom type EBG structure has many benefits: 1) it provides a compact high-impedance boundary and an in-phase reflection characteristic and 2) it can suppress the propagation of guided modes. These properties are useful in enhancing the radiation

properties of low-profile antennas, e.g., to improve the return loss over a relatively wide bandwidth and reduce the mutual coupling in printed antenna arrays sharing the same ground plan.

5.2 Scan Blindness and its Phenomena

The scan range of the printed phased arrays is limited by the phenomenon known as scan blindness, which is induced due to coherent coupling between the substrate waves and the array's space harmonic fields. Due to strong excitation of substrate waves and coupling of desired radiating energy to these unwanted substrate waves, near a scan blindness angle, a phased array fails to function as a radiator or receiver.

Scan blindness occurs as phase matching is satisfied between the substrate waves and array's Floquet modes. This condition can be shown as [31]

$$\beta_{sub}^2 = (\frac{2\pi p}{d_x} + k_0 \sin\theta \cos\phi)^2 + (\frac{2\pi q}{d_y} + k_0 \sin\theta \sin\phi)^2 \tag{5.3}$$

where β_{sub} is the substrate wave phase constant, where it can be β_{sw} or β_{tw}, depending on the mode type under consideration, and the right side represents phase constant of the projected array mode on the structure's surface. In most practical cases scan blindness is due to coupling between a surface wave mode and the $(\mp 1, 0)$ Floquet modes. However, we can also observe from equation 5.3 that the scan blindness, due to the $(0, 0)$ Floquet mode or main beam, is possible if the array excites leaky wave modes, whose phase constant β_{sw} is smaller than that of free space k_0.

Fast periodic leaky modes may exist within a surface wave bandgap zone. These leaky modes may result in more energy loss and crosstalk than the surface wave modes and should be taken into account in circuit design. Leaky modes (complex wavenumbers) may exist within the surface wave bandgap. In order to utilize the surface wave bandgap for loss

reduction, it is necessary to also eliminate the leaky modes within the bandgap, creating a complete mode bandgap [29]. The eigenvalues (propagation wavenumbers) are obtained from the roots of this equation for a given direction in the phase plane (i.e., for a given ratio of or, equivalently, a given angle). When the propagation wavenumber is purely real (for a lossless structure), the corresponding mode is a bound mode. When the wavenumber is a complex value, the mode may be either an attenuating slow wave (an evanescent surface wave mode in the bandgap) or a radiating leaky mode. To calculate the leaky modes, we need attenuation constant α. In the periodic case, if there are several space harmonics, the incident beam may strongly couple to a leaky mode of the structure whenever it is phase matched to any of these space harmonics. A guided mode with phase constant $|\beta| < k_0$, supported by an open wave guiding structure, is a leaky wave that radiates energy into free space as it travels along the structure. In other words, the leaky mode can couple to the radiation modes of free space, namely, outgoing plane waves. However, recent theoretical and experimental findings have shown that, under specific conditions, a fast wave traveling along an open structure can avoid radiation and, instead, it can behave as a purely bound mode without coupling to propagating waves in the background [32].

Similar to mushroom EBG structures, another high impedance surface named unipolar compact EBGs (UC-EBG) is constructed by interconnecting unit cells on the top layer to realize a high-impedance surface with good stopband characteristics at the desired frequency range [33–36]. For a variety of microwave applications, UC-EBG's are very attractive and easier to fabricate compared to mushroom EBGs, as they don't have vias. However, to design UC-EBG's at certain desired frequencies, the compactness became an issue as their periodicity should be a half wave-length at their center frequency [37].

5.3 Multilayer EBG Surface for Antenna Applications

Our main focus for this study is to suppress surface waves for weather applications. Most of the weather radar works on S-band. For simplicity we chose frequency at 3.415 GHz. We have chosen a 50.8 mm $\times$ 50.8 mm unit cell. Due to its larger wavelength and vias in the mushroom, it also needs significant memory constraint to simulate the whole structure in the full wave simulator with proper convergence.

Within the 50.8 mm$\times$ 50.8 mm dimension, we can fit as many mushroom EBG unit cells as we want. Many mushroom EBGs require more memory and time to solve the whole structure. It is important to remember that our substrates are all lossy. However, due to memory and time constraint to use EBG as an antenna's ground plane, we later switched to a 4 $\times$ 4 mushroom EBG unit cell to cover the whole 50.8 mm$\times$ 50.8 mm dimension. That is why our EBG mushroom cell is 12.7 mm, as shown in Figure 5.4.

5.3.1 Dipole Antennas on EBG Surface

In the frequency range where the surface impedance is very high, the tangential magnetic field is small, even with a large electric field along the surface. Such a structure is sometimes described as an artificial magnetic conductor. Because of this unusual boundary condition, the high impedance surface can function as a new type of ground plane for low-profile antennas. The image currents in the ground plane are in-phase with the antenna current, rather than out-of-phase, allowing radiating elements to lie directly adjacent to the surface, while still radiating efficiently. For example, a half-wave dipole lying flat against a high-impedance ground plane is not shorted as it would be on an ordinary metal sheet. For simplicity, we choose dipole antenna length to be $\lambda/2$ as its characteristics are well known.

It is well-known that input impedance for a $\lambda/2$ dipole is $73 + j42.5\ \Omega$ [25]. The resonance condition for any kind of antenna is considered as the reactance part needs to be zero. Therefore, to make the imaginary part equal to zero, the antenna length is reduced until the input impedance becomes real. While the antenna gets excited there is some fringing effect. So, the antenna's physical dimension is not exactly $\lambda/2$, but slightly smaller than the effective length. Usually $\lambda/2$ is the effective length of the antenna.

To design dipole antenna usually this equation can be followed

$$l + d = 0.48\lambda \tag{5.4}$$

where d is the diameter of the wire, and l is the length of the wire. Ideally, $d < \lambda/10$. In such case real input impedance should be $\leqslant 68\ \Omega$. The diameter of the wire antenna can be transformed to the width of the antenna using Hellen's transformation as [38]

$$\text{width of dipole planar antenna } (W) = 4r$$

where r is radius of the wire. In practice, width usually helps to increase the bandwidth of the antenna.

It has been studied that a straight-wire dipole can be located parallel and in very close proximity to the ground plane to achieve $50\ \Omega$ impedance with more bandwidth [39]. Also, Yang and Rahmat−Samii [40] matched a dipole antenna over a single layer EBG surface with $50\ \Omega$ impedance. They concluded that due to strong mutual coupling between the image current and dipole currents, due to their close proximity, the impedance of the dipole gets changed for the PMC ground plane. In their study [40], it was indicated that surface wave bandgap cannot guarantee the effective radiation of a low-profile wire antenna as a complicated interaction occurs between the wire antenna and the EBG surface. They never explained what this complicated interaction is. Our exploration would be to learn about this complicated interaction and its effects on radiation patterns and the surrounding environment.

Yang and Rahmat−Samii [40], in their study of dipole antenna for a single layer mushroom, put the dipole over an EBG top surface as high as $0.02\lambda_{12GHz}$ and varied the dipole distance until maximum isolation found within the frequency band. We extended this study for multilayer circuits for lossy substrates and instead of wire antenna printed planar antenna is used.

5.4 Aperture Coupling

For microstrip planar antenna configuration, aperture coupling is very common for the indirect method of feeding the resonant patch. Aperture-coupled antennas are well known for increasing the impedance bandwidth and theoretically provide zero cross-polarizations in the principal planes [41, 42]. In general, microstrip-fed slot antennas have the advantage of relatively good impedance matching and the capacity for full integration with active or passive components.

For aperture coupling for microstrip antenna, the top substrate contains the radiating element, and the bottom substrate contains the microstrip feed line. The coupling aperture is usually centered under the patch, leading to lower cross-polarization due to symmetry of the configuration. As depicted in Figure 5.3, a small aperture is cut in the ground plane to allow coupling from the open-circuited microstrip feed line to the radiating patch. A microstrip 50 Ω feed line is generally placed in the center of the patch for maximum coupling and symmetric radiation pattern. According to [41], the aperture couple microstrip antenna has several benefits such as:

- The top patch could be fabricated on a thick low dielectric substrate to enhance the BW, and the feed network on the other side of the ground plane could be on a thin high dielectric substrate to reduce radiation losses.

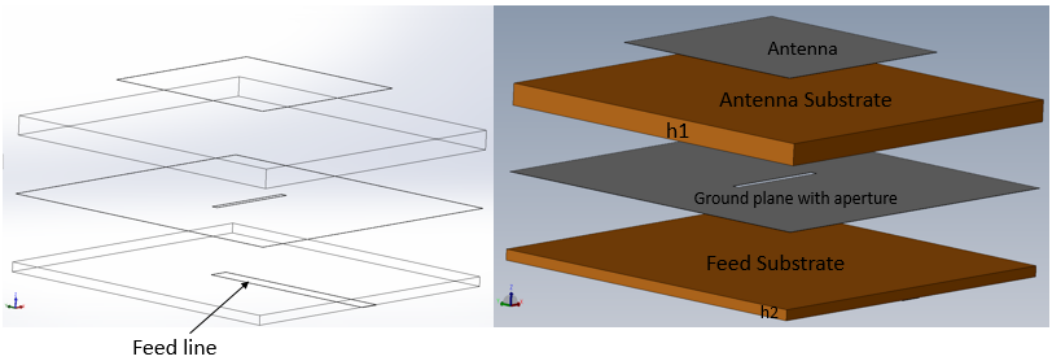

Figure 5.3: Typical aperture coupled microstrip antenna.

- Radiation from the feed network does not interfere with the main radiation pattern, since the ground plane separates the two substrates.
- The excess reactance of the antenna can be compensated for by varying the microstrip feed length of the open-circuited microstrip stub.
- The input impedance is easily controlled by the size, shape, and position of the aperture.

The slot aperture can be either resonant or non-resonant. The resonant slot provides another resonance in addition to the patch resonance, thereby increasing the BW at the expense of an increase in back radiation. As a result, a non-resonant aperture is normally used.

5.5 Reflection Phase Diagram

To effectively suppress the surface waves, a mushroom EBG unit cell is designed, as presented in Figure 5.4. It consists of five parts: two dielectric substrates of different thickness, a metal ground plane is sandwiched in-between the dielectric substrates, periodic metal patches on top of the substrate, and vertical vias connecting the patches

to the ground plane. The patch size is 11.47 mm × 11.47 mm and the ground plane is 12.70 mm × 12.70 mm. The diameter of the via is 2 mm. The dimension of the top substrate is 12.70 mm × 12.70 mm × 4.572 mm, where at the bottom substrate is 12.70 mm × 12.70mm × 1.524 mm.

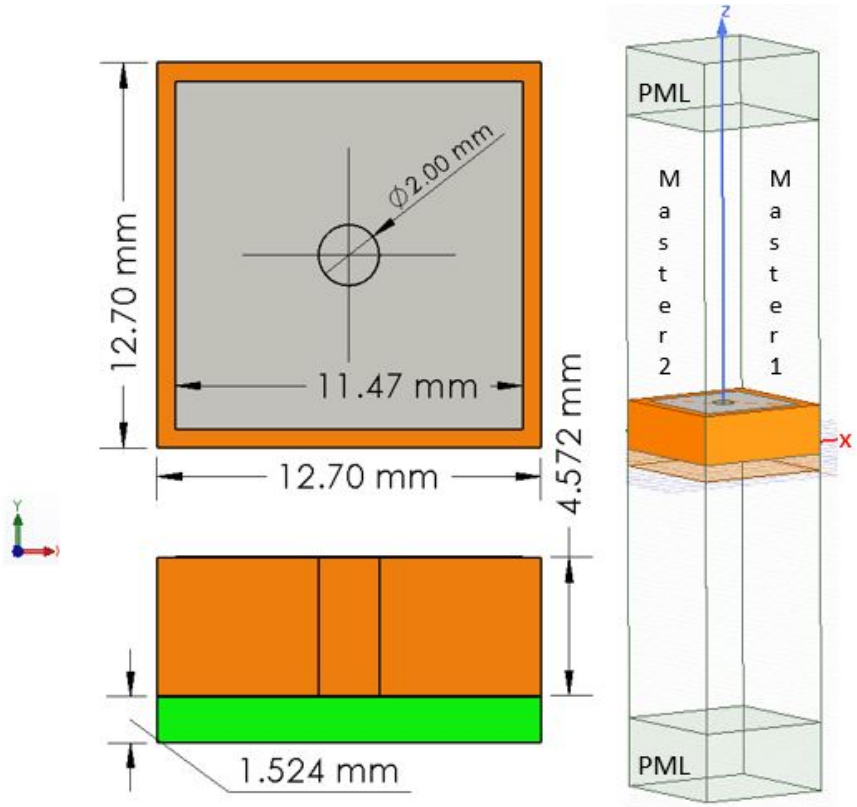

Figure 5.4: EBG unit cell structure.

The performance of the mushroom EBG surface is verified based on the aforementioned geometrical configuration and dimensions. The plane wave normal incidence reflection phase variation of S_{11} of the geometry is shown in Figure 5.5. The full wave Floquet based simulated data shows that the bandwidth of 0.50 GHz ($f_l = 3.27$ GHz and $f_h = 3.77$ GHz) is achieved. At a very low frequency, the reflection phase is +180° and the structure behaves like a smooth metal surface. As frequency increases the reflection phase slopes

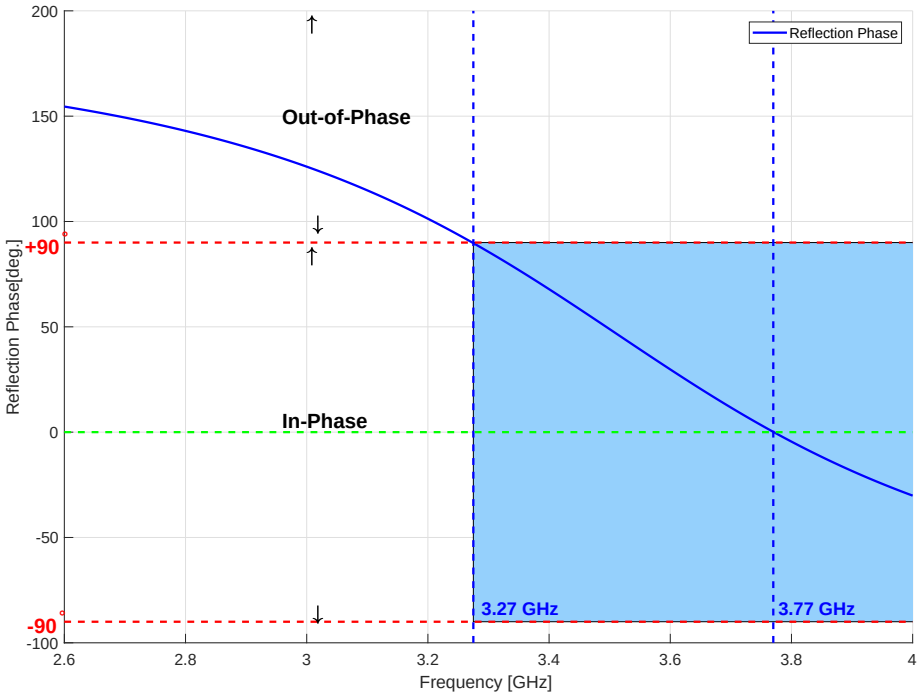

Figure 5.5: Reflection phase diagram of the proposed EBG geometry.

downward and eventually crosses through zero, where it behaves like a magnetic conductor. Above the resonance frequency the phase returns to $-180°$. This diagram is obtained from HFSS, a full wave electromagnetic solver. It is worth mentioning that both CST and HFSS give almost the same reflection phase diagram. The desired band is close to the frequency region where the EBG surface shows a reflection phase in the range of $(0° \pm 90°)$. In this range, antenna can lie on the top of the EBG surface.

5.6 Dispersion Diagram and Surface Wave Bandgap

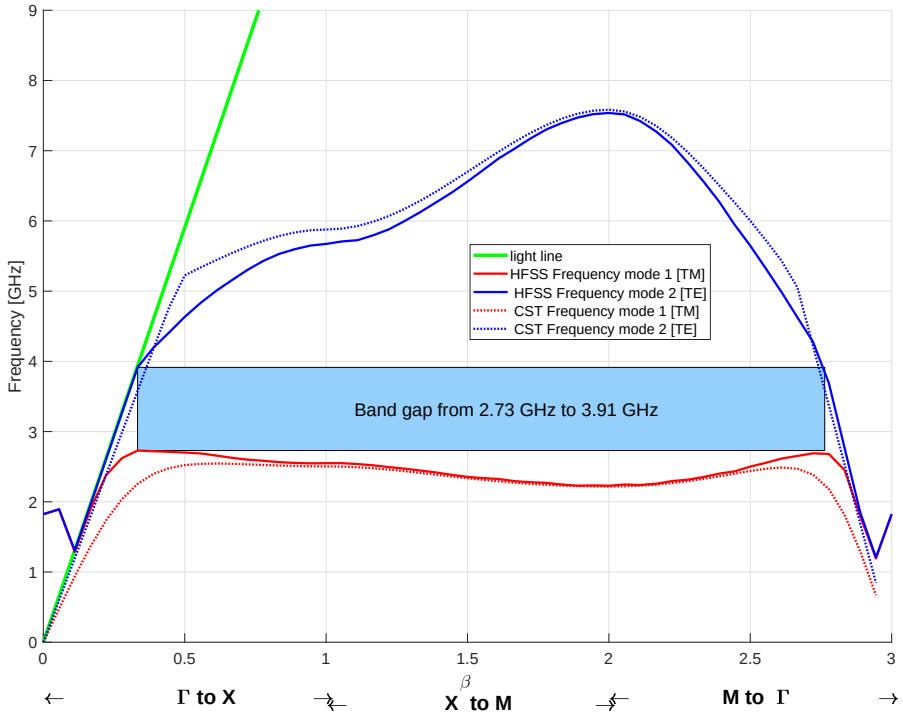

Figure 5.6: Dispersion diagram of the proposed EBG geometry.

A single EBG unit cell is simulated using full wave eigenmode HFSS and CST solver. The Bloch boundary conditions are applied in the unit cell. The dispersion diagram for the geometry described here is shown in Figure 5.6. As can be seen, the surface wave bandgap is approximately between 2.73 GHz and 3.91 GHz. Below resonance the TM surface waves are supported. At low frequencies they lie very near to the light indicated in Figure 5.6 by a green line with a slope equal to the speed of light c. The field extends many wavelengths beyond the surface, as it does on a flat metal sheet. Near the resonant frequency, around 3.415 GHz, the surface waves are tightly bound to the surface and have a very low group velocity. The dispersion curve is bent away from light line at around 3.91 GHz. Above the resonance frequency, the TE waves are supported and the surface is capacitive. The

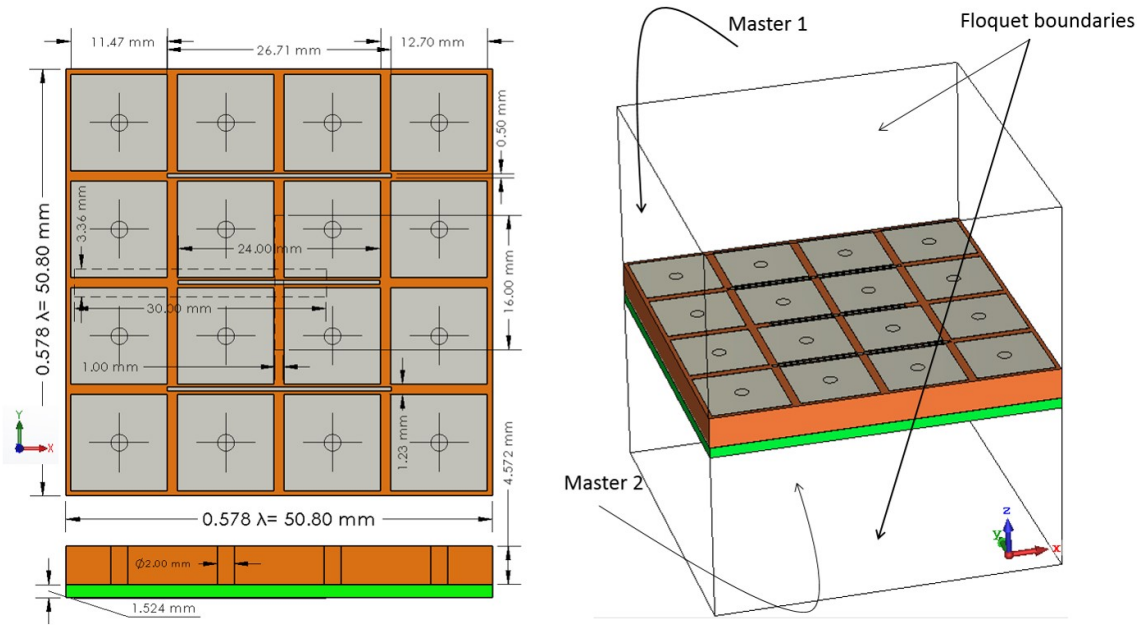

Figure 5.7: Proposed EBG geometry.

lower end of the dispersion curve is close to the light line and the waves are weakly bound to the surface, extending far into the surrounding space. As the frequency is increased, the curve bends away from the light line and the waves are more tightly bound to the surface [24]. The slope of the dispersion curve indicates that the waves feel an effective index of refraction that is greater than unity. This is because a significant portion of the electric field is concentrated in the capacitors.

5.7 Theoretical Design of Mushroom EBG Dipole Antenna

In this study, a mushroom EBG structure for dipole antennas is designed to resonate at 3.415 GHz. Figure 5.7 shows the dimensions of the antenna. The antenna is designed on the substrate R4350B with dielectric constant ϵ_r=3.66. The geometry has two substrates,

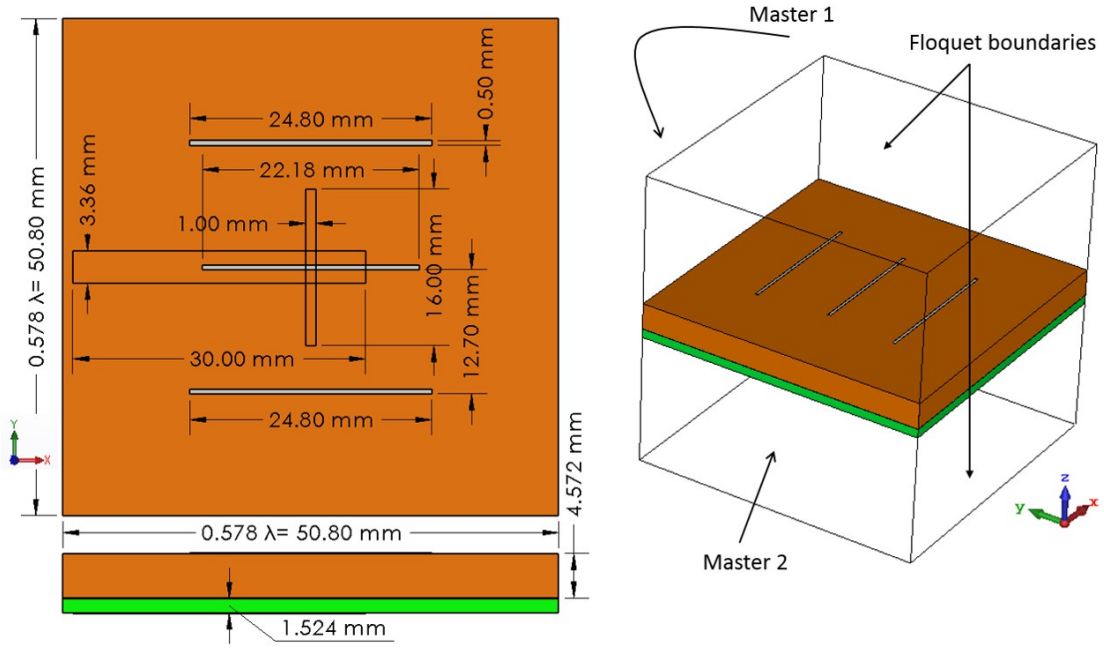

Figure 5.8: Antenna geometry without mushroom.

the top for the antenna and the bottom for the feed. The dimension of the mushroom patch is chosen to be 11.47 mm × 11.47 mm. The via dimension is found 2 mm and the distance between two mushrooms patch is 1.23 mm. The unit cell consists of three parallel dipole antennas. The center one is the driven dipole antenna and the other two are parasitic antennas. Parasitic elements are used to increase the bandwidth of the antennas. The driven antenna dimension is 24 mm × 0.50 mm. The parasitic antenna dimensions are 26.71 mm× 0.50 mm. These dimensions are obtained through parametric studies. The aperture in the ground plane is 16 mm × 1 mm. On the bottom substrate there is a microstrip feed line. This stub length is found to be 5.6 mm × 3.36 mm to match it with 50 Ω.

The geometry is excited under Floquet boundary conditions. It is found that there are 34 Floquet modes required to perfectly simulate the antenna. Therefore, 34 Floquet modes are used on each top and bottom Floquet boundary. The choice of these modes is

based on the frequency, scan angle, and unit cell size to ensure that highest order modes have enough attenuation to the Floquet ports.

To compare the antenna performance, another similar naked version of the antenna is designed. Figure 5.8 shows the geometry of the naked version. Since the antenna needs to resonate at 3.415 GHz, the dimensions for the driven and parasitic elements are changed slightly. These dimensions are found through parametric studies. The driven antenna's dimensions are 22.18 mm $\times$ 0.50 mm. The parasitic antennas' dimensions are 24.80 mm $\times$ 0.50 mm.

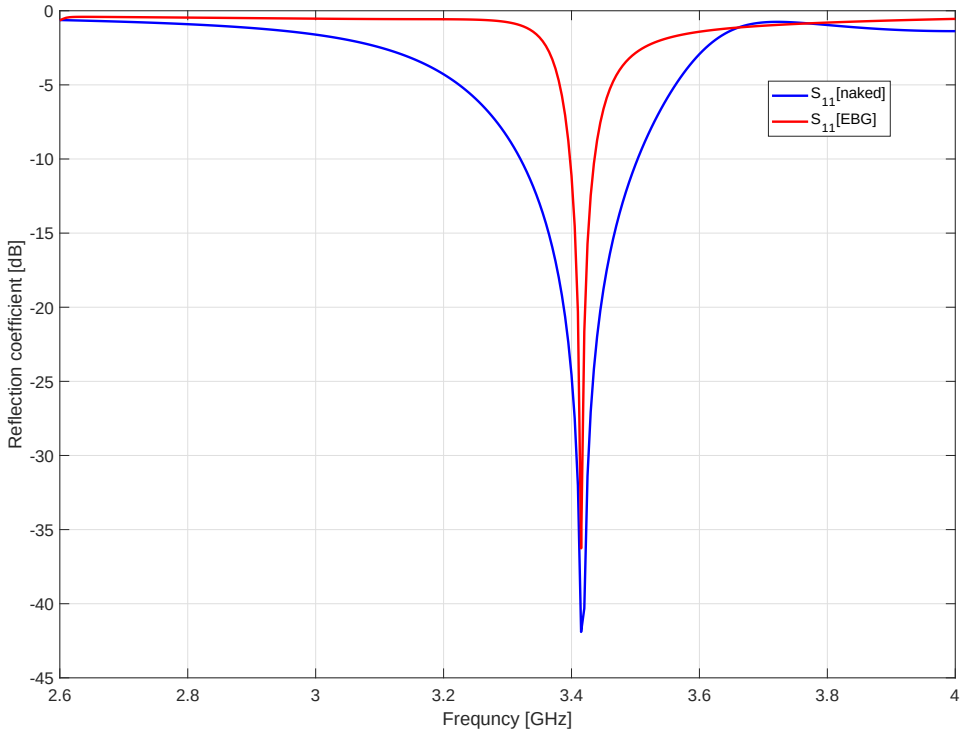

Figure 5.9: Reflection coefficient comparison.

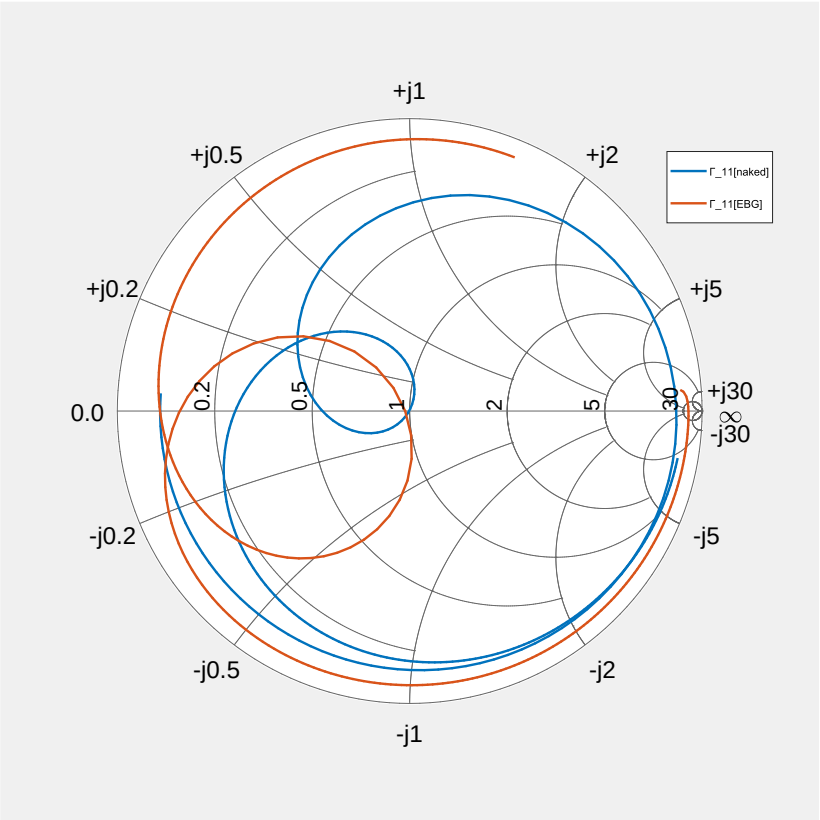

Figure 5.10: Smith charts comparison.

The performance of the antenna is shown in Figure 5.9. Both antennas are resonating at 3.415 GHz. The comparison of the smith charts is shown in Figure 5.10. It is found that both antennas achieved well impedance match at 3.415 GHz. However, a naked version has wider bandwidth compared to the EBG one.

5.8 Scan Performance

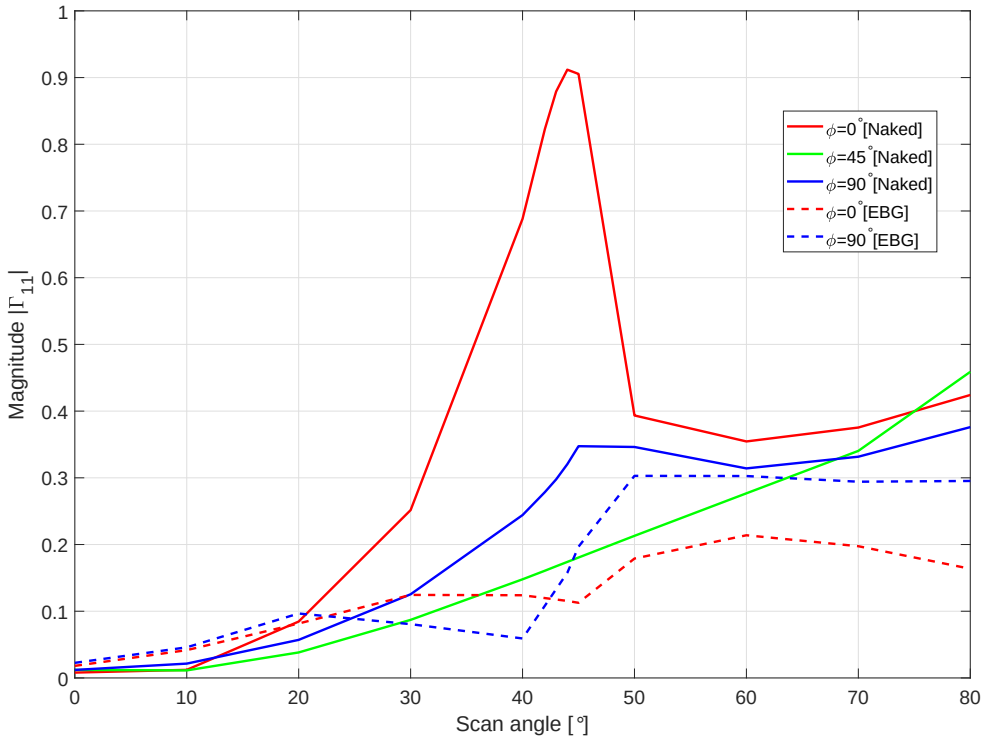

Figure 5.11: Scan performance.

Scan performance of the antenna is shown in Figure 5.11. For the naked version there is clearly a blind angle at around 44° for E-plane scanning. However, there is no blind angle for E-plane scanning for EBG geometries. This is due to suppression of surface waves using EBG material.

6

Electromagnetic Bandgap Structure on Cylindrical Radiating Geometries

A cylindrical polarimetric radar is always the best choice compared to its planar counterparts. There are several benefits of using cylindrical geometry compared to planar geometry. In a cylindrical array configuration, while scanning the beam, the sector of each cylindrical facet commutates to scan different azimuths. A very low cross-polarization can be achieved through cylindrical geometry.

The main benefits of using a cylindrical array is that the beam shape is invariant with the azimuth scanning with a constant elevation angle. Polarization is always pure along H- and V- position, since the cylindrical array is always scanning on the principal planes. In a planar array, while scanning away from principal planes, there is an issue with cross-polar biases that can be introduced due to the loss of orthogonality from electronically steering the beam away from the principal planes. Using a cylindrical array configuration, this can be easily avoided [12, 43, 44].

The cylindrical array configuration supports creeping wave modes in addition to leaky and surface wave modes. All surface and creeping waves have adverse effects on array performance. They increase the back radiation levels. In order to meet future weather

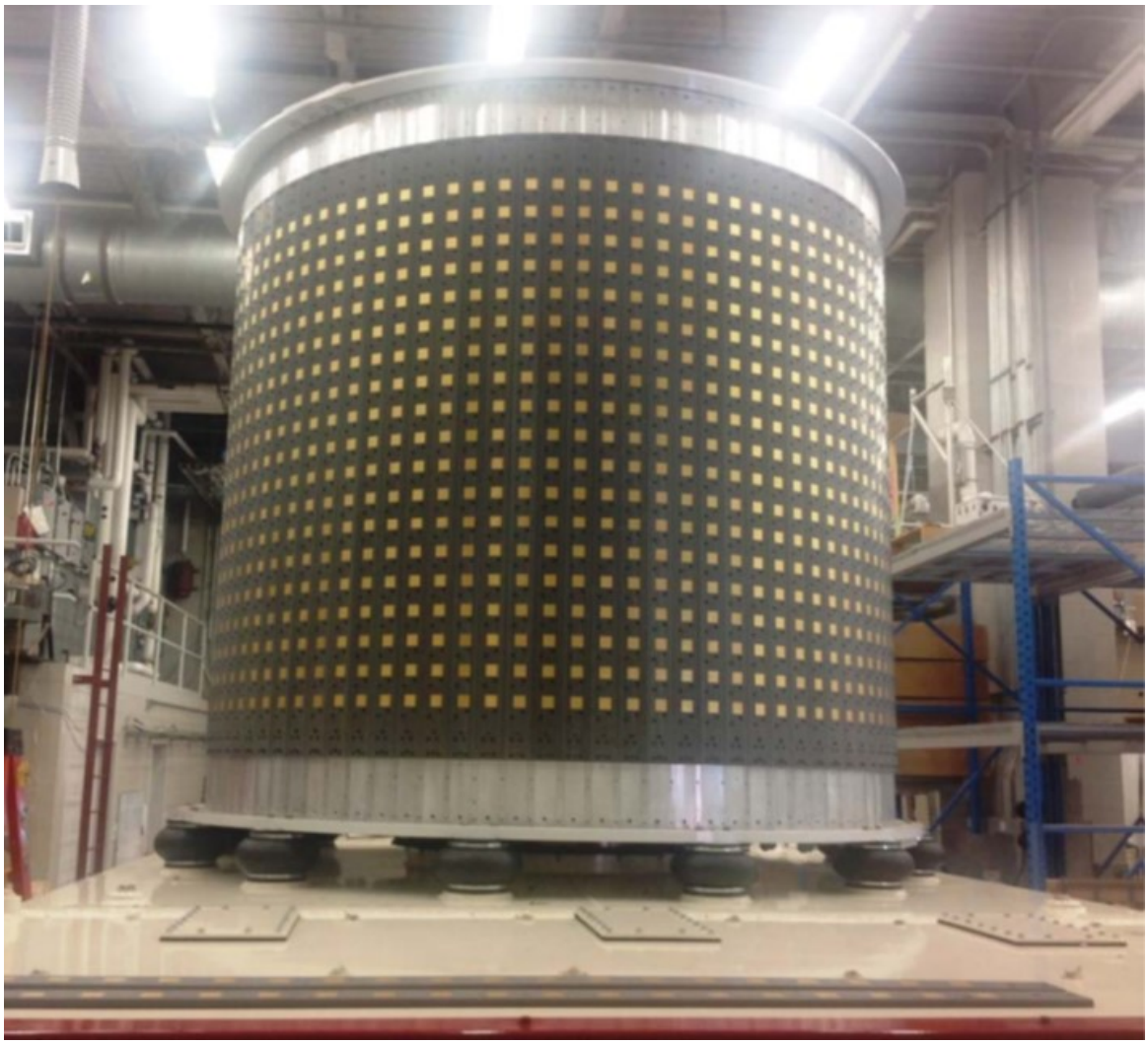

Figure 6.1: Cylindrical polarimetric phased array radar demonstrator.

observation needs, under the multifunction polarimetric phased array radar (MPAR) program, a cylindrical polarimetric phased array radar (CPPAR) was modeled, built, and tested at the Advanced Radar Research Center at the University of Oklahoma, as shown in Figure 6.1. Most of the details of the analysis, starting from modeling, beam-forming, and calibration can be found in [12, 44, 45]. This is the biggest cylindrical radar ever made for weather applications. Comparatively, the CPPAR demonstrator is a new and very uncommon technology [12]. Some of the electromagnetic behavior of the CPPAR

demonstrator is well-understood. However, a significant number of electromagnetic wave interactions with the surroundings are yet to be well-understood [12, 44]. It was found that CPPAR patterns suffer from ripples in the H-polarized pattern and a substantial amount of back radiation [12, 44]. Measurements were taken several times to better understand these behaviors. Through both measurements and simulations, it was found that there are significant amounts of back radiation. Initially, it was assumed that the ground reflections and other environmental factors might have effects on back radiation. Some new measurements were performed by putting electromagnetic absorbers where the ground reflections have the highest possibilities. There are still substantial amounts of back radiations present. The measurement results were imported to a MATLAB program to further study the phase mode spectral analysis of the measurement results. By eliminating some of the phase modes, the creeping waves dropped significantly and the back radiation improved substantially [12, 44, 45]. Since these surface and creeping waves are the root cause of the pattern's deterioration, it is crucial to suppress those surface and creeping waves to make the pattern quality as clean as possible. One of the reasons the pattern quality needs to be clean is in order to use minimal frequency spectrums or to reuse spectrums while operating the radar, instead of spending money on the frequency real estate, it is a cost effective solution [44].

The motivation of this study here is to reduce the effects of surface and creeping waves on cylindrical array geometry using electromagnetic bandgap structures and ultimately reduce the back radiation. To accurately and precisely capture the surface waves and creeping waves effects, the analysis invoked Floquet modal framework and the phase mode pattern synthesis technique [12].

6.1 Electromagnetic Bandgap on Cylindrical Structure

In the previous chapter, we designed and analyzed the planar EBG structure in a rigorous mathematical framework to suppress the surface waves on planar phased array geometries. We were able to mitigate scan blindness and improved the gain of the rectangular configurations that ultimately enhanced antenna performance. Alternatives of the planar lattice structure, cylindrical structures are a better choice for future weather applications [45]. Even though numerous papers have studied cylindrical EBG geometries, none of them address creeping and surface wave effects and back radiation [46–48].

In this chapter, a new circularly periodic EBG substrate is introduced to suppress the surface waves and creeping waves. The proposed EBG substrate is periodic based on the aperture-coupled mushroom-like structure. So, we use the same geometry to explore the suppression of surface waves on cylindrical geometry. We used the same geometrical configuration for cylindrical structures, shown in Figure 6.2, as we used for planar EBG structures. Unlike in the case of planar scan blindness, we want to eradicate the "phase mode blindness" using cylindrical EBG geometries. The analysis technique described herein includes the creeping and surface wave effects and takes into account the mutual coupling. Hence, this analysis technique is more powerful than any techniques that do not account for these effects.

6.2 Formulation for Analyzing the Simulation Results

The cylindrical array was previously studied in rigorous mathematical framework in [12]. The embedded element pattern for an N- column arrays can be expressed as [12]

$$E(\theta_s, \phi) = \frac{1}{N} \sum_{k=0}^{N-1} \sum_{n=0}^{N-1} E(\theta_s, \phi - \frac{2\pi}{N} n) e^{j\frac{2\pi}{N}nk} \tag{6.1}$$

where k is the k^{th} cylindrical phase sequence excitation (CPSE) and n is the column number. A MATLAB function was generated to take the 0^{th} element pattern, phase shift the array by $\frac{2\pi}{N}$, and add the phase shifted calculation to the total pattern. Due to the periodic nature of the cylindrical array geometries, the radiation pattern of the cylindrical array can be represented as a Fourier series, where each term in the Fourier series is a phase mode [12]. The Fourier series resulting from the far field pattern at an elevation angle θ_s and ϕ may be represented by

$$E(\theta_s, \phi).\hat{\boldsymbol{n}} = \sum_{m=-\infty}^{\infty} a_m e^{jm\phi} \tag{6.2}$$

where $\hat{\boldsymbol{n}}$ is the unit vector normal to the far field pattern at a specific elevation angle θ_s, and a_m is the phase mode coefficients. The vector form of the antenna can be written as [12]

$$n = \frac{N}{2\pi} K_{sw} r\Delta\phi + pN \tag{6.3}$$

where p is any integer, and $r\Delta\Phi$ is the azimuth element spacing. The first fundamental term here is larger than $n_{max} = k_0 r$ and has little contribution to the radiation. The radiation index $p = -1$ case, the contribution of the surface waves typically cancels out the direct radiation from the exciting element. In general, excitation of surface waves is identified as the primary contributor of the pattern degradations for the H-polarization.

6.3 Unit Cell Set Up

The behavior of planar arrays is well-understood, while a planar antenna is analyzed under Floquet framework. The Floquet framework accounts for the mutual coupling and scan impedance effects. It is a very powerful method to accurately predict any infinite to finite sized antenna performance in the array environment [9, 18]. In general, the simulation

in Floquet analysis is performed using the center element or geometry while computing remaining elements in parallel to avoid computing thousands of elements in parallel. A similar approach is applied to simulate the cylindrical geometry because of the cylinder's axial symmetry. This kind of method was applied earlier in a rigorous mathematical framework to predict the performance of cylindrical array antenna geometry [12]. The same procedure is applied to simulate this cylindrical EBG geometry. This kind of simulation technique helps to accurately predict antenna performance using much less time and fewer computational resources. Typically, the usage of computer resources goes up by $\boldsymbol{N^3}$ for the conventional array geometry, where $\boldsymbol{N}$ is the number of elements in the array, while the computational usage for the unit-cell technique increases linearly with $\boldsymbol{N}$. Hence, for any medium to large arrays, this approach to the unit cell method is advantageous.

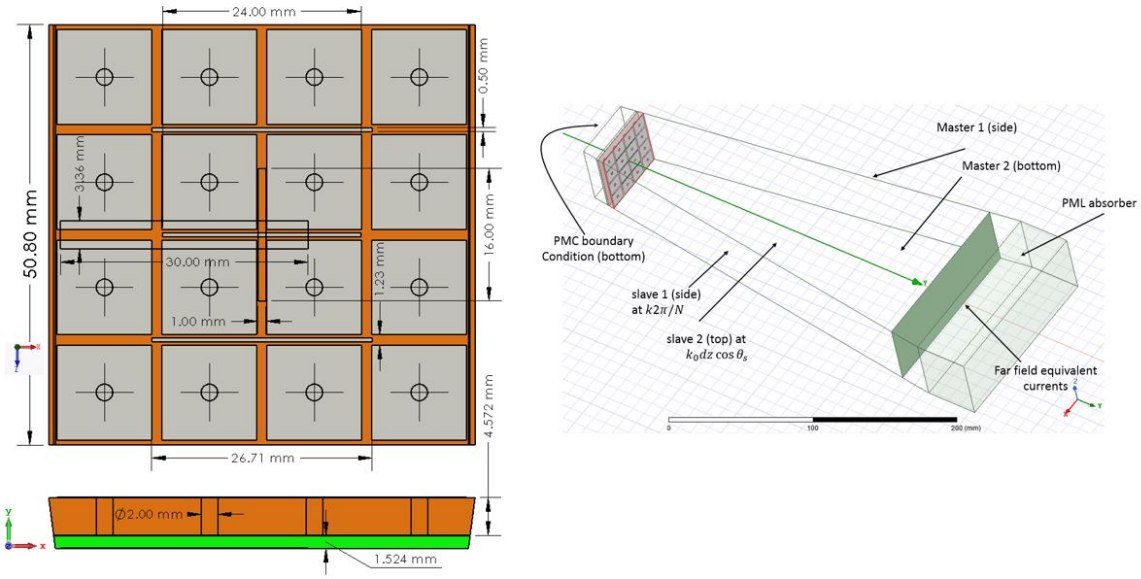

Figure 6.2: Cylindrical EBG set up.

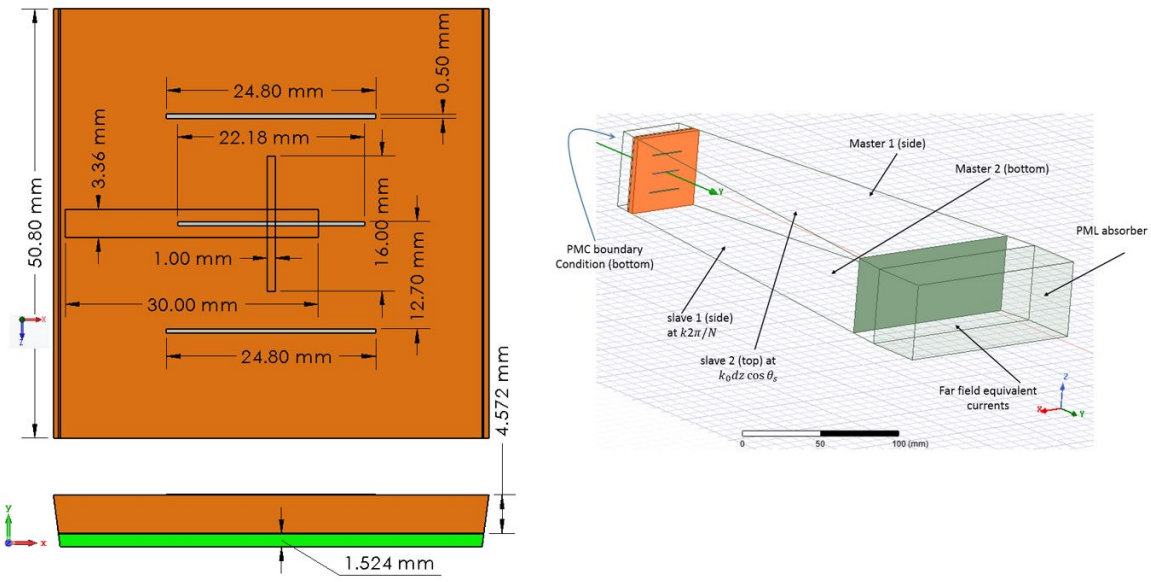

Figure 6.3: Cylindrical naked/uniform substrate set up.

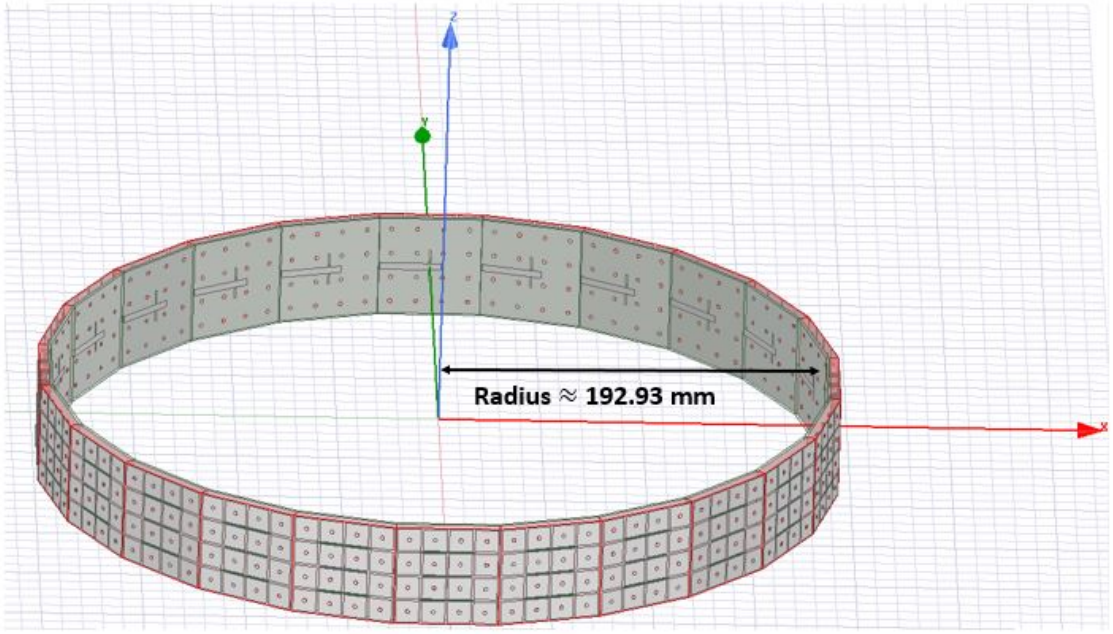

Figure 6.4: Cylindrical EBG geometry set up for 24 columns.

For the simulation set-up over here, as shown in Figure 6.2 and Figure 6.3, the cylinder is positioned axially along the z-direction with the 0^{th} element directed along positive y-axis in such a way that the elevation angle is $\theta_{ele} = (90° - \theta_s)$ and the azimuth angle is $\phi_{az} = (90° - \phi_s)$, when the 0^{th} element is considered at broadside. A typical 24-column cylindrical EBG geometry set-up is shown in Figure 6.4, as an example. For this specific geometrical configuration, the radius of the cylinder is approximately 192.93 mm, while for 96-columns it is about 775.89 mm. Even though the set-up shows all 24 columns around the cylinder, the simulation will compute only the center element. Particularly, the 0^{th} element, and use master/slave boundary conditions to emulate the full array of elements.

The first master/slave boundary conditions are located on the air-box and are perpendicular to the x-y plane. The first master/slave boundary conditions create a phase difference between the master and slave by $\frac{2\pi k}{N}$ to emulate a fully populated cylinder in the azimuthal direction. The first master/slave boundary conditions are located on the air-box surfaces, which are parallel to the x-y plane. These two boundaries emulate currents on these surfaces as if there were an infinite array of elements both above and beneath the unit-cell. The slave-1 boundary condition follows a phase difference of $k_0 dz \cos\theta_s$ between the bottom and top boundaries.

A perfectly matched layer (PML) boundary condition is applied as a wedge-shaped square air-box on the top of the geometry. PML is a reflection-free boundary condition. If PML is not there, the default radiation boundary for HFSS would be a short circuit at the end of the air-box. This would result disruptions in the radiation patterns that would not physically be present in an experimental measurement. At the bottom, a perfect magnetic boundary condition is applied at a distance of at least six times of the feed substrate height.

6.4 Convergence Consideration

Convergence is an important issue for any numerical method because it is necessary to understand where, in angular and phase mode domains, it is invalid due to numerical and boundary conditions. Unfortunately, most of the literature does not explicitly discuss numerical convergence issues. The key to a successful electromagnetic field simulation is to begin with simple, and easily manageable problems for which the solution is known in advance. This helps the designer to build a sound technical judgment and an appreciation for the sensitivity of the solution to various design parameters. Techniques for error-checking and assessment of convergence can thus be systematically articulated and refined. When simulating a cylindrical unit cell using full wave solver, for instance, with HFSS, it is very important that one studies the convergence issues to get the correct solution of the geometry. In HFSS, a PML is a radiation boundary that emulates reflection-free radiation [49]. For a given geometry and set of boundary conditions, HFSS ensures one will not receive any false numerical convergence. Even though PML requires more RAM, PMLs absorb a much wider range of waves in terms of frequency and direction. For a cylindrical geometry's unit cell set-up, the PML boundary should provide an appropriate termination for the cylindrical harmonics/phase modes that are above cutoff within the unit cell for each CPSE [12]. However, we found a potential sensitivity of the placement of PML that terminates the unit cell. In our simulation the PML distance is adjusted to observe how PML distance affects convergence of the simulation.

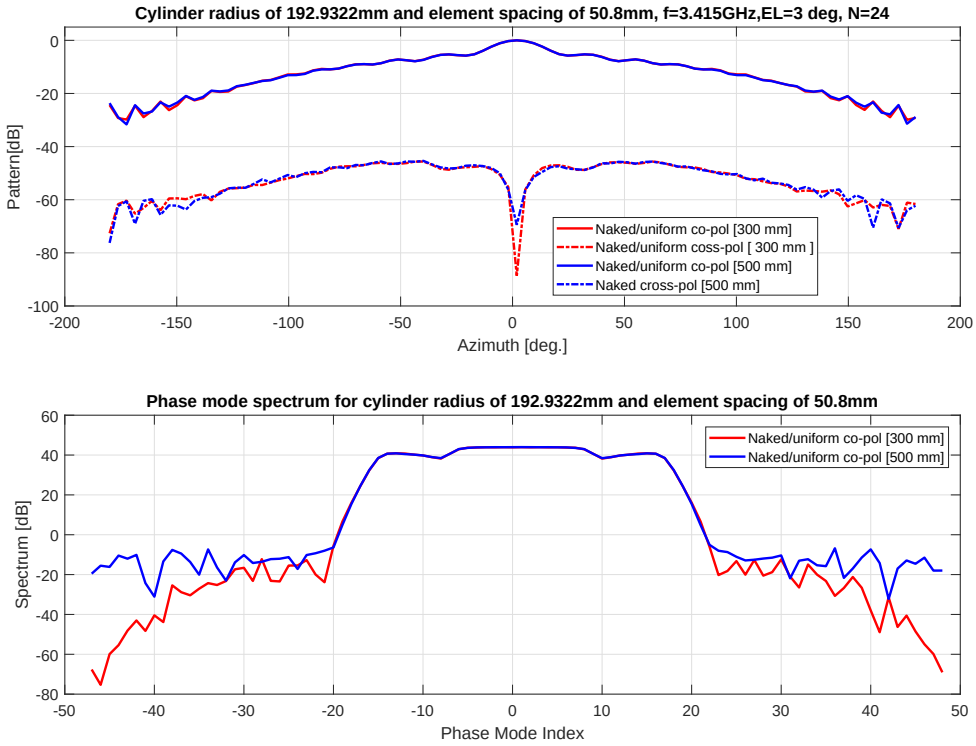

Figure 6.5: Cylindrical simulation results comparison for naked/uniform substrate while PML 300 mm vs. 500 mm away from the radiating surface [$N = 24$].

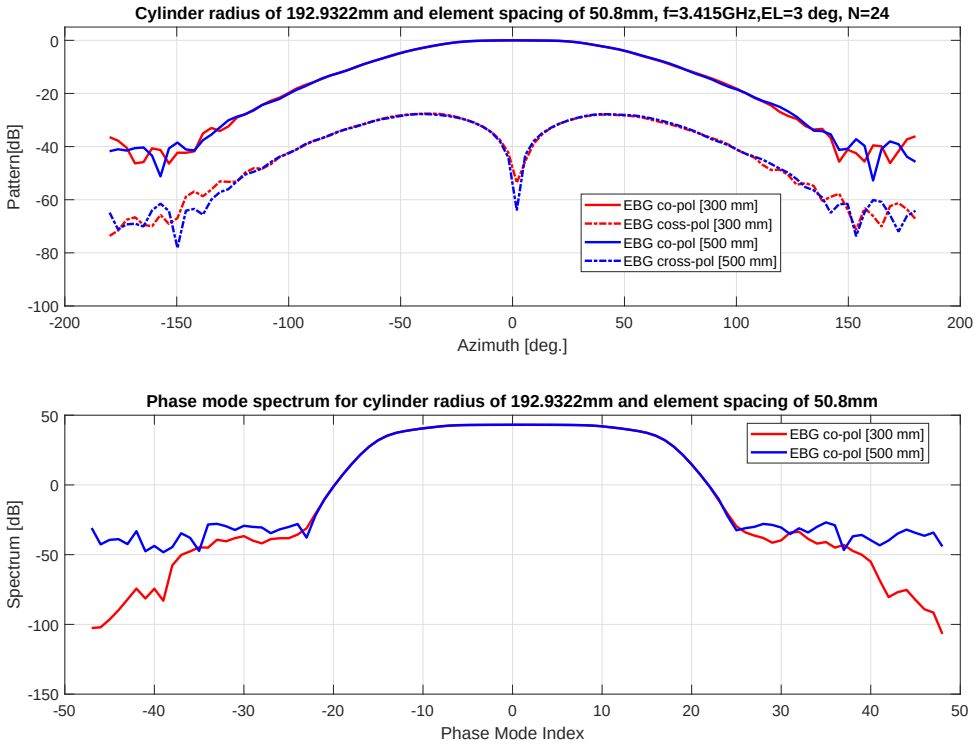

Figure 6.6: Cylindrical simulation results comparison for EBG substrate while PML 300 mm vs. 500 mm away from the radiating surface [$N = 24$].

Figure 6.5 and Figure 6.6 compare the simulation results for PML termination 300 mm vs. PML 500 mm away from the radiating surface for H-pol, for cylindrical geometries on a uniform substrate and on an EBG substrate, respectively. Apparently, there are excess ripples in the co-pol patterns, and elevated back radiation observable for the naked case. The phase mode analysis shows that, for both the EBG and naked cases, even though PML is more than 3λ away, it is still modifying the simulation results.

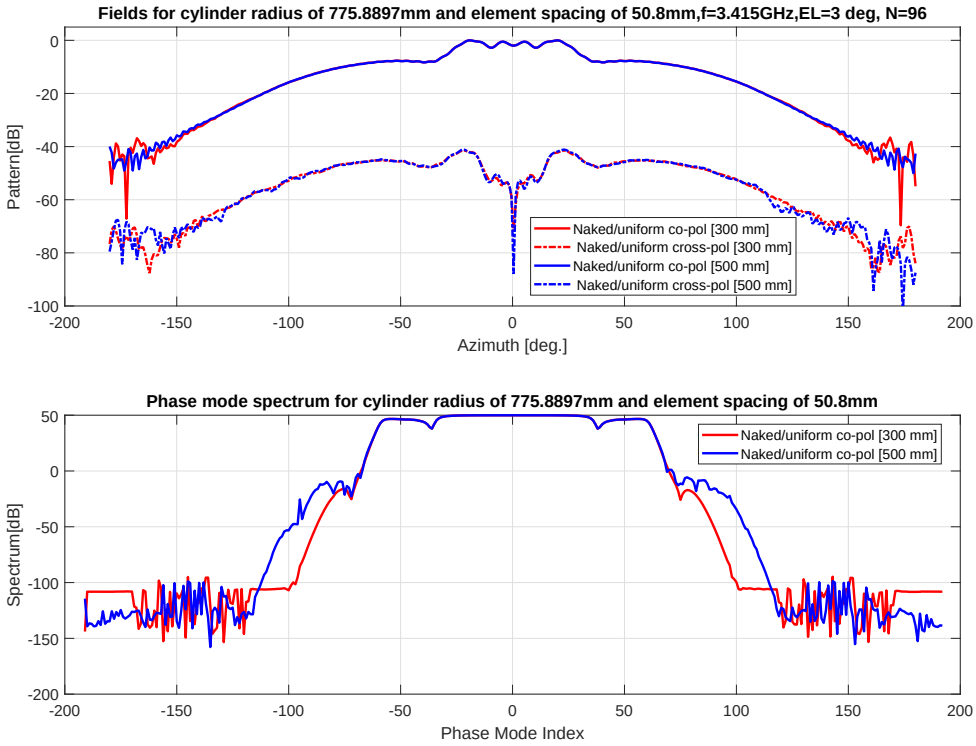

Figure 6.7: Cylindrical simulation results comparison for naked/uniform substrate while PML 300 mm vs. 500 mm away from the radiating surface [$N = 96$].

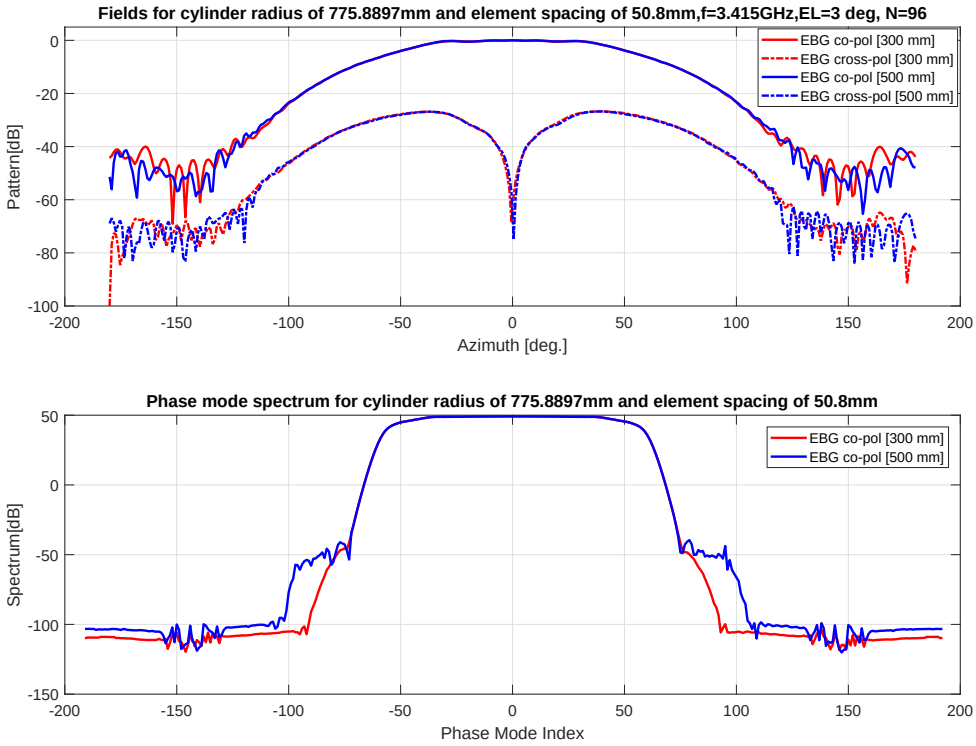

Figure 6.8: Cylindrical simulation results comparison for EBG substrate while PML 300 mm vs. 500 mm away from the radiating surface [$N = 96$].

This behavior is much more visible when the number of elements is increased to 96. Similar behavior is apparent for 96 elements as well and is depicted in Figure 6.7 and Figure 6.8 for naked and EBG structures, respectively. The 500 mm case obviously gives fewer numerical convergence issues and better results. The closer the PML is to the radiating surface, the more phase mode spectrum acts inappropriately. From this we can conclude that, for more complex antenna design, the PML should be placed more than 5λ away to ensure convergence issues do not interfere with the simulated results.

.

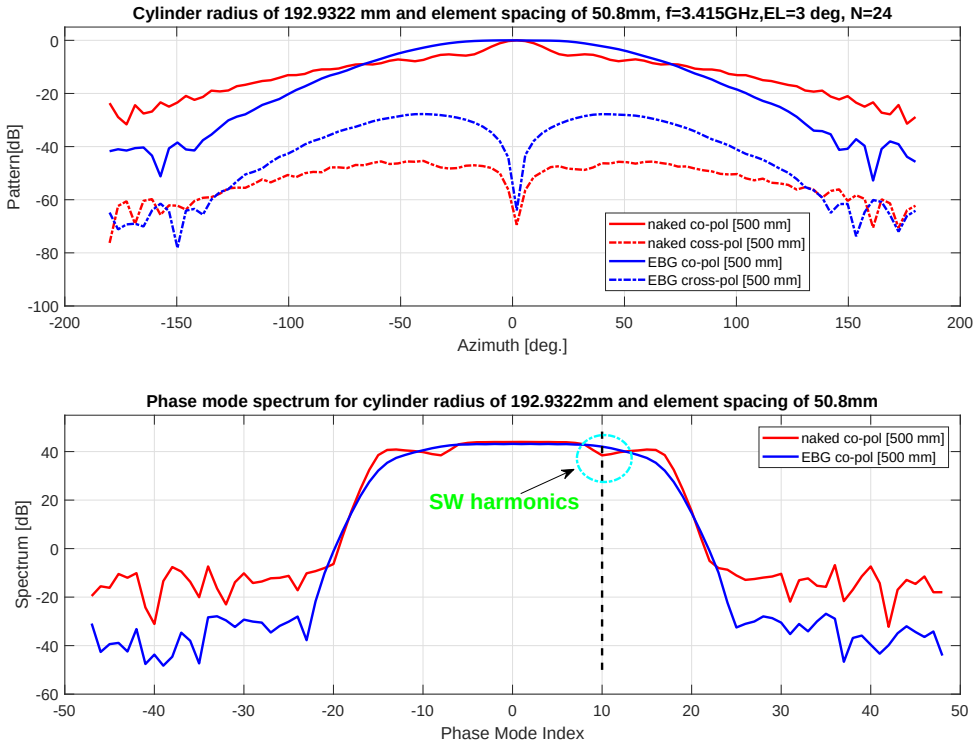

Figure 6.9: Cylindrical comparison while PML 500 mm away from the radiating surface $[N = 24]$.

6.5 Comparison and Analysis of the Simulation Results

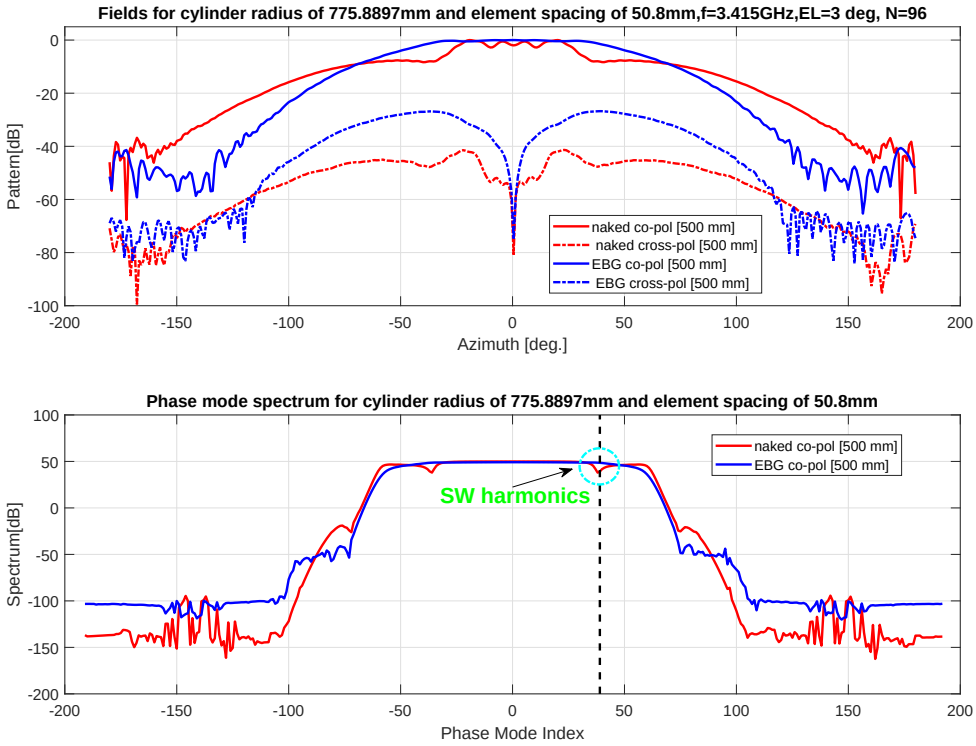

Figure 6.10: Cylindrical comparison while PML 500 mm away from the radiating surface $[N = 96]$.

As we discussed in an earlier section, we first analyzed our geometry with number of elements $N = 24$. The comparison of the results is shown in Figure 6.9. The 500 mm case results are shown here as it gives better convergence. As can be seen, there are significant improvements in the EBG cylindrical pattern. There are no ripples observed in the co-pol pattern of cylindrical EBG structure. We also studied the $N = 96$ element cylindrical pattern and the simulation results are shown in Figure 6.10. Certainly, while exciting H-polarization, there are significant ripples observed near the broadside radiation for naked/uniform cases for both settings. With the aid of phase mode analysis, it is found

that in the naked case certain phase modes do not radiate. This is caused by a surface wave on the grounded dielectric slab that leads to "phase mode blindness" which is similar to "scan blindness" on planar equivalent cases discussed in the previous chapter. Therefore, these ripples complicate the pattern synthesis. On the other hand, there are no ripples for EBG geometries. This indicates that by using cylindrical EBG structure, one can eliminate surface and creeping wave effects on cylindrical geometries and can improve the antenna performance.

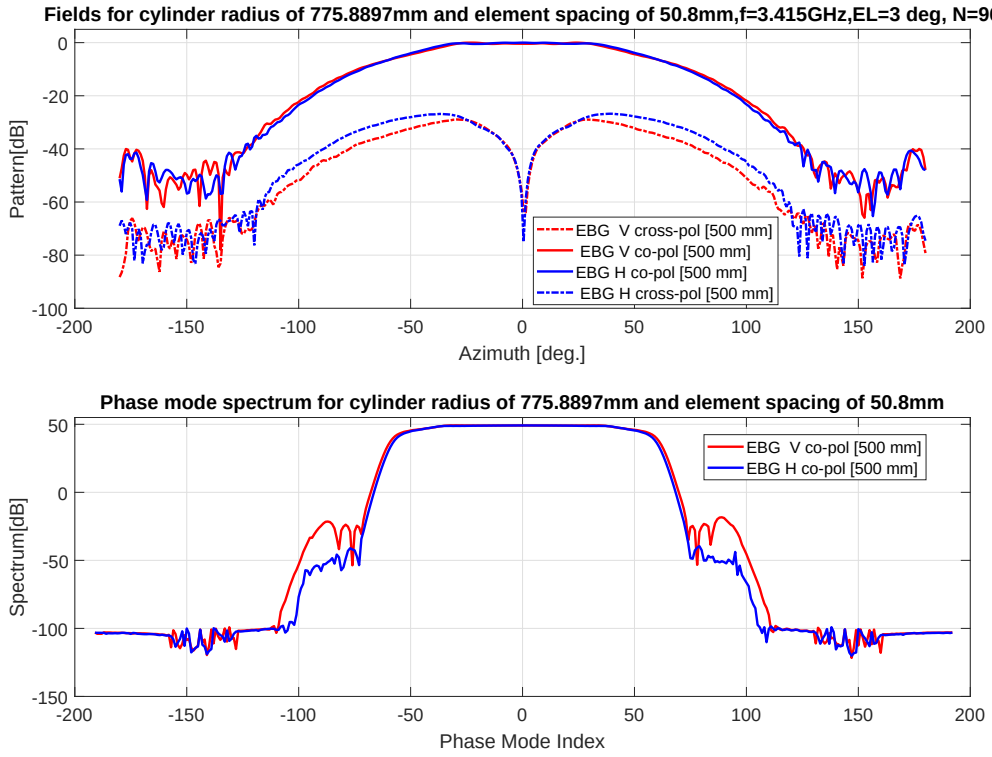

Figure 6.11: Cylindrical comparison while PML 500 mm away from the radiating surface $[N = 96]$.

In a separate simulation, dipole antennas are placed along vertically. The comparison of the simulation results for both $V-$pol and $H-$pol are shown in Figure 6.11. Both

patterns are symmetric and matched very well. From the graphs it is seen that using cylindrical EBG structures, the suppression of phase mode blindness is possible.

6.6 Conclusions

This chapter has presented the design, analysis, techniques, and simulation of a new cylindrical EBG structures for multifunction radar application as a development effort for future weather surveillance needs. The proposed cylindrical EBG structure has several advantages to improve the pattern quality and the overall antenna performance. For example, the creeping and surface wave excitation that is dominant in uniform substrate geometries can easily be suppressed using these cylindrical EBG geometries. The back radiation can be improved considerably. The "phase mode blindness", which occurs due to coherent coupling of creeping and surface waves to the radiated space waves is totally eliminated. This analysis involved a rigorous mathematical framework referred to as the phase mode analysis technique. By comparing both polarization simulation results, precise matching between co-pol beam patterns is achieved.

To achieve the appropriate convergence, PML is placed at different distances from the radiating surface of the antenna. It was seen that if the PML is placed too close to the antenna surface in the unit cell, the far field radiation pattern is affected substantially and relative convergence error occurs. For accurate analysis, the PML should be placed at least 5λ apart from the radiating surface for the complicated and multilayer cylindrical structure discussed in this chapter.

Finally, the next step would be to fabricate and measure this cylindrical geometry within the facilities of ARRC at the University of Oklahoma. A good comparison between

measurement and simulation results would be a fantastic aid to the ongoing effort to develop the next-generation cylindrical phased array radar. Overall, the proposed cylindrical EBG element could be an ideal choice for weather and MPAR applications.

7

Summary and Conclusion

This dissertation presents an investigation into the theory and applications of Floquet analysis on finite phased array applications. It was found that even though there is a very small gap, as small as 1 mm in-between the sub-arrays, this has a huge impact on the cross-polarization level increase. These periodic gap currents get radiated and contribute to increasing the cross-polarization of the antennas.

Furthermore, the proposed scanning phased array antenna with EBG has promising potential for the future generation of phased array antennas with reduced surface waves beyond the commonly used half-wavelength element spacing. They have numerous utilization in weather applications and remote sensing, surveillance systems, wide-angle scanning radars, automotive radars such as collision avoidance, massive multi-input/multi-output radars, intelligent vehicle highways, autonomous cruise control radars, and many more.

The simulation results shows there are significant improvements in surface wave suppression of cylindrical EBG geometries. This is due to TM surface wave suppression. To validate its results, cylindrical EBG geometries need to be built and tested. For future weather radar, this kind of effort will be helpful to mitigate adverse effects of creeping and surface waves.

7.1 Future Works

We have analyzed the Floquet modal analysis for grating lobe effects of finite sized sub-arrays. The study could be extended to multilayer arrays with different periodicities and axis orientations. This type of analysis requires modal mapping between different sets of Floquet modes due to different periodicities.

Even though the mushroom EBG structure was able to remove the scan blindness, the antenna impedance bandwidth was very narrow. It is just the starting point to investigate the EBG structure on weather applications. It would be very interesting for future work to design a very broad-band antenna, while at the same time suppressing the surface waves. There are many parameters that need to be investigated to observe the bandwidth behavior. For instance, the wider the mushroom patch hat, the more capacitance it generates. We need to explore the bandwidth characteristics upon patch hats, vias, thickness etc.

In this dissertation, each antenna design was for specific frequency band and operated to be in a single state. In practical environments, these impedance surfaces can be made tunable or reconfigurable by using varactors, switches, tunable materials or other methods. This would give additional flexibility to operate the antennas over different frequency bands or in different settings.

In addition, the bandwidth enhancement of the cylindrical array geometry using EBG surface would be an interesting research topic for future work. Surface wave suppression on cylindrical arrays would be a significant improvement for cylindrical geometries. However, in any case, the cost and design challenges of high impedance surfaces are generally increased, as compared to the static and passive surface. Many attempts have been taken in the past to solve these problems. However, these attempts only were partially successful. These problems can be solved through more intuitive knowledge, understating, and rigorous research.

The next-generation phased array radar would be based on a digital beam-forming technique. In this method, all the signals from the antenna elements will be collected into a computer. Therefore, beam-forming can be performed using software instead of hardware. As a consequence, generating multiple beams, adaptive nulling, lowering sidelobes, grating lobes suppression and many other signal processing techniques can be employed, even though it would be costly to implement. Conformal arrays would be another amazing technology. Spherical arrays though, have many benefits like total hemispherical coverage, polarization, mismatch loss compared to planar arrays but are difficult to build. As demand continues to increase, more challenges will come along with existing challenges. The designer's task would be to overcome these challenges and make it affordable.

Bibliography

[1] R. Garg, P. Bhartia, I. J. Bahl, and A. Ittipiboon, *Microstrip antenna design handbook*. Artech house, 2001.

[2] F. Yang and Y. Rahmat-Samii, *Electromagnetic band gap structures in antenna engineering*. Cambridge university press Cambridge, UK, 2009.

[3] R. J. Mailloux, *Phased array antenna handbook*. Artech house, 2017.

[4] W. L. Stutzman and G. A. Thiele, *Antenna theory and design*. John Wiley & Sons, 2012.

[5] A. K. Bhattacharyya, *Phased array antennas: Floquet analysis, synthesis, BFNs and active array systems*. John Wiley & Sons, 2006, vol. 179.

[6] C. A. Balanis, *Modern antenna handbook*. John Wiley & Sons, 2011.

[7] W. L. Stutzman and C. G. Buxton, "Radiating elements for wideband phased arrays," *Microwave Journal*, vol. 43, no. 2, p. 130, 2000.

[8] J. Huang, "The finite ground plane effect on the microstrip antenna radiation patterns," *IEEE Transactions on Antennas and Propagation*, vol. 31, no. 4, pp. 649–653, 1983.

[9] L. M. Bhowmik and C. J. Fulton, "Floquet modal analysis of grating lobe effects for finite planar arrays," in *2015 Antenna Applications Symposium*, 2015.

[10] T. E. Christian, H. Loui, C. G. Christodoulou, and D. F. Dubbert, "A new approach for in-situ scan impedance characterization of scanned antenna arrays," in *Antennas and Propagation Society International Symposium (APSURSI), 2013 IEEE*. IEEE, 2013, pp. 304–305.

[11] J. R. Mailoux, "Phased array antenna handbook," *Artech House, Boston*, 2005.

[12] C. J. Fulton, "Phase mode analysis of a cylindrical polarimetric phased array antenna," in *2014 IEEE Antenna Applications Symposium*. Robert Allerton Park,Monticello,Illinois, September 23-25, 2014.

[13] H. A. Wheeler, "The radiation resistance of an antenna in an infinite array or waveguide," *Proceedings of the IRE*, vol. 36, no. 4, pp. 478–487, 1948.

[14] L. Stark, "Radiation impedance of a dipole in an infinite planar phased array," *Radio Science*, vol. 1, no. 3, pp. 361–378, 1966.

[15] H. Wheeler, "The grating-lobe series for the impedance variation in a planar phased-array antenna," *IEEE Transactions on Antennas and Propagation*, vol. 14, no. 6, pp. 707–714, 1966.

[16] G. Farrell and D. Kuhn, "Mutual coupling in infinite planar arrays of rectangular waveguide horns," *IEEE Transactions on Antennas and Propagation*, vol. 16, no. 4, pp. 405–414, 1968.

[17] G. H. Knittel, A. Hessel, and A. A. Oliner, "Element pattern nulls in phased arrays and their relation to guided waves," *Proceedings of the IEEE*, vol. 56, no. 11, pp. 1822–1836, 1968.

[18] A. K. Bhattacharyya, "An accurate model for finite array patterns based on floquet modal theory," *Antennas and Propagation, IEEE Transactions on*, vol. 63, no. 3, pp. 1040–1047, 2015.

[19] R. J. Mailloux, "Phased array antenna handbook," *Boston, MA: Artech House, 1994.*, 1994.

[20] W. H. Von Aulock, "Properties of phased arrays," *Proceedings of the IRE*, vol. 48, no. 10, pp. 1715–1727, 1960.

[21] Allen C. Newell and Greg Hindmam, "Antenna spherical coordinate systems and their application in combining results from different antenna orientations," in *Antenna Meaurement Techniques Assocaition (AMTA) Symposium.* Carson,CA, 1999.

[22] L. M. Bhowmik, C. Armiento, A. Akyurtlu, W. Miniscalco, J. Chirravuri, and C. McCarroll, "Design and analysis of conformal ku-band microstrip patch antenna arrays," in *2013 IEEE International Symposium on Phased Array Systems and Technology.* IEEE, 2013, pp. 815–820.

[23] T. A. Milligan, T. A. Milligan, T. A. Milligan, and T. A. Milligan, *Modern antenna design.* Wiley Online Library, 2005.

[24] D. Sievenpiper, L. Zhang, R. F. Broas, N. G. Alexopolous, E. Yablonovitch *et al.*, "High-impedance electromagnetic surfaces with a forbidden frequency band," *IEEE Transactions on Microwave Theory and techniques*, vol. 47, no. 11, pp. 2059–2074, 1999.

[25] C. A. Balanis, *Antenna theory: analysis and design.* John wiley & sons, 2016.

[26] D. F. Sievenpiper, "High-impedance electromagnetic surfaces." 2000.

[27] C. Wang, S. Kim, E. Li, D. F. Sievenpiper *et al.*, "Simulation analysis of electromagnetic surface wave suppression by soft surfaces, including effects of resistive and active elements," *IEEE Antennas and Wireless Propagation Letters*, vol. 17, no. 12, pp. 2394–2398, 2018.

[28] V. R. Komanduri, D. R. Jackson, J. T. Williams, and A. R. Mehrotra, "A general method for designing reduced surface wave microstrip antennas," *IEEE Transactions on Antennas and Propagation*, vol. 61, no. 6, pp. 2887–2894, 2013.

[29] H.-Y. Yang, R. Kim, and D. R. Jackson, "Design consideration for modeless integrated circuit substrates using planar periodic patches," *IEEE Transactions on Microwave Theory and Techniques*, vol. 48, no. 12, pp. 2233–2239, 2000.

[30] M. G. Silveirinha, C. A. Fernandes, J. R. Costa *et al.*, "Electromagnetic characterization of textured surfaces formed by metallic pins," 2008.

[31] E. Adas, F. De Flaviis, and N. G. Alexopoulos, "Scan blindness-free electromagnetic bandgap phased arrays," in *Antennas and Propagation & USNC/URSI National Radio Science Meeting, 2017 IEEE International Symposium on.* IEEE, 2017, pp. 1593–1594.

[32] S. Sengupta, D. R. Jackson, and S. A. Long, "Modal analysis and propagation characteristics of leaky waves on a 2-d periodic leaky-wave antenna," *IEEE Transactions on Microwave Theory and Techniques*, vol. 66, no. 3, pp. 1181–1191, 2018.

[33] F.-R. Yang, K.-P. Ma, Y. Qian, and T. Itoh, "A uniplanar compact photonic-bandgap (uc-pbg) structure and its applications for microwave circuits," *IEEE Transactions on microwave theory and techniques*, vol. 47, no. 8, pp. 1509–1514, 1999.

[34] M. S. Alam, M. T. Islam, and N. Misran, "A novel compact split ring slotted electromagnetic bandgap structure for microstrip patch antenna performance enhancement," *Progress in Electromagnetics Research*, vol. 130, pp. 389–409, 2012.

[35] Y. Yao, X. Wang, and Z. Feng, "A novel dual-band compact electromagnetic bandgap (ebg) structure and its application in multi-antennas," in *2006 IEEE Antennas and Propagation Society International Symposium*. IEEE, 2006, pp. 1943–1946.

[36] B.-Q. Lin, X.-Y. Ye, X.-Y. Cao, and F. Li, "Uniplanar ebg structure with improved compact and wideband characteristics," *Electronics Letters*, vol. 44, no. 23, pp. 1362–1363, 2008.

[37] M. Alam, N. Misran, B. Yatim, M. T. Islam *et al.*, "Development of electromagnetic band gap structures in the perspective of microstrip antenna design," *International Journal of Antennas and Propagation*, vol. 2013, 2013.

[38] M. Hellen and I. Craddock, "Calculation of the input impedance of dipoles in proximity to walls," *IEE Proceedings-Microwaves, Antennas and Propagation*, vol. 150, no. 5, pp. 369–374, 2003.

[39] S. R. Best and D. L. Hanna, "Design of a broadband dipole in close proximity to an ebg ground plane," *IEEE Antennas and propagation magazine*, vol. 50, no. 6, pp. 52–64, 2008.

[40] F. Yang and Y. Rahmat-Samii, "Reflection phase characterizations of the ebg ground plane for low profile wire antenna applications," *IEEE Transactions on Antennas and Propagation*, vol. 51, no. 10, pp. 2691–2703, 2003.

[41] G. Kumar and K. P. Ray, *Broadband microstrip antennas*. Artech house, 2003.

[42] Z. N. Chen and M. Y. W. Chia, *Broadband Planar Antennas*. Wiley Online Library, 2006.

[43] G. Zhang, R. J. Doviak, D. S. Zrnić, R. Palmer, L. Lei, and Y. Al-Rashid, "Polarimetric phased-array radar for weather measurement: A planar or cylindrical configuration?" *Journal of Atmospheric and Oceanic Technology*, vol. 28, no. 1, pp. 63–73, 2011.

[44] K. Sperzel and C. J. Fulton, "Mechanisms for generation and suppression of creeping waves on a radiating cylindrical structure," in *2017 IEEE Antenna Applications Symposium*. Robert Allerton Park,Monticello,Illinois, September, 2017.

[45] C. Fulton, J. L. Salazar, Y. Zhang, G. Zhang, R. Kelly, J. Meier, M. McCord, D. Schmidt, A. D. Byrd, L. M. Bhowmik *et al.*, "Cylindrical polarimetric phased array radar: Beamforming and calibration for weather applications," *IEEE Transactions on Geoscience and Remote Sensing*, vol. 55, no. 5, pp. 2827–2841, 2017.

[46] H. Boutayeb and T. A. Denidni, "Gain enhancement of a microstrip patch antenna using a cylindrical electromagnetic crystal substrate," *IEEE transactions on antennas and propagation*, vol. 55, no. 11, pp. 3140–3145, 2007.

[47] V. Jandieri, K. Yasumoto, and Y.-K. Cho, "Rigorous analysis of electromagnetic scattering by cylindrical ebg structures," *Progress In Electromagnetics Research*, vol. 121, pp. 317–342, 2011.

[48] H. Boutayeb, T. A. Denidni, K. Mahdjoubi, A.-C. Tarot, A.-R. Sebak, and L. Talbi, "Analysis and design of a cylindrical ebg-based directive antenna," *IEEE Transactions on Antennas and Propagation*, vol. 54, no. 1, pp. 211–219, 2006.

[49] [Online]. Available: https://www.ansys.com/-/media/ansys/corporate/resourcelibrary/techbrief/ab-hfss-perfectly-matched-layer-boundary-automation.pdf.

[50] D. R. Jackson and A. A. Oliner, "Leaky-wave antennas," *Modern antenna handbook*, pp. 325–367, 2008.

[51] L. Zhang, J. A. Castaneda, and N. G. Alexopoulos, "Scan blindness free phased array design using pbg materials," *IEEE Transactions on Antennas and Propagation*, vol. 52, no. 8, pp. 2000–2007, 2004.

[52] D. F. Sievenpiper, "Forward and backward leaky wave radiation with large effective aperture from an electronically tunable textured surface," *IEEE transactions on antennas and propagation*, vol. 53, no. 1, pp. 236–247, 2005.

[53] F. Xu and K. Wu, "Numerical multimode calibration technique for extraction of complex propagation constants of substrate integrated waveguide," in *Microwave Symposium Digest, 2004 IEEE MTT-S International*, vol. 2. IEEE, 2004, pp. 1229–1232.

[54] ——, "Guided-wave and leakage characteristics of substrate integrated waveguide," *IEEE Transactions on microwave theory and techniques*, vol. 53, no. 1, pp. 66–73, 2005.

[55] F. Xu, A. Patrovsky, and K. Wu, "Fast simulation of periodic guided-wave structures based on commercial software," *Microwave and Optical Technology Letters*, vol. 49, no. 9, pp. 2180–2182, 2007.

[56] F. Xu, Y. Zhang, W. Hong, K. Wu, and T. J. Cui, "Finite-difference frequency-domain algorithm for modeling guided-wave properties of substrate integrated waveguide," *IEEE Transactions on Microwave Theory and Techniques*, vol. 51, no. 11, pp. 2221–2227, 2003.

[57] C. Balanis, *Antenna Theory: Analysis and Design*. Wiley, 2015.

[58] F. Xu, K. Wu, and W. Hong, "Equivalent resonant cavity model of arbitrary periodic guided-wave structures and its application to finite-difference frequency-domain algorithm," *IEEE Transactions on Microwave Theory and Techniques*, vol. 55, no. 4, pp. 697–702, 2007.

[59] Y. Saad, "Algorithms and architectures for advanced scientific computing," *Numerical Methods for Large Eigenvalue Problems*.

[60] D. M. Pozar, "Scanning characteristics of infinite arrays of printed antenna subarrays," *IEEE transactions on antennas and propagation*, vol. 40, no. 6, pp. 666–674, 1992.

[61] H. Howe Jr, "Stripline is alive and well," *Microwave Journal*, vol. 14, p. 25, 1971.

[62] A. Vosoogh and P.-S. Kildal, "Simple formula for aperture efficiency reduction due to grating lobes in planar phased arrays," *IEEE Transactions on Antennas and Propagation*, vol. 64, no. 6, pp. 2263–2269, 2016.

[63] R. C. Hansen, *Phased array antennas*. John Wiley & Sons, 2009, vol. 213.

[64] A. Ishimaru, R. J. Coe, G. E. Miller, and W. P. Geren, "Finite periodic structure approach to large scanning array problems," *Antennas and Propagation, IEEE Transactions on*, vol. 33, no. 11, pp. 1213–1220, 1985.

[65] A. K. Skrivervik and J. R. Mosig, "Analysis of finite phase arrays of microstrip patches," *Antennas and Propagation, IEEE Transactions on*, vol. 41, no. 8, pp. 1105–1114, 1993.

[66] A. K. Bhattacharyya, "Floquet-modal-based analysis for mutual coupling between elements in an array environment," in *Microwaves, Antennas and Propagation, IEE Proceedings*, vol. 144, no. 6. IET, 1997, pp. 491–497.

[67] A.K. Bhattacharyya, "Accuracy of floquet model in predicting performances of finite arrays," *Antennas and Wireless Propagation Letters, IEEE*, vol. 13, pp. 19–22, 2014.

[68] A. J. Roscoe, R. Perrott *et al.*, "Large finite array analysis using infinite array data," *Antennas and Propagation, IEEE Transactions on*, vol. 42, no. 7, pp. 983–992, 1994.

[69] B. Tomasic and A. Hessel, "Analysis of finite arrays-a new approach," *Antennas and Propagation, IEEE Transactions on*, vol. 47, no. 3, pp. 555–565, 1999.

[70] D. Ludick, U. Jakobus, and D. Davidson, "Numerical analysis of finite antenna arrays using the domain green's function method," in *Electromagnetics in Advanced Applications (ICEAA), 2012 International Conference on.* IEEE, 2012, pp. 216–219.

[71] H. R. Hassani and M. Jahanbakht, "Method of moment analysis of finite phased array of aperture coupled circular microstrip patch antennas," *Progress In Electromagnetics Research B*, vol. 4, pp. 197–210, 2008.

[72] A. Taflove and S. C. Hagness, *Computational electrodynamics.* Artech house, 2005.

[73] J.-M. Jin, *The finite element method in electromagnetics.* John Wiley & Sons, 2014.

[74] C. A. Balanis, *Advanced engineering electromagnetics.* Wiley Online Library, 2012, vol. 111.

[75] M. Costa, A. Richter, and V. Koivunen, "Unified array manifold decomposition based on spherical harmonics and 2-d fourier basis," *Signal Processing, IEEE Transactions on*, vol. 58, no. 9, pp. 4634–4645, 2010.

[76] D. Davies, "A transformation between the phasing techniques required for linear and circular aerial arrays," in *Proceedings of the Institution of Electrical Engineers*, vol. 112, no. 11. IET, 1965, pp. 2041–2045.

[77] I. Longstaff, P. Chow, and D. Davies, "Directional properties of circular arrays," in *Proceedings of the Institution of Electrical Engineers*, vol. 114, no. 6. IET, 1967, pp. 713–718.

[78] E. De Witte, H. Griffiths, and P. Brennan, "Phase mode processing for spherical antenna arrays," *Electronics Letters*, vol. 39, no. 20, pp. 1430–1431, 2003.

[79] F. Belloni and V. Koivunen, "Beamspace transform for uca: error analysis and bias reduction," *Signal Processing, IEEE Transactions on*, vol. 54, no. 8, pp. 3078–3089, 2006.

[80] C. P. Mathews and M. D. Zoltowski, "Eigenstructure techniques for 2-d angle estimation with uniform circular arrays," *Signal Processing, IEEE Transactions on*, vol. 42, no. 9, pp. 2395–2407, 1994.

[81] R. Goossens and H. Rogier, "A hybrid uca-rare/root-music approach for 2-d direction of arrival estimation in uniform circular arrays in the presence of mutual coupling," *Antennas and Propagation, IEEE Transactions on*, vol. 55, no. 3, pp. 841–849, 2007.

[82] B. K. Lau, Y. H. Leung, Y. Liu, and K. L. Teo, "Transformations for nonideal uniform circular arrays operating in correlated signal environments," *Signal Processing, IEEE Transactions on*, vol. 54, no. 1, pp. 34–48, 2006.

[83] B. Rafaely, "Plane-wave decomposition of the sound field on a sphere by spherical convolution," *The Journal of the Acoustical Society of America*, vol. 116, no. 4, pp. 2149–2157, 2004.

[84] R. J. Garbacz, "Modal expansions for resonance scattering phenomena," *Proceedings of the IEEE*, vol. 53, no. 8, pp. 856–864, 1965.

[85] Y. Chen and C.-F. Wang, *Characteristic Modes: Theory and Applications in Antenna Engineering*. John Wiley & Sons, 2015.

[86] R. J. Garbacz and R. H. Turpin, "A generalized expansion for radiated and scattered fields," *Antennas and Propagation, IEEE Transactions on*, vol. 19, no. 3, pp. 348–358, 1971.

[87] R. J. Garbacz and D. M. Pozar, "Antenna shape synthesis using characteristic modes," *Antennas and Propagation, IEEE Transactions on*, vol. 30, no. 3, pp. 340–350, 1982.

[88] R. F. Harrington and J. R. Mautz, "Theory of characteristic modes for conducting bodies," *Antennas and Propagation, IEEE Transactions on*, vol. 19, no. 5, pp. 622–628, 1971.

[89] ——, "Computation of characteristic modes for conducting bodies," *Antennas and Propagation, IEEE Transactions on*, vol. 19, no. 5, pp. 629–639, 1971.

[90] J. L. Ethier, "Antenna shape synthesis using characteristic mode concepts," Ph.D. dissertation, University of Ottawa,Canada, 2012.

[91] J. R. Mautz and R. F. Harrington, "Modal analysis of loaded n-port scatterers," *Antennas and Propagation, IEEE Transactions on*, vol. 21, no. 2, pp. 188–199, 1973.

[92] A. J. King and J. T. Bernhard, "An investigation of the characteristic modes of dipole arrays," in *2013 Antenna Applications Symposium on.* Robert Allerton Park,Monticello,Illinois, September 17-19, 2013.

[93] R. E. Collin, *Field theory of guided waves.* Wiley-IEEE Press, 1991.

[94] B. A. Munk, *Finite antenna arrays and FSS.* John Wiley & Sons, 2003.

[95] R. Coifman, V. Rokhlin, and S. Wandzura, "The fast multipole method for the wave equation: A pedestrian prescription," *Antennas and Propagation Magazine, IEEE*, vol. 35, no. 3, pp. 7–12, 1993.

[96] W. C. Chew, E. Michielssen, J. Song, and J. Jin, *Fast and efficient algorithms in computational electromagnetics*. Artech House, Inc., 2001.

[97] J. B. Manges, J. W. Silvestro, and K. Zhao, "Finite-element analysis of infinite and finite arrays," *International Journal of Microwave and Wireless Technologies*, vol. 4, no. 03, pp. 357–364, 2012.

[98] E. Suter and J. R. Mosig, "A subdomain multilevel approach for the efficient mom analysis of large planar antennas," *Microwave and Optical Technology Letters*, vol. 26, no. 4, pp. 270–277, 2000.

[99] L. Matekovits, G. Vecchi, G. Dassano, and M. Orefice, "Synthetic function analysis of large printed structures: the solution space sampling approach," in *Antennas and Propagation Society International Symposium, 2001. IEEE*, vol. 2. IEEE, 2001, pp. 568–571.

[100] J. Yeo, V. Prakash, and R. Mittra, "Efficient analysis of a class of microstrip antennas using the characteristic basis function method (cbfm)," *Microwave and Optical Technology Letters*, vol. 39, no. 6, pp. 456–464, 2003.

[101] X. Wang, D. H. Werner, and J. P. Turpin, "A fast analysis of scattering from large-scale finite periodic microstrip patch arrays arranged on a non-orthogonal lattice using sub-entire domain basis functions," *Antennas and Propagation, IEEE Transactions on*, vol. 62, no. 5, pp. 2543–2552, 2014.

[102] C. A. Balanis, *Antenna theory: analysis and design*. John Wiley & Sons, 2005, vol. 1.

[103] D. M. Pozar, *Microwave engineering*. John Wiley & Sons, 2009.

[104] D. M. Pozar, "A relation between the active input impedance and the active element pattern of a phased array," *Antennas and Propagation, IEEE Transactions on*, vol. 51, no. 9, pp. 2486–2489, 2003.

[105] [Online]. Available: http://www.altair.com/

[106] Y. Chen and C.-F. Wang, "Synthesis of reactively controlled antenna arrays using characteristic modes and de algorithm," *Antennas and Wireless Propagation Letters, IEEE*, vol. 11, pp. 385–388, 2012.

[107] W.-X. Zhang and Y.-M. Bo, "Pattern synthesis for linear equal-spaced antenna array using an iterative eigenmodes method," in *IEE Proceedings H (Microwaves, Antennas and Propagation)*, vol. 135, no. 3. IET, 1988, pp. 167–170.

[108] D. M. Pozar, "The active element pattern," *Antennas and Propagation, IEEE Transactions on*, vol. 42, no. 8, pp. 1176–1178, 1994.

[109] R. L. Chen, D. R. Jackson, J. T. Williams, S. Long *et al.*, "Scan impedance of rsw microstrip antennas in a finite array," *Antennas and Propagation, IEEE Transactions on*, vol. 53, no. 3, pp. 1098–1104, 2005.

[110] J. L. Allen and B. Diamond, "Mutual coupling in array antennas," DTIC Document, Tech. Rep., 1966.

[111] T.-K. Wu, *Frequency selective surface and grid array*. Wiley-Interscience, 1995, vol. 40.

[112] B. A. Munk, "Element types: a comparison," *Frequency Selective Surfaces: Theory and Design*, pp. 26–62, 2000.

[113] N. Engheta and R. W. Ziolkowski, *Metamaterials: physics and engineering explorations*. John Wiley & Sons, 2006.

[114] E. D. Sharp, "A triangular arrangement of planar-array elements that reduces the number needed," *Antennas and Propagation, IRE Transactions on*, vol. 9, no. 2, pp. 126–129, 1961.

[115] R. F. Harrington and J. L. Harrington, *Field computation by moment methods*. Oxford University Press, 1996.

[116] A. Neto, S. Maci, G. Vecchi, and M. Sabbadini, "A truncated floquet wave diffraction method for the full wave analysis of large phased arrays. i. basic principles and 2-d cases," *Antennas and Propagation, IEEE Transactions on*, vol. 48, no. 4, pp. 594–600, 2000.

[117] Ö. A. Çivi, P. H. Pathak, H.-T. Chou, and P. Nepa, "A hybrid uniform geometrical theory of diffraction–moment method for efficient analysis of electromagnetic radiation/scattering from large finite planar arrays," *Radio Science*, vol. 35, no. 2, pp. 607–620, 2000.

[118] C. Craeye, A. Tijhuis, and D. Schaubert, "An efficient mom formulation for finite-by-infinite arrays of two-dimensional antennas arranged in a three-dimensional structure," *Antennas and Propagation, IEEE Transactions on*, vol. 52, no. 1, pp. 271–282, 2004.

[119] E. Garcia, C. Delgado, D. Adana, F. Sáez, F. Cátedra, and R. Mittra, "Incorporating the multilevel fast multipole method into the characteristic basis function method to solve large scattering and radiation problems," in *Antennas and Propagation Society International Symposium, 2007 IEEE*. IEEE, 2007, pp. 1285–1288.

[120] E. Bleszynski, M. Bleszynski, and T. Jaroszewicz, "Aim: Adaptive integral method for solving large-scale electromagnetic scattering and radiation problems," *RADIO SCIENCE-WASHINGTON-*, vol. 31, pp. 1225–1252, 1996.

[121] P. De Vita, A. Freni, L. Matekovits, P. Pirinoli, and G. Vecchi, "A combined aim-sfx approach for large complex arrays," in *Antennas and Propagation Society International Symposium, 2007 IEEE*. IEEE, 2007, pp. 3452–3455.

[122] C. Craeye, "A fast impedance and pattern computation scheme for finite antenna arrays," *Antennas and Propagation, IEEE Transactions on*, vol. 54, no. 10, pp. 3030–3034, 2006.

[123] M. Bebendorf, "Approximation of boundary element matrices," *Numerische Mathematik*, vol. 86, no. 4, pp. 565–589, 2000.

[124] S. Kurz, O. Rain, and S. Rjasanow, "The adaptive cross-approximation technique for the 3d boundary-element method," *Magnetics, IEEE Transactions on*, vol. 38, no. 2, pp. 421–424, 2002.

[125] K. Zhao, M. N. Vouvakis, and J.-F. Lee, "The adaptive cross approximation algorithm for accelerated method of moments computations of emc problems," *Electromagnetic Compatibility, IEEE Transactions on*, vol. 47, no. 4, pp. 763–773, 2005.

[126] A. Pellegrini, A. Monorchio, G. Manara, and R. Mittra, "A hybrid mode matching-finite element method and spectral decomposition approach for the analysis of large finite phased arrays of waveguides," *Antennas and Propagation, IEEE Transactions on*, vol. 62, no. 5, pp. 2553–2561, 2014.

[127] X. Y. Xiong, L. L. Meng, L. J. Jiang, W. E. Sha, F. Yang *et al.*, "Efficient calculation of large finite periodic structures based on surface wave analysis," *Antennas and Propagation, IEEE Transactions on*, vol. 63, no. 1, pp. 69–80, 2015.

[128] A. J. KING, "Characteristic mode theory for closely spaced dipole arrays," Ph.D. dissertation, University of Illinois at Urbana-Champaign, 2015.

[129] D. H. Werner and R. Mittra, *Frontiers in electromagnetics*. Wiley-IEEE Press, 2000, vol. 2.

[130] J. P. Gianvittorio and Y. Rahmat-Samii, "Fractal antennas: A novel antenna miniaturization technique, and applications," *Antennas and Propagation magazine, IEEE*, vol. 44, no. 1, pp. 20–36, 2002.

[131] V. Pierro, V. Galdi, G. Castaldi, I. M. Pinto, and L. B. Felsen, "Radiation properties of planar antenna arrays based on certain categories of aperiodic tilings," *Antennas and Propagation, IEEE Transactions on*, vol. 53, no. 2, pp. 635–644, 2005.

[132] M. Gregory, J. Petko, T. Spence, and D. Werne, "Nature-inspired design techniques for ultra-wideband aperiodic antenna arrays," *Antennas and Propagation Magazine, IEEE*, vol. 52, no. 3, pp. 28–45, 2010.